POLITECNICO DI TORINO

I Engineering Faculty
Master's Degree Course in Aerospace Engineering

Master's Degree Thesis

DESIGN OF THE ELASTIC SUSPENSION FOR A NEW CONCEPT ACCELEROMETER FOR SPACE APPLICATIONS: *LIG-A-CUBE* MISSION

Supervisors:
Prof. Angelo LERRO
PhD. Marco PISANI

Candidate:
Samuele CIUFFREDA

October 2023

INDEX

INTRODUCTION

The thesis here presented is the result of the numerical and experimental research activity carried out with the National Institute of Metrological Research INRiM of Turin and aims to study the design possibilities for a mechanical elastic suspension of the test mass for a new high performance concept accelerometer for space applications. This aforesaid accelerometer is the LIG-A (*Laser Interferometer Gauge-Accelerometer*), carried on board of the spacecraft of the ESA proposed mission LIG-A-CUBE. Laser interferometry is capable of acceleration readings with unprecedented performances, granting high accuracy and low noise, like any other current technology in use and this means it can find uses in scientific space exploration or Earth observation missions like the NGGM (*Next Generation Gravity Mission*). In order to obtain the desired results, it is necessary to use a mechanical elastic suspension that is as loose as possible and has competitive performances compared to the electrostatic type, widely used in the same field of application. Thanks to the sets of knowledge acquired in my years of BSc in Mechanical Engineering and MSc in Aerospace Engineering and skills with FEM (*Finite Elements Method*) softwares, I realized some design proposals for the project of the mass-spring system of the aforementioned accelerometer. Specifically in this thesis I propose two design solutions: the first is an elastic suspension based on a helical spring obtained from a single metal piece, of the so called HELI-CAL® kind, the second solution is a multiple sheets based suspension. The objective is to design a mechanical elastic suspension capable of 6 degrees of freedom of movement, a main modal oscillation frequency in the order of a tenth of an Hz, with a smaller frequency resulting with a better instrument sensitivity.

The body of this thesis is structured as follows. The first chapter introduces the state of the art for high-precision space applications accelerometers, therefore of the capacitive type, with an in-depth analysis of the electrostatic suspension, which is the direct rival of the one to be designed for the LIG-A and an insight of the Italian ISA accelerometer on board of the BepiColombo mission. The second character presents the LIG-A-CUBE space mission, that will be hosting the LIG-A accelerometer that the team I'm working with is designing, with the related objectives and requirements, in particular as regards the elastic suspension. The third and fourth chapters represent the main body of this work of master thesis and respectively present the two design solutions proposed for the mechanical suspension in question, which are of the HELI-CAL® type and multiple sheets type. In both chapters the first part presents a preliminary FEM study, in which it is determined how to construct the models with the *MSC Patran* software and the scope of validity of the solutions obtained in the numerical analyses performed by the *Nastran* solver. A delightful insight is the presentation of an analytical and numerical method developed by me which, based on a lumped parameter simplification of the elastic-dynamic problem, pursuits the determination of the virtual rotation centre of the bending oscillatory mode of a mass-spring system (3.1.5 e 4.4.4 subsections). The reliability of the numerical results are confirmed by empirical measurement tests conducted within the INRiM labs. The chapters follow with a section on the study of the influence of the design parameters of the elastic suspension on the modal response, both in the case of the HELI-CAL® type suspensions but also, in a more detailed way, for the multiple sheets elastic suspension. Finally, for both cases, design solutions are proposed with dimensioned technical drawings and details on the assembly of the different mechanical parts, with the relative FEM modal analyses which determine the performance of the proposed systems in terms of the oscillation frequencies, with the aim to demonstrate that the requirements are met. From this design study it is possible to deepen the details in order to better define a final construction solution of the mechanical suspensions in question for the LIG-A accelerometer, however the proposed methods and results have general value and could find applications outside of this specific context.

1 ACCELEROMETERS FOR SPACE APPLICATIONS

Accelerometers are instruments capable of measuring the proper acceleration and they find many applications in science and technology, such as the use in inertial navigation systems of aircrafts and spacecrafts, vibration monitoring of mechanical systems, measure of the gravitational field anomalies or more trivial employments such as to allow rotation of the screen display in modern electronic devices.

In more scientific terms, an accelerometer is a tool capable of reading the proper relativistic acceleration that a system, to which the instrument is anchored, is subjected to, be it due to a change of velocity, to gravitational or inertial forces. It does not measure the absolute coordinate acceleration with respect to a fixed inertial reference system but the acceleration with respect to an instantaneous rest reference system of the instrument [1]. In fact, for an object stationary on the Earth's surface, an accelerometer would supply an output value equal the gravity acceleration, on the contrary if the object is free falling and therefore subjected to constant acceleration with respect to an Earth's fixed reference system, the instrument would supply a null acceleration value [2].

The operating principle of most accelerometers consists in determining the inertial acceleration derived from the measurement of the displacement of a so called test mass, suspended on an elastic element. The behaviour of the test mass depends on the nature of the acceleration: a gravitational force will produce the same acceleration regardless of the mass, while for an inertial force the acceleration will be inversely proportional to the value of the mass. According to the equivalence principle, the actions of a gravitational and non-gravitational force are indistinguishable. Different types of accelerometers are classified depending on the technology used for measuring the mass displacement and the most common one used in space is of the capacitive type, while the newly developed accelerometer proposed in this thesis work will exploit laser interferometry.

In space applications the accelerometer is an essential component, especially for missions dedicated to space geodesy, space exploration and fundamental physics or as an auxiliary tool, for example to determine the residual vibration noise on the International Space Station. High sensitivity at low frequencies, down to 10^{-3} Hz, will be required for high precision applications. A spacecraft might be equipped with a *drag free control* or *drag adjustment system* where the actuators directly follow the accelerometer inputs so as to compensate for all disturbances and thus cancel the measured inertial acceleration. Hence the habit of some authors to refer to accelerometers improperly as "inertial sensors", since only if there is *a priori* certainty that the disturbances measured are predominantly inertial in nature, one could name accelerometers correctly that way.

If low frequency sensitivity is required for applications such as space geodesy, conversely for less demanding applications, such as the characterization of vibrations on the ISS, high frequency sensitivity will also be required, because such vibrations will have a structural sonic and human voice nature. The LIG-A accelerometer (*Laser Interferometry Gauge & Accelerometer*) of the demonstrative space mission currently in design process by INRiM, covered in this thesis, is able to be highly competitive in this context thanks to the very high displacement measurement accuracy granted by the laser interferometry and the use of an highly loose elastic suspension for the test mass, which will be the object of my design work [3].

1.1 State of the Art: Capacitive Accelerometers

1.1.1 Electrostatic Suspension

Capacitive accelerometers are characterized with a test mass that constitute an armature of a capacitor and with its oscillations, with respect to the armature integral with the accelerometer, the capacity varies and therefore an electrical signal is generated which depends on the position of the mass. An example of high-sensitivity capacitive accelerometers for space applications are those built by the French ONERA, used on space missions such as CHAMP, GOCE, GRACE and MICROSCOPE. In this case the suspension of the test mass is of the electrostatic type, which works as a negative stiffness spring, as shown in the following figure.

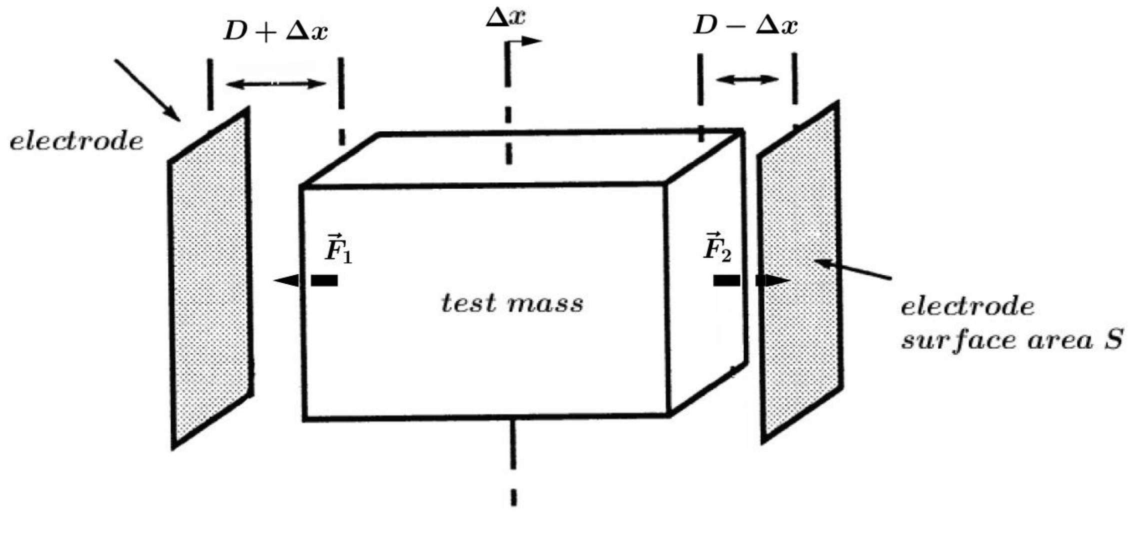

Fig. 1.1: Operating principle of the electrostatic suspension for a capacitive accelerometer

The electrostatic force is always attractive and since the test mass is attracted to the closest electrode, the equilibrium position will be unstable. It is therefore required an application of a force to bring the mass back to the central equilibrium position. The action of this control force must depend on the displacement Δx of the test mass, however the electrical signal generates a spurious force which causes noise at all frequencies. Referring to Fig. 1.1 and calling D the distance between the test mass and the electrodes, the behaviour of the suspension can be described as a "negative spring":

$$F_2 - F_1 = \frac{1}{2}\varepsilon_0 S V^2 \left[\frac{1}{(D-\Delta x)^2} - \frac{1}{(D+\Delta x)^2}\right]$$

$$F_2 - F_1 \cong \frac{2\varepsilon_0 S V^2}{D^3}\Delta x$$

$$F_2 - F_1 \cong -k_{electrostatic}\Delta x$$

- $-k_{electrostatic} = \frac{2\varepsilon_0 S V^2}{D^3}\Delta x$

A system of this nature needs very small gaps, in the order of tenths of a millimetre, to ensure adequate sensitivity to small variations in capacitance and to exert sufficient control force. This implies however an amplification of electrical and thermal noise, due to the gas thermal agitation of the trapped molecules. A capacitive accelerometer will be thus characterized by a spectrum with high electronic noise at low frequencies, as shown in the figure below.

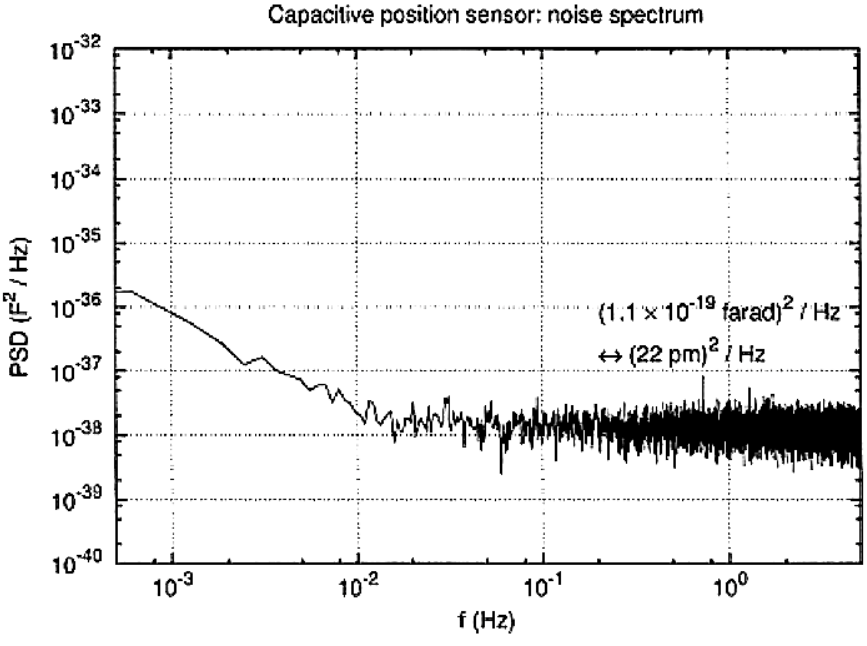

Fig. 1.2: Noise spectrum of the ONERA capacitive accelerometer [4]

1.1.2 The ISA Accelerometer

Currently on board the MPO (*Mercury Planetary Orbiter*) spacecraft of the ESA BepiColombo mission, is present the highly sensitive, three-axis capacitive accelerometer ISA (*Italian Spring Accelerometer*), provided by the Institute of Astrophysics and Space Planetology of Rome, with the aim of mapping Mercury's gravitational field to study its internal structure. What distinguishes it from the before mentioned cases is the use of a mechanical spring, as can be guessed from the name, for the suspension of the test mass as an alternative to the electrostatic suspension. Our special interest on the ISA accelerometer is justified by the fact that the past INRiM experience on space accelerometers is based upon mods and experiments carried upon an ISA prototype.

ISA is composed of three elements sensitive to accelerations on a single axis, in order to obtain a reading on three orthogonal axes. Each element consists of a test mass elastically suspended by a thin blade, all built from a single piece of aluminium. The blade allows the test mass to oscillate on a single axis of rotation. The oscillating mass is included between two plates which act together with the mass as capacitor electrodes, allowing to detect displacement values of the mass in the order of 10^{-12} m.

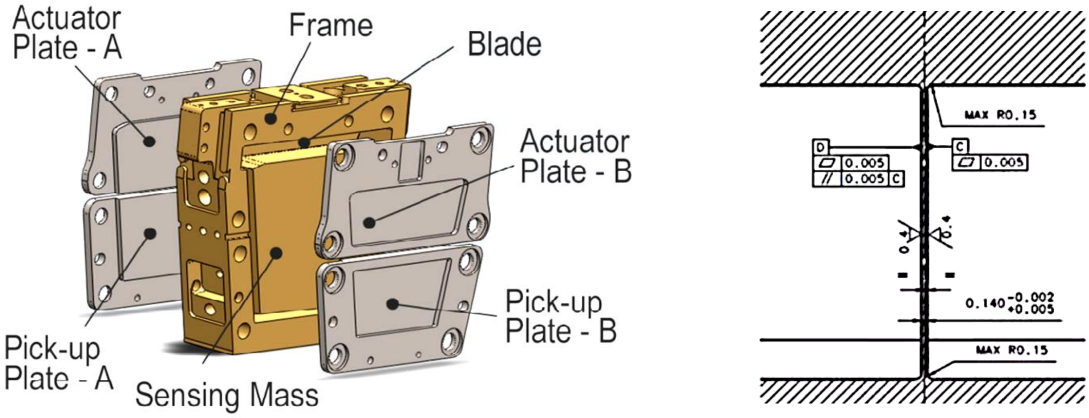

Fig. 1.3: Sensible element and a detail of the elastic suspension blade of the test mass

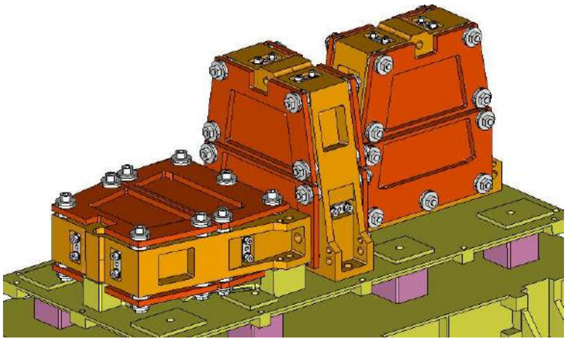

Fig. 1.4: Layout of the three sensible elements of the ISA instrument

The main task of ISA is to support the scientific activities of the MORE (*Mercury Orbiter Radio science Experiment*) instrument through acceleration measurements. The orbit of the spacecraft is highly perturbed, for example by the effect of solar radiation pressure, and ISA contributes to the orbit determination procedure. The scientific objectives of this collaboration can be divided into three parts.

Gravimetry Experiment The aim of this experiment is the study of Mercury's gravitational field to characterize its internal planetary structure, such as the mantle and the crust-mantle interface, through local gravitational anomalies. The MPO satellite can be considered as a proof mass whose trajectory crosses the gravitational field of the planet. Through least square estimates between the observed orbit (through radio tracking) and the path predicted by numerical models, the orbit of the MPO and the gravitational field of Mercury can be reconstructed simultaneously.

Rotation Experiment The objective is to determine the rotational state of Mercury, therefore the direction of its polar axis and the amplitude of the librations in longitude of the duration of 88 days. This estimate is obtained by observing reference points on the surface with an optical camera and therefore a great precision is required by the MPO's AOCS (*Attitude and Orbit Control System*) to reconstruct the camera pointing. The relative position of the satellite with respect to the inertial reference of Mercury is required to be determined with an error of less than 3 m, which can only be obtained thanks to the data of the gravimetric experiment.

Relativity Experiment The proximity of Mercury to the Sun allows the emergence of observable relativistic effects, such as the excess of the precession of the perihelion of Mercury's orbit with respect to a classical Newtonian model. From range measurements through a tracking from the Earth and the determination of the MPO orbit around the planet through MORE’s data and of Mercury's orbit around the Sun, it will be possible to test the values of some parameters of Einstein's General Theory of Relativity.

A meaningful contribution of the ISA accelerometer is to the orbit determination procedure of MORE, called POD (*Precise Orbit Determination*), through acceleration measurements. The MPO spacecraft is equipped with moving masses and therefore the acceleration measured by the ISA accelerometer will have, in addition to the contributions of gravitational and non-gravitational forces, an apparent acceleration contribution due to the displacement of the satellite's centre of gravity. Therefore ISA measurements should be integrated with information on the displacement of the COM (*Centre Of Mass*) vector with an accuracy that entails the strict COM stability requirements. Alternatively, the COM of the ISA instrument can be used instead of that of the entire spacecraft for the POD, in order to simplify the equations to be solved to determine the trajectory in Mercury's gravitational field.

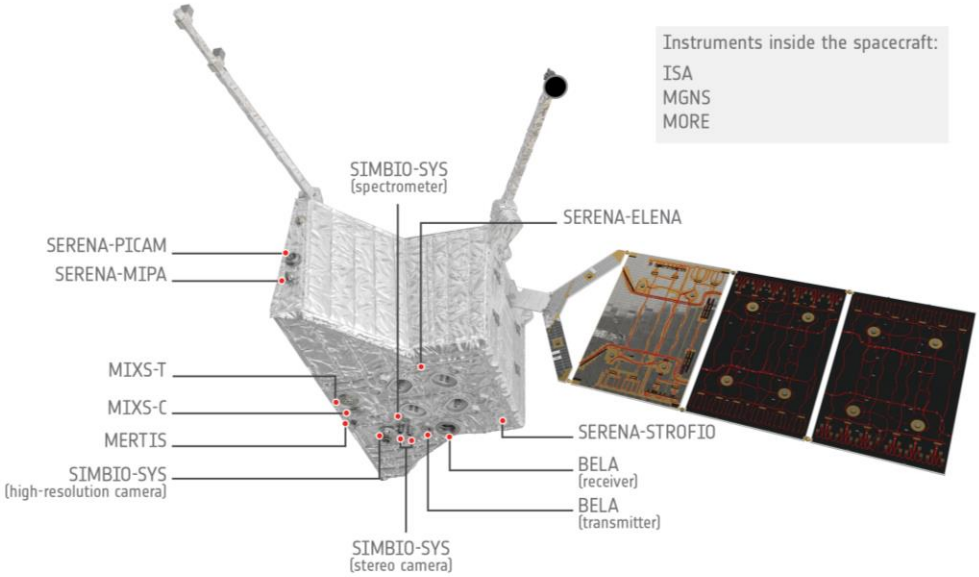

Fig. 1.5: MPO, spacecraft of the BepiColombo mission, which carries the ISA instrument on board

BepiColombo is the first interplanetary mission with a highly sensitive accelerometer on board, specifically in function of the scientific purposes it must perpetrate. In general space vehicles are anyway equipped with an accelerometer inside the IMU (*Inertial Measurement Unit*) for determining and controlling the orbit and attitude but with performances that are not comparable with those of high-precision accelerometers such as ISA or the aforementioned CHAMP, GRACE and GOCE ones. The potential of ISA can also come into play in the stages preceding the purely scientific ones such as before the separation of the MCS (*Mercury Composite Spacecraft*), which is the spacecraft of the mission BepiColombo made up of two parts, the aforementioned MPO (*Mercury Planetary Orbiter*) and the MMO (*Mercury Magnetospheric Orbiter*). In this context ISA is playing a role in determining non-conservative forces during the cruise stages, gravitational gradients due to planets during flybys, MCS accelerations during thruster transits, density variations in the magnetosphere during flybys, impacts from dust, debris or micrometeorites [5].

2 LIG-A-CUBE SPACE MISSION

The LIG-A-CUBE space mission proposed with the INRiM (*Istituto Nazionale di Ricerca Metrologica*) for ESA, has the purpose of demonstrating the performance of the LIG-A accelerometer (*Laser Interferometry Gauge & Accelerometer*) which has as the main characteristic, that differentiates it from all the other accelerometers used in space, the use of laser interferometry as the technology for measuring the displacement of the test mass. Furthermore, to reduce the electrical noise typical of high sensitivity accelerometers for space applications described in the previous chapter, where an electrostatic suspension and capacitive reading was used, the use of a mechanical elastic suspension for the test mass is proposed. The goal of this thesis is to design such an elastic suspension. In response to ESA's *Call for Ideas*, the proposed mission plans to use a 20U CubeSat (volume unit 1U = 10×10×10 cm) as a demonstrator satellite of this technology and to allocate 8U (2×2×2 U) to service platforms and 12U (2×3×2 U) for the payload which would consist primly of LIG-A accelerometers. The orbit will be low polar with passive Earth attitude pointing.

An interferometry gauge for measuring displacement with heterodyne detection exploits the principle by which two rays of coherent light (laser) with slightly different modulated frequencies, meet to form a beating interference pattern and one of the beams reflects on the surface of the moving test mass. By measuring the relative phase of the beat frequency, it is possible to obtain the displacement of the test mass with an accuracy of the order of half the wavelength of the source. In this context, LIG-A is nothing more than an evolution of the LIG (*Laser Interferometry Gauge*) already developed at INRiM with an ITI type A contract, of which we want to maintain the technology but with a miniaturization of the components.

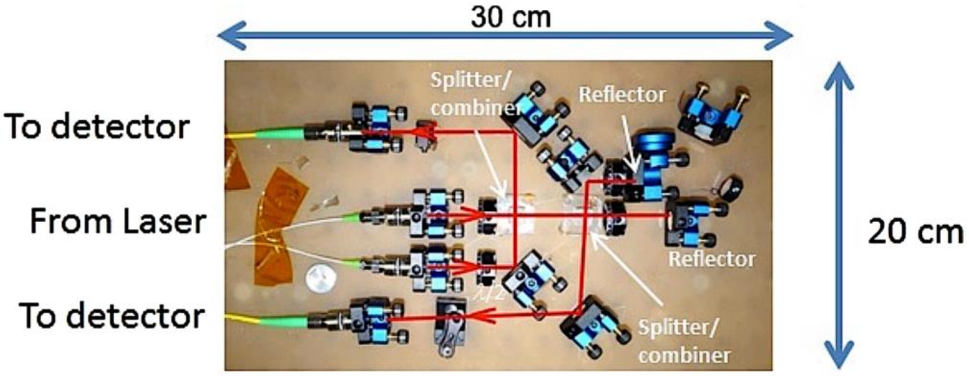

Fig. 2.1: LIG's optic circuit [6]

An experiment campaign with simultaneous measurements conducted with the same test mass, which is that of the type used in the ISA instrument presented in the previous chapter, have compared the results obtained from a capacitive reading with an interferometric one obtained with the LIG, confirming the superiority of the LIG as regards noise, however for frequencies below 2 mHz the noise is dominated by local seismic vibrations for both systems. Above 3 mHz the results obtained with laser interferometry are up to 40 times better than the capacitive ones, as shown in the spectrum below.

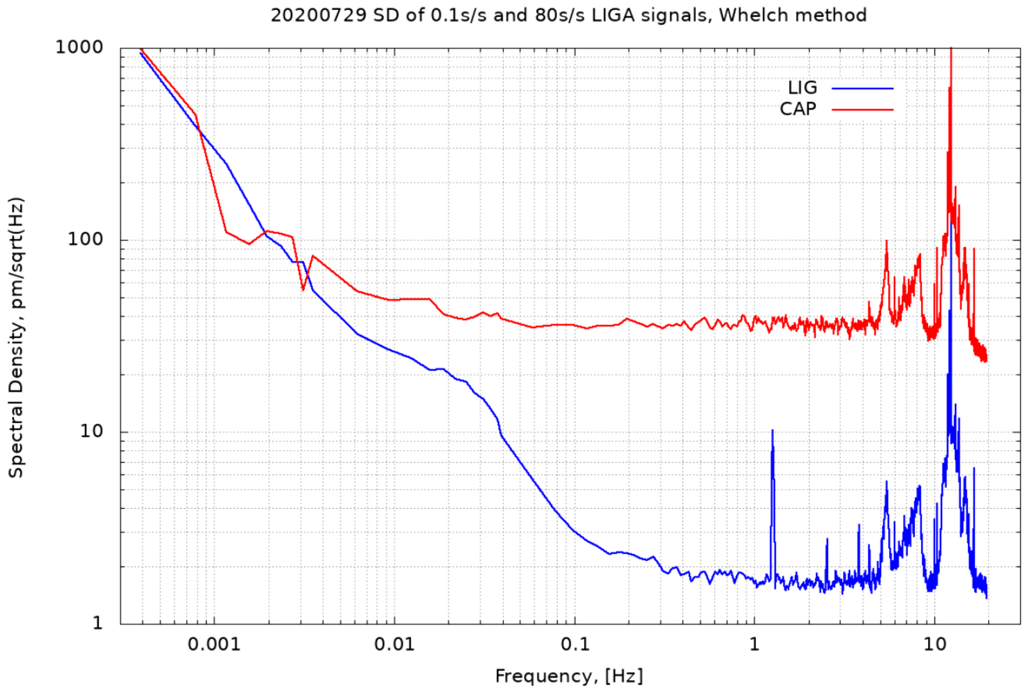

Fig. 2.2: Comparison of the noise spectrum of displacement readings of the test mass with capacitive technology (in red) and with laser interferometry of the LIG (in blue) [3]

The natural frequency of the ISA test mass with a blade suspension used in this comparison is 5.8 Hz, which is equivalent to 36.44 rad/s. This implies that for a frequency of 1 mHz and a displacement sensitivity of 30 pm/√Hz measured by the LIG, the acceleration sensitivity results to be [3]:

$$3 \times 10^{-11} \frac{rad}{s} \times \left(36.44\ \frac{pm}{\sqrt{Hz}}\right)^2 \cong 3.98 \times 10^{-8} \frac{ms^{-2}}{\sqrt{Hz}}$$

From similar measurements of those reported in Fig. 2.2 it was evaluated a noise at 1 Hz in the order of 0.35 pm/√Hz which results in an acceleration noise of:

$$3.5 \times 10^{-13} \frac{rad}{s} \times \left(36.44\ \frac{pm}{\sqrt{Hz}}\right)^2 \cong 4.6 \times 10^{-10} \frac{ms^{-2}}{\sqrt{Hz}}$$

This establishes that both project requirements of the LIG-A proposal to ESA have been met [6]:

"The baseline LIG-A accelerometer shall be sensitive in a wide frequency range, spanning 3 frequency decades from 10-3 Hz to 1Hz, with an acceleration noise going from 5x10-8 ms-2/√Hz at 10-3 Hz to 5x10-10 ms-2/√Hz at 1Hz. Realization shall be limited to 1D."

An evolution of the LIG-A interferometry system was developed for the LIG-A-CUBE mission, with a breadboard integrating both the interferometers and the test mass. The new reading unit will be composed of two very compact interferometers, one of which is equipped with fixed mirrors that provides a reference measurement. The optical layout is designed with the purpose of maximizing the symmetry and minimizing the number of components. The fiber design will be basically identical to the LIG-A one but with a smaller footprint [8].

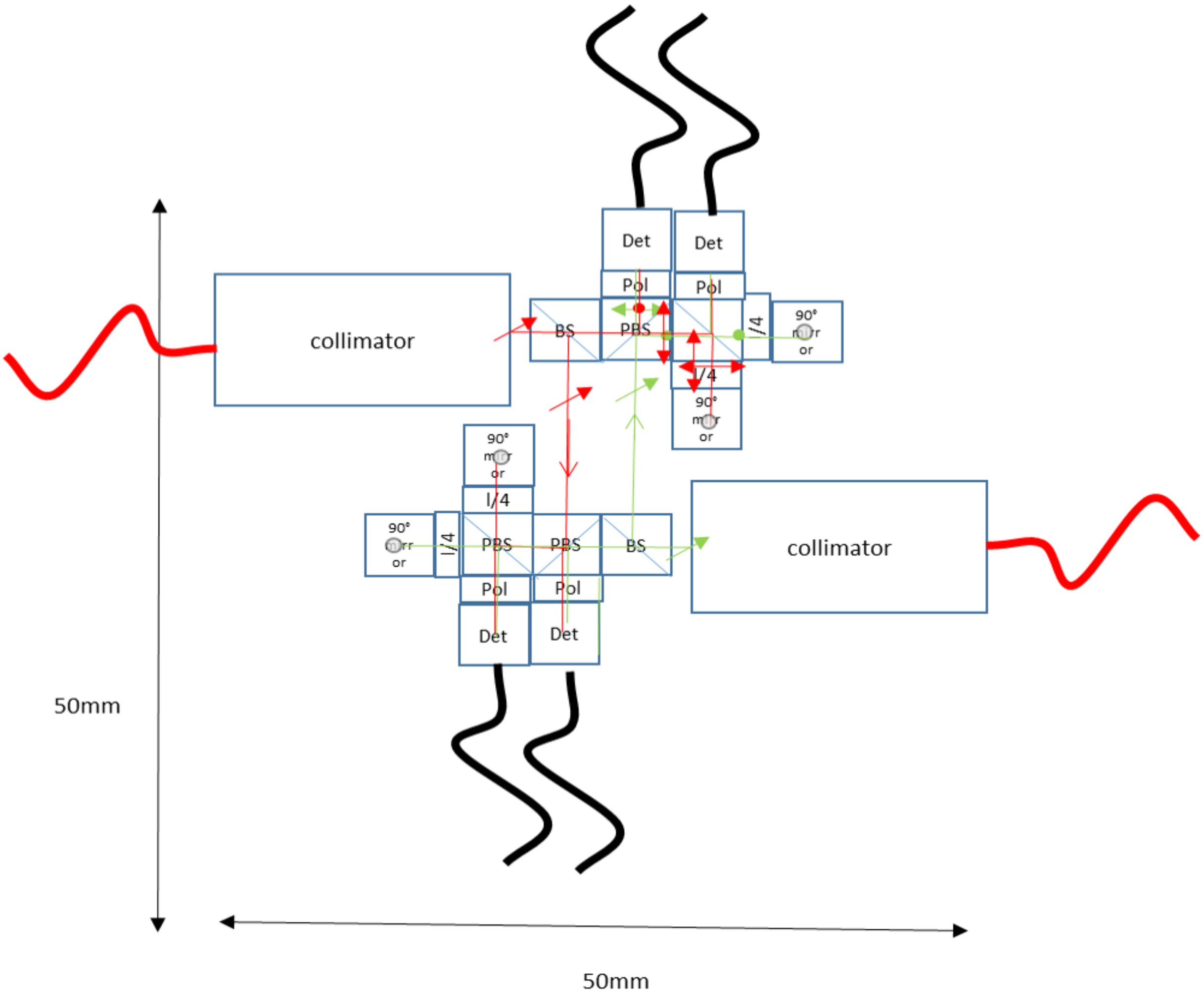

Fig. 2.3: Evolution of the LIG-A optical design, side view [8]

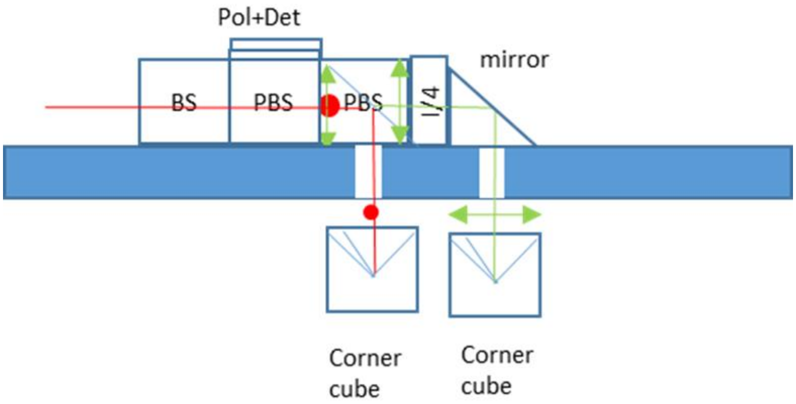

Fig. 2.4: Evolution of the LIG-A optical design, side view [8]

The interferometers will be assembled with discrete off-the-shelf optical components, glued to a metal plate of low thermal expansion coefficient such as Invar®. The moving mirror is embedded in the test mass while the base plate is fixed to part of the spacecraft's frame.

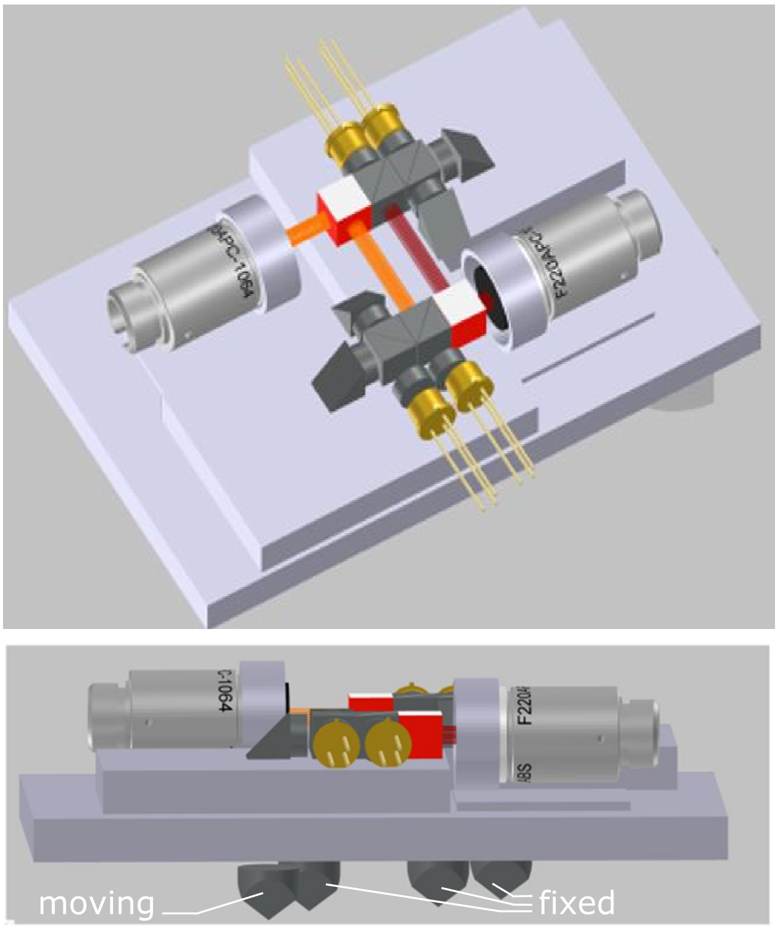

Fig. 2.5: Optical components and base plate of the LIG-A evolution [8]

The interferometer will be measuring only one translational degree of freedom of the respective test mass and two LIG-A systems will be present on board the spacecraft, in order to also measure twisting accelerations and to get more robust measurements. By subtraction of the two readings of the two test masses in one direction it is possible to evaluate the unwanted vibrations that need to be deleted in order to get a more reliable acceleration reading. In the following picture the payload layout inside the 200×200×300 mm section of the spacecraft is represented which must also be compliant with the M3 platform, the same used in the OHB Eaglet II nanosatellite [8].

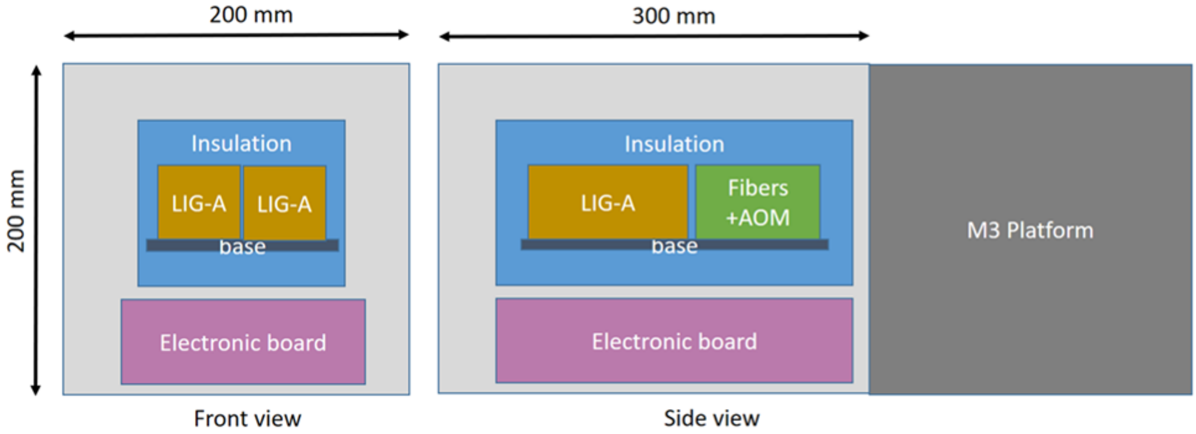

Fig. 2.6: Payload layout of the LIG-A-CUBE with the M3 platform [8]

The main interest for our purposes is the elastic suspension of the accelerometer test mass for the LIG-A-CUBE mission, of which I submitted different design proposals as a result of the thesis work at the INRiM of Turin. A mechanical type suspension is chosen to avoid the electrodes of an electrostatic suspension and the relative control of the test mass, allowing the setting of a passive equilibrium position and an electrical grounding. The elastic suspension must have a modal oscillation frequency in the sensitive direction as low as possible, since displacement noise translates into acceleration noise through the square of the natural oscillation frequency of the accelerometer test mass. The mechanical elastic suspension will have to guarantee all 6 degrees of freedom of translation and rotation of the test mass, so as to allow sensitivity on 3 orthogonal axes for a potential simultaneous reading [7]. In the proposed mission, being only demonstrative, the interferometric reading will be sensitive to only one axis even if the mass will still have to provide freedom in the other axes in order to withstand any kind of stress during launch. To reduce thermal noise, a single solid piece construction or an assembly that minimizes the use of glue and seams, which are the main source of losses, is preferred. It is better to have gaps of adequate size, because small gaps are another source of noise induced by thermal agitation of the residual air molecules trapped between the electrodes. In response to the *Call for Ideas* for ESA it was proposed that the LIG-A-CUBE mission should carry two test masses, each with a single-axis LIG-A reading, to allow an accelerometer sensitivity to 2 degrees of freedom, one for translation and one for rotation. The natural frequency initially proposed for the mass-spring system was 0.07 Hz but it was subsequently discussed to bring the requirement to a more realistic value of a maximum of 1 Hz [6]. Another requirement for the suspension design concerns dimensions. The goal is to bring the dimensions to the minimum possible to demonstrate that the technology is miniaturizable and therefore competitive for applications in scientific space exploration missions, despite having 12 U of payload available for the demonstration mission. It must be remembered that in any case two test mass - elastic suspension devices must be carried on board to allow sensitivity also to rotation. The volume requirement agreed with Doc. Pisani for the design of the single elastic suspension system with test mass is not to exceed a box of 40 × 40 × 70 mm.

3 HELI-CAL ELASTIC SUSPENSION

A suspension system that we have taken into consideration because it can potentially comply with the project requirements is the *HELI-CAL®* type, a technology in use for the construction of torque couplings. In Mechanics this type of joint, also known as *Beam coupling*, was conceived to transfer torque between two misaligned rotating shafts and is obtained from a single machined piece of metal.

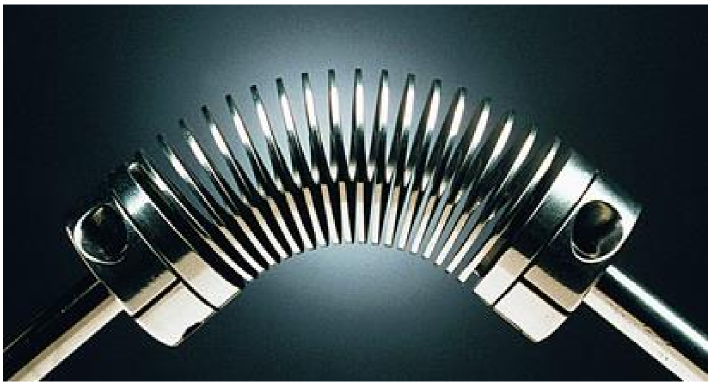

Fig. 3.1: *Mondial HELI-CAL®* beam coupling for large misalignments [9]

The potentiality of manufacturing different spiral shapes and thickness according to needs, from a single block of the same material, provides this kind of solution with the ideal characteristics for employment as a precision spring. The performance of a beam coupling of this type depends on the following factors:

- Configuration and thickness of the coils
- Inside diameter
- Number of coil and coil starts
- Material

Thickness and inside diameter:
The variation of these parameters affects angular and radial misalignment (which are the ones of our interest), torsional strength and compression ratio.

Number of coils:
Affects all parameters except torque capacity.

Number of coil start:
A higher number of coil starts increases torsional stiffness.

1. The single-start spiral makes for a continuous individual spiral;

2. The two-start spiral provides for the overlapping of two spirals with the second starting at 180° from the first;
3. Similarly, the three-start coil has three spirals placed at 120° from each other.

Material:

Material-dependent factors are of course properties such as elasticity, fatigue and corrosion resistance. The high-strength materials typically used in HELI-CAL® joints are:

- Corrosion resistant steel 17-4PH
- Inox steel 15-5 PH
- Steel C300
- Titanium BETA C
- 7075-T6 Aluminium

This kind of precision machined springs grant the achievement of design objectives such as reliability, repeatability and accuracy. They guarantee extremely precise linear deflection values, since virtually all residual stresses are eliminated [9]. Using two identical spirals in the same piece but with opposite directions of rotation, it is possible to compensate for the problem of coupling between the two degrees of freedom of torsional rotation and axial elongation typical of spiral elements.

3.1 FEM Preliminary Study: Helical-A Model

3.1.1 Helical-A Model: Static

Fig. 3.2: CAD rendering of the Helical-A model

For a preliminary FEM analysis of a spring of this type, I built a prototype CAD of an Helical spring with characteristics that might meet of our interest, therefore with a thin wall and with many coils. In this specific case I started by choosing two spirals of three and a half coils each, with opposite rotation directions, 1 mm thick radial wall and external dimensions similar to those of a commercial available beam couplings.

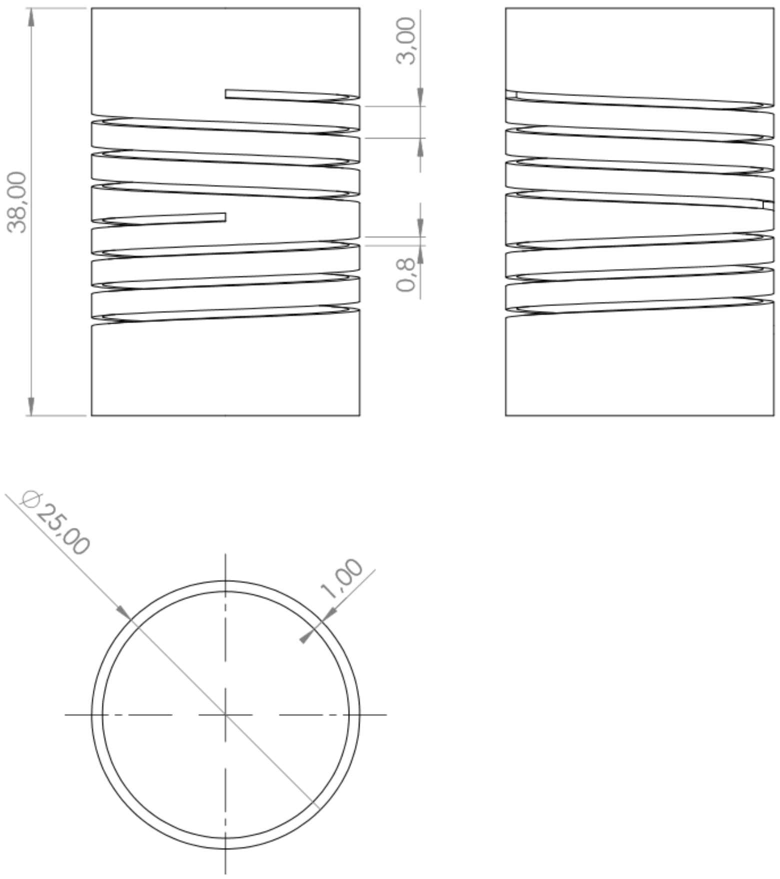

Fig. 3.3: Dimensioned CAD of the Helical-A model

For our purposes, we are first of all interested in the bending behaviour, which is what our elastic suspension will be subjected to during lateral acceleration. Mechanically, therefore, the model is simplified by reducing it to a torsional spring, with elastic constant k_t which is obtained from the lateral displacement Δx as:

$$k_t = \frac{FL}{\vartheta}$$

With:

$$\vartheta \cong \left(\frac{\Delta x}{L}\right) \, [rad]$$

The above formulas are referring to the simplified model in the following figure, with the spring pivot centre initially considered at the base:

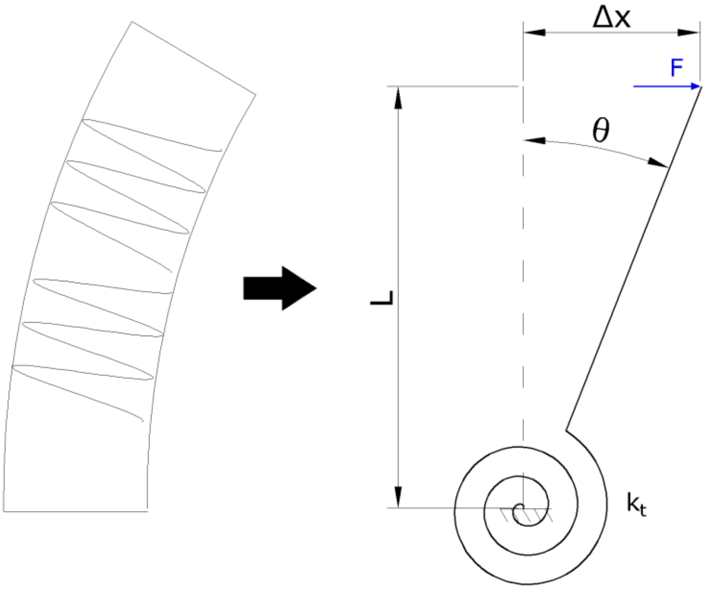

Fig. 3.4: Simplified lumped model to find the bending elastic constant of the spring

I use the FEM *MSC Patran – Nastran* software to perform static analyses of the behaviour of the spring, in the linear and non-linear field, using an automatic three-dimensional tetrahedral element meshing, with a *global edge length* of 4.55 mm. In this preliminary study phase an exact characterization of the material is not important and it is set as isotropic with the typical properties of a generic steel:

Elastic Modulus:	E = 210000	[MPa]
Poisson's Ratio:	$\nu = 0.3$	
Density:	$\rho = 7.85\text{e-}9$	[Ton/mm^3]

It is useful to remind that the *Patran - Nastran* software infers without units of measurement, therefore we need to be careful in choosing a system of coherent units and respect it. Because we choose millimetres for length, the unit system will be:

$$mm - N - MPa - Ton$$

Different analyses are reiterated with a linear static solution (Nastran code SOL 101) and a non-linear static solution (Nastran code SOL 106), thus the maximum displacement values are obtained, from which the bending stiffness is derived for a range of forces of small values, in the range of interest, and is subsequently verified that consistent results are obtained.

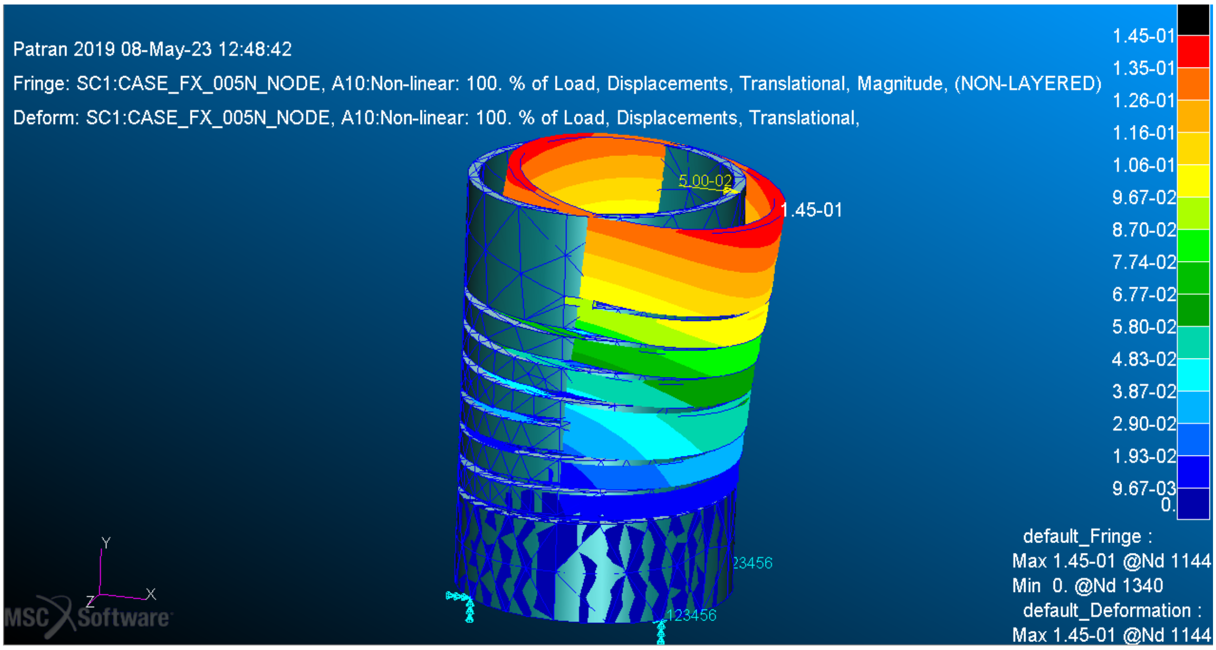

Fig. 3.5: Displacements plot for Nastran SOL 106 analysis with side force of 0.05 N for the Helical-A model, mesh with *Global edge length* of 4.55 mm

	Nastran SOL 101		**Nastran SOL 106**	
F	**max displ.**	**k_t**	**max displ.**	**k_t**
[N]	**[mm]**	**[Nmm/deg]**	**[mm]**	**[Nmm/deg]**
0.05	0.146	**8.63**	0.145	**8.70**
0.10	0.292	**8.63**	0.289	**8.74**
0.20	0.584	**8.63**	0.576	**8.74**
0.50	1.46	**8.63**	1.42	**8.89**
1.00	2.93	**8.63**	2.77	**9.12**

Tab. 3.1: Bending stiffness results for the FEM analysis of the Helical-A model, rough mesh of 4.55 mm of *Global Edge Length*

It can be observed from the results that, as expected, the linear analysis always provides the same bending stiffness value while the non-linear analysis provides very similar values but with a slight increase as the load increases. For small force values, linear and non-linear analyses provide practically the same results, close values are always obtained even for forces greater than those of our interest, i.e. of the order of a Newton. This is a good result and makes us understand that it is possible to continue with this type of analysis and modelling to study the influence of the different design parameters on the elastic performance of springs of this type.

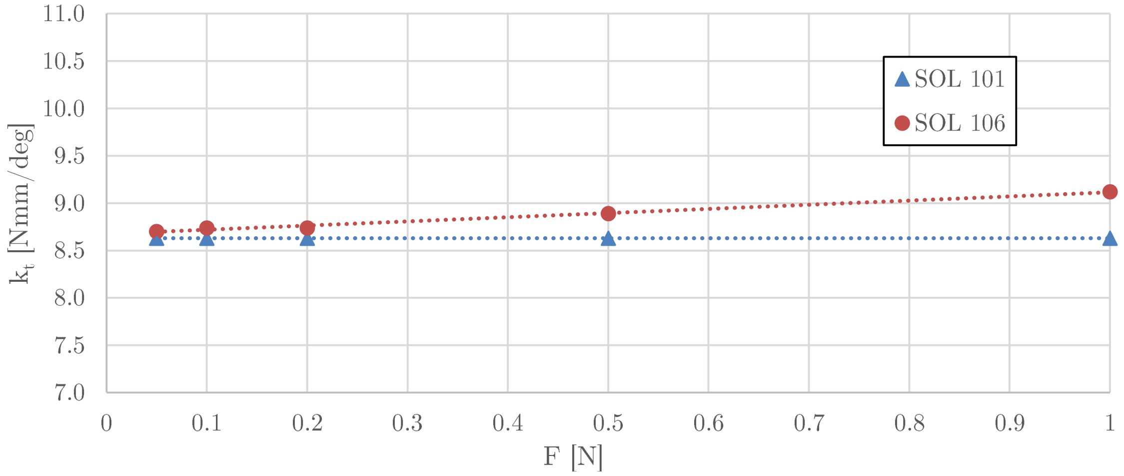

Fig. 3.6: Comparison of bending stiffness results for linear and non-linear analysis

This non-constant trend of the non-linear results is due to *large displacements phenomena* coming into play for larger loads, which however should not be of interest to us in our applications.

3.1.2 Helical-A Model: Mesh Convergence Analysis

In order to obtain better results, the mesh can be made denser at the price of an higher computational cost for each single analysis. To optimize the procedure, a convergence study can be performed to find the maximum *Global Edge Length* (GEL) value of the *Tet* (tetrahedral) type elements to ensure sufficiently accurate results.

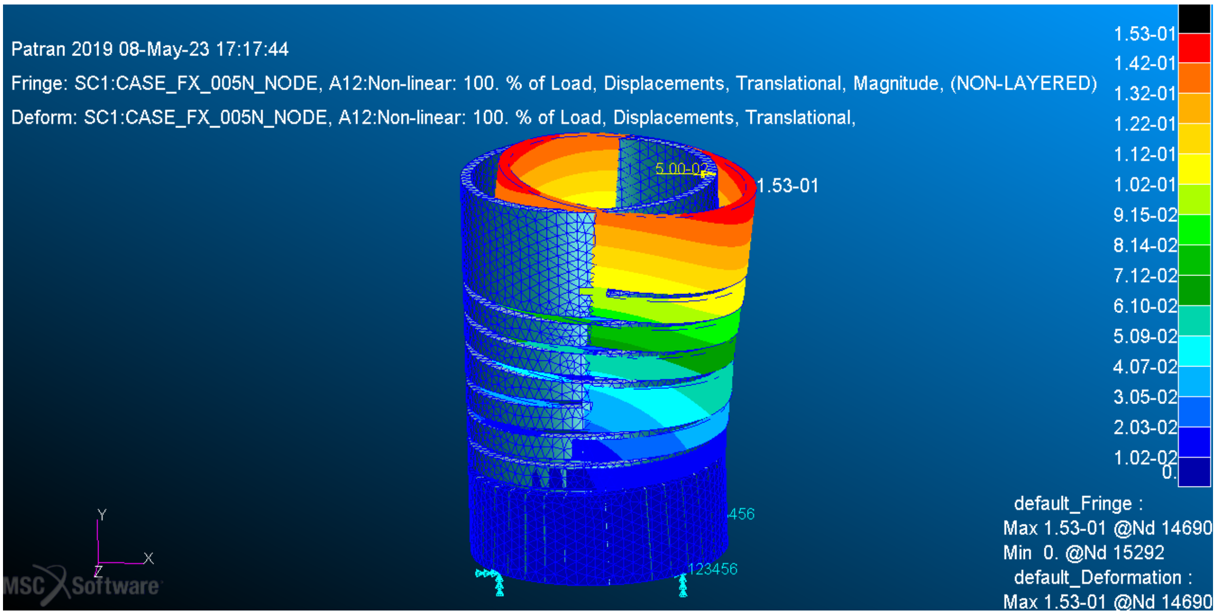

Fig. 3.7: Displacements plot for Nastran SOL 106 analysis with side force of 0.05 N for the Helical-A model, denser mesh with *GEL* of 4.55 mm

	Nastran SOL 101		Nastran SOL 106	
	max displ.	k$_t$	max displ.	k$_t$
F [N]	**[mm]**	**[Nmm/deg]**	**[mm]**	**[Nmm/deg]**
0.05	0.153	**8.24**	0.153	**8.24**
0.50	1.53	**8.24**	1.49	**8.46**

Tab. 3.2: Bending stiffness results for the FEM analysis of the Helical-A model, denser mesh of 1 mm of *GEL*

Results obtained with a mesh of 1 mm of GEL are certainly more refined, with a difference of about 5% compared to the values obtained with an automatic meshing of 4.55 mm GEL, but this comes at an high computational cost (482 seconds for the SOL 106 analysis at 0.5 N). Even with the finer mesh we find the same relative increase in stiffness with increasing load for the non-linear analysis of the previous case, meaning this phenomenon is independent of the mesh. A compromise is therefore necessary between computational cost and reliability of the results.

Since we shouldn't be interested in the non-linear field, because the space applications of the accelerometer in the project require it to be sensitive to micro-accelerations and therefore large displacements are not created, the convergence study is carried out only for the linear solution SOL 101, therefore for small loads. In particular I choose the load of 0.05 N of which we already established that linear and non-linear solutions coincide.

Convergence Analysis, 3D Mesh:

1. Element shape: Tet (tetrahedral)
2. Mesher: TetMesh
3. Topology: Tet10

Mesh Tet	Nastran SOL 101					
	F	max. x	k$_t$	Run Time	N. of	Error
GEL [mm]	**[N]**	**displ. [mm]**	**[Nmm/deg]**	**[s]**	**nodes**	**%**
0.50	0.05	0.160	**7.88**	129	231970	Ref.
0.75	0.05	0.157	**8.03**	52.7	89005	1.90
1.00	0.05	0.153	**8.24**	17.4	39989	4.57
1.50	0.05	0.151	**8.34**	8.83	17709	5.84
2.00	0.05	0.148	**8.51**	7.58	10489	7.99
4.55	0.05	0.146	**8.63**	5.25	4967	9.52

Tab. 3.3: Bending stiffness results in function of the mesh elements dimensions for the FEM analysis of the Helical-A model

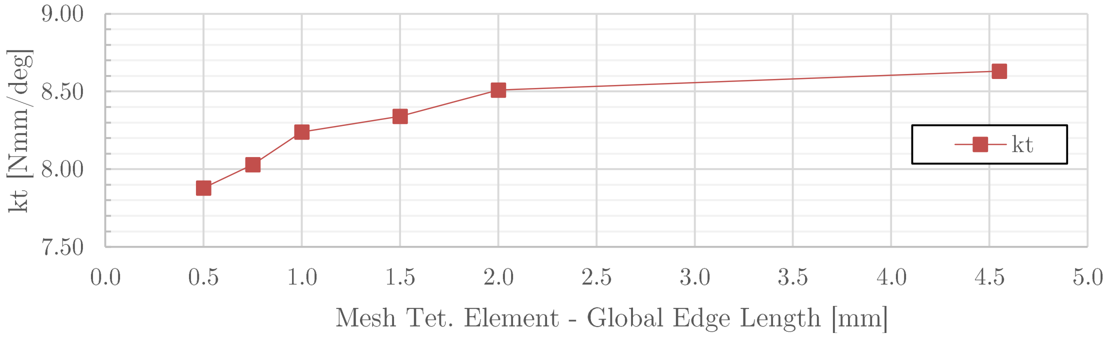

Fig. 3.8: FEM results variation of bending stiffness with the average size of the tetrahedral mesh element, for the Helical-A model

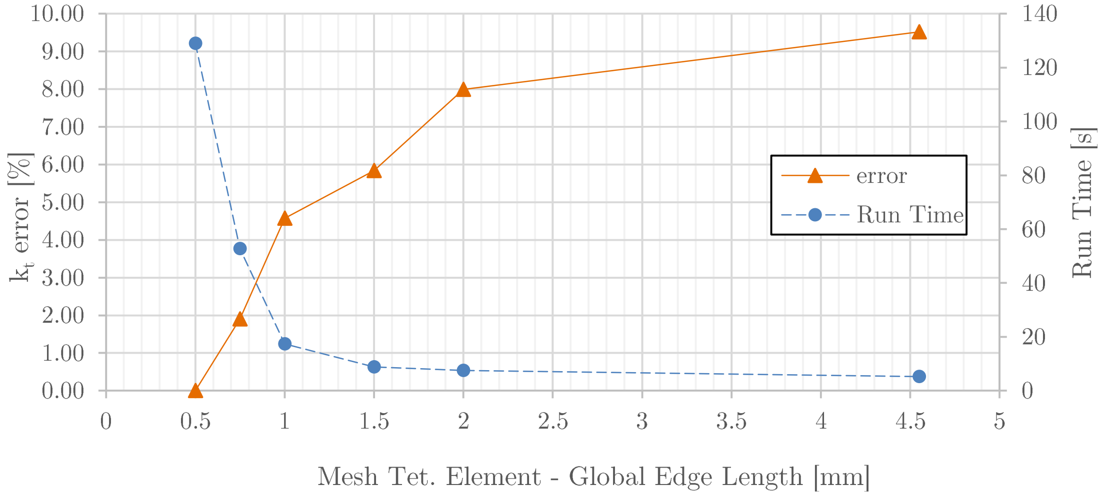

Fig. 3.9: Error and analysis time of the FEM results as a function of the size of the 3D mesh element, for the Helical-A model

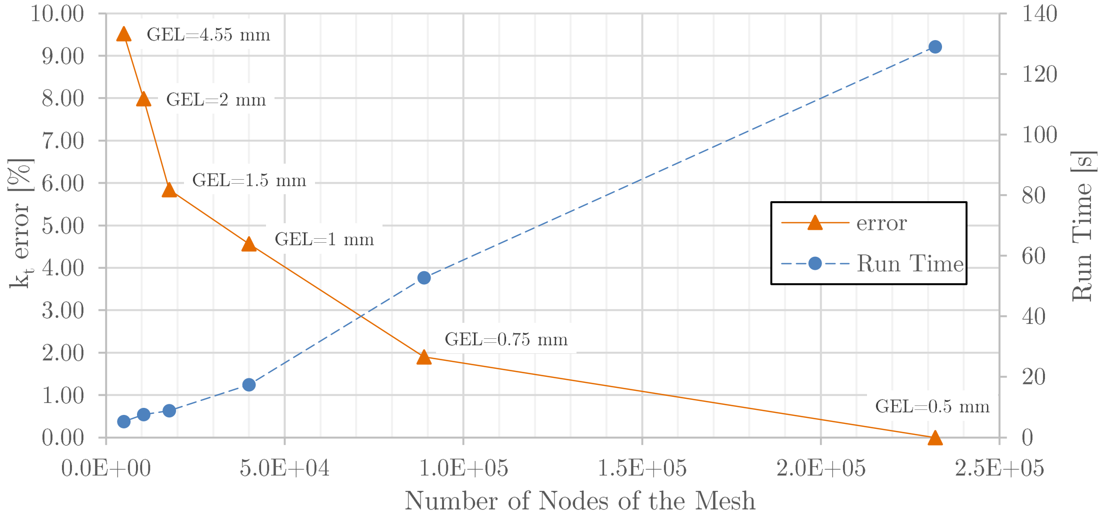

Fig. 3.10: Error and analysis time of the FEM results as a function of the number of nodes of the mesh, for the Helical-A model

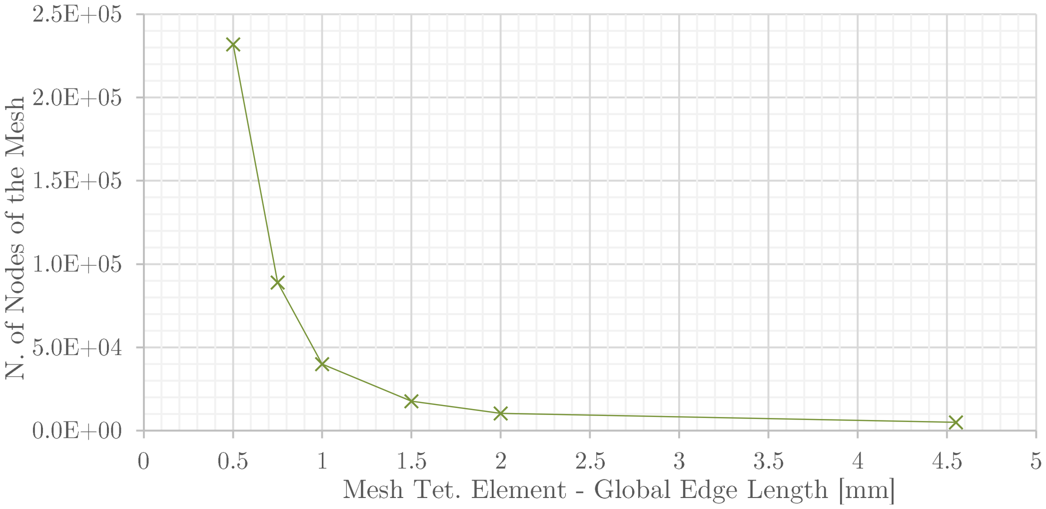

Fig. 3.11: Number of mesh nodes as a function of the average size of the tetrahedral element, for the Helical-A model

The run time is displayed in the ".log" file generated by the Nastran run. It can be observed that the number of nodes increases asymptotically as the GEL parameter decreases in the size of the mesh elements (Fig. 3.11), in fact for a zero GEL it would have infinite nodes.

If we consider the trend of the error with respect to the number of nodes instead of the size of the elements, we can observe a certain convergence as the number of nodes increases (Fig. 3.10). Unfortunately already for a GEL of 1 mm there is an important number of nodes but still an error of about 5%. For example, if you want to obtain results with errors of less than 1%, you will need a number of mesh nodes greater than 1.5E+05 (Fig. 3.10) and therefore select a GEL smaller than 0.65 mm (Fig. 3.9). The choice will have to be weighed in each case for the different conditions, since these results are valid for this specific case. However, for later studies and for the characterization of the influence of geometric parameters on the performance of the spring, I will refer to this convergence analysis to estimate the error or choose the refinement of the mesh.

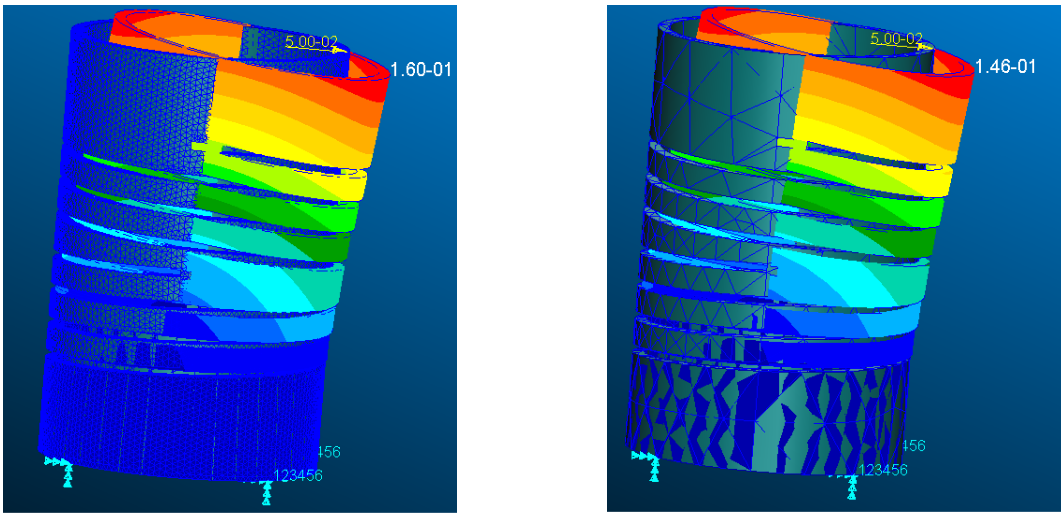

Fig. 3.12: Comparison of the two extremes of the convergence analysis, i.e. with GEL of 0.05 mm and then of 4.55 mm

It can also be observed from the results that a mesh refinement always leads to results with greater deformations and vice versa a coarser mesh provides increasingly stiffness results, this can be explained by the fact that as the mesh refinement increases and therefore the number of nodes, the total number of degrees of freedom of the structure increases and it will be more allowed to deform. This should be kept in mind for subsequent studies.

3.1.3 Helical-A Model: FEM Modal Analysis

In order to carry out a preliminary modal analysis, I choose a mass of about 1 kg to be attached to the end of the coil spring, model Helical-A. This would represent the test mass of the accelerometer and is modelled as a steel cube with a side length of 50 mm of the same material and therefore density as the spring. The model is defined with a finer mesh for the spring and a rougher one for the test mass and a modal analysis, Nastran code SOL 103, is performed.

For the spring I choose to use the automatic mesh with a *Global Edge Length* (GEL) of 4.55 m, therefore the least refined one from the convergence analysis study done previously (see Fig. 3.12). This is to avoid an excessive computational cost, in fact the modal analysis in this case employed about twice the resources compared to the static case seen previously. However we know from the previous analysis that with this type of mesh we will have an overestimation error of the static stiffness of about 10% (see Tab. 3.3, page 21) and therefore, since each natural frequency depends on the root of the generalized stiffness of that mode, we will have to take into account a correction factor of 0.95, thus an acceptable error:

Vibrational mode diff. equation: $m_{gener} \cdot \ddot{\theta} + K_{gener} \cdot \theta = 0$

Mode natural frquency: $f_n = \dfrac{\omega_n}{2\pi} = \dfrac{1}{2\pi}\sqrt{\dfrac{K_{gener}}{m_{gener}}}$

Correction for rough mesh: $K_{gener,real} \approx 0.9 \cdot K_{gener,GEL=4.55}$

$$f_{n,real} \approx \sqrt{0.9} \cdot f_{n,GEL=4.55}$$

$$f_{n,real} \approx 0.95 \cdot f_{n,GEL=4.55}$$

The Nastran SOL 103 modal analysis is solved as an eigenvalue problem with the *Lanczos method*. The results obtained for the first 5 modes of vibration of the system are reported as follows, in order of increasing frequency:

N. Mode	**Eigenvalue**	**Generalized Mass**	**Generalized Stiffness**	**Natural Frequency** (f_n) **[Hz]**	**Corrected natural Frequency** ($0.95 \times f_n$) **[Hz]**
1	7.911080E+01	1.000000E+00	7.911080E+01	1.415592E+00	**1.34**
2	8.147144E+01	1.000000E+00	8.147144E+01	1.436557E+00	**1.36**
3	2.389233E+02	1.000000E+00	2.389233E+02	2.460081E+00	**2.34**
4	8.914480E+02	1.000000E+00	8.914480E+02	4.751909E+00	**4.51**
5	6.402901E+03	1.000000E+00	6.402901E+03	1.273528E+01	**12.1**

Tab. 3.4: FEM modal analysis results for the Helical-A model with a test mass of 1 kg

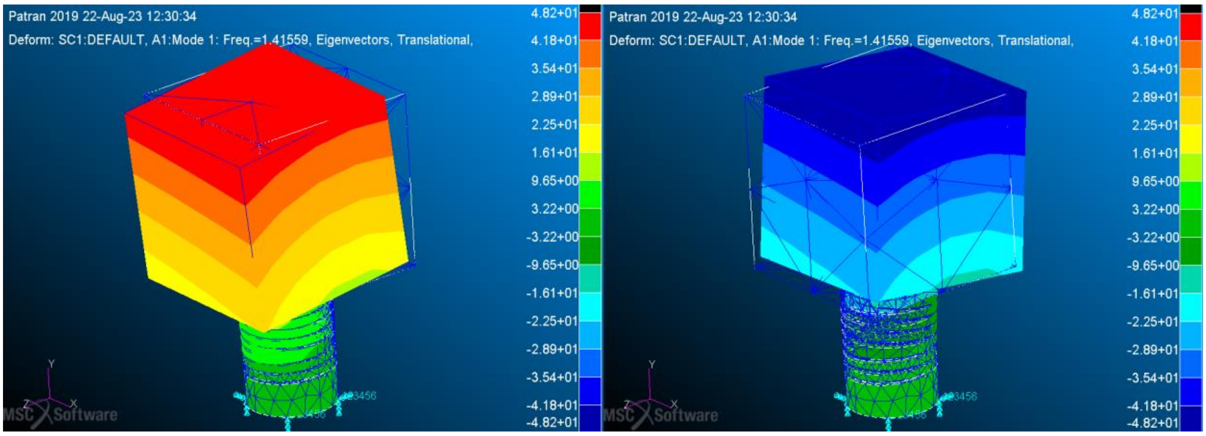

Fig. 3.13: F_1=1.42 Hz (FEM); 1.34 Hz (correction). First bending mode, Helical-A, 1 kg test mass.

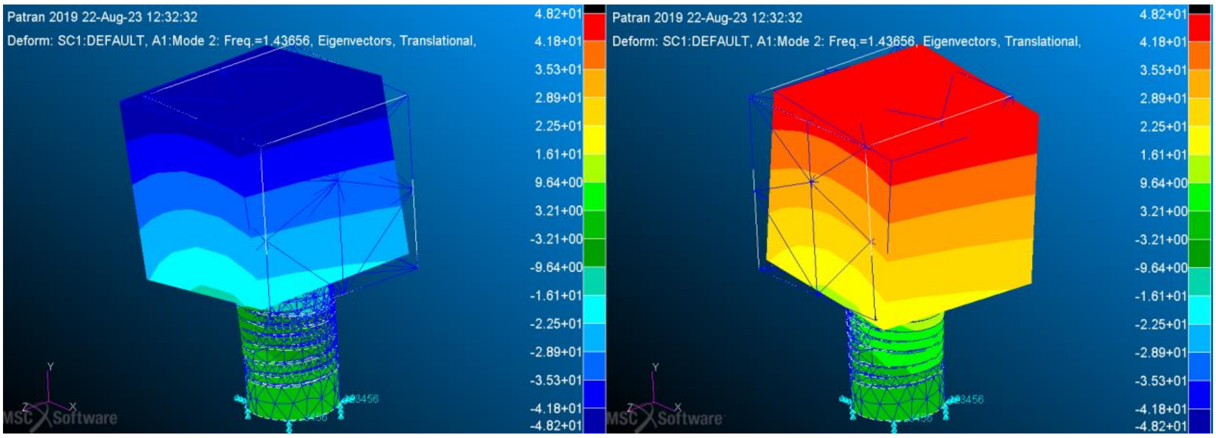

Fig. 3.14: F$_2$=1.44 Hz (FEM); 1.36 Hz (correction). Second bending mode, Helical-A, 1 kg test mass.

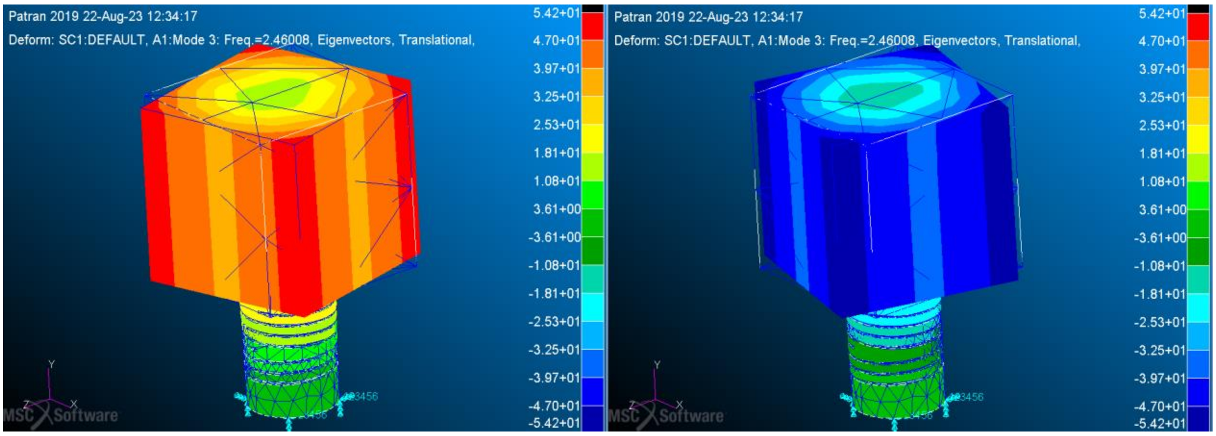

Fig. 3.15: F$_3$=2.46 Hz (FEM); 2.34 Hz (correction). First torsional mode, Helical-A, 1 kg test mass.

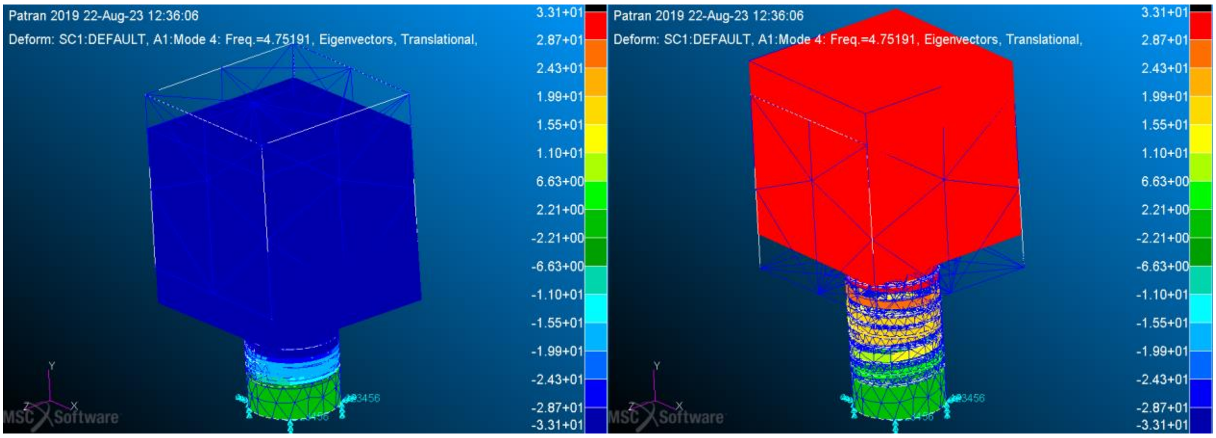

Fig. 3.16: F$_4$=4.75 Hz (FEM); 4.51 Hz (correction). First axial translational mode, Helical-A, 1 kg test mass.

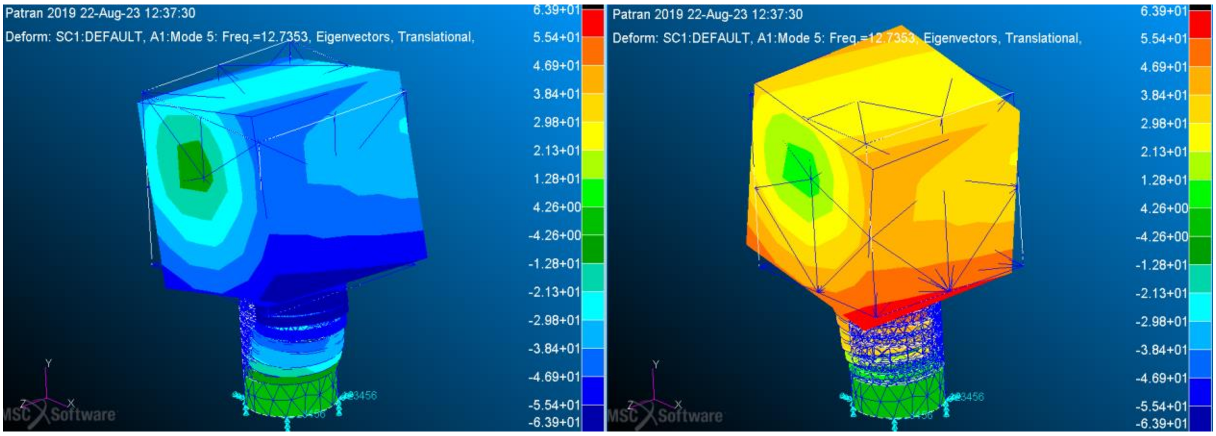

Fig. 3.17: F_5=12.7 Hz (FEM); 12.1 Hz (correction). Second torsional mode, Helical-A, 1 kg test mass.

From the results of this preliminary modal analysis, important deductions can be made regarding the behaviour of a spring of this type:

- The first two modes are those of bending oscillations, which are of interest to us for application on the accelerometer. The oscillation is slightly diagonal due to the not perfect symmetry of a complex geometry such as that of the spring. The frequency is of the order of the Hz, an acceptable value even if still high for our objectives.
- The first torsional mode is already the third in frequency order and is therefore more influent than the axial translational one, with a frequency comparable to that of the first ones. This makes us understand that for this particular geometry the spring is not torsionally rigid enough for our purposes, perhaps because the wall is too thin. To improve this aspect one could intuitively look for a geometry with a greater radial thickness, which however would give excessive lateral stiffness and therefore a greater number of turns to restore a low frequency of the first two modes. An insight into the influence of geometry design parameters on modal behaviour is indeed needed.

3.1.4 Simplified Model for Modal Analysis

Referring to the simplified model with lumped parameters of the bending behaviour of the spring, seen as a torsional spring (see Fig. 3.4 on page 18) we want to make a comparison of the FEM results with those given by an analytical calculation of the system seen as an oscillating mass, with rigid rotation around a torsion spring acting as the pivot point.

This is therefore an undamped mechanical system free to oscillate with a single rotational degree of freedom, whose behaviour is described by the differential equation of equilibrium of dynamics:

$$I\ddot{\theta} + K_t\theta = 0$$

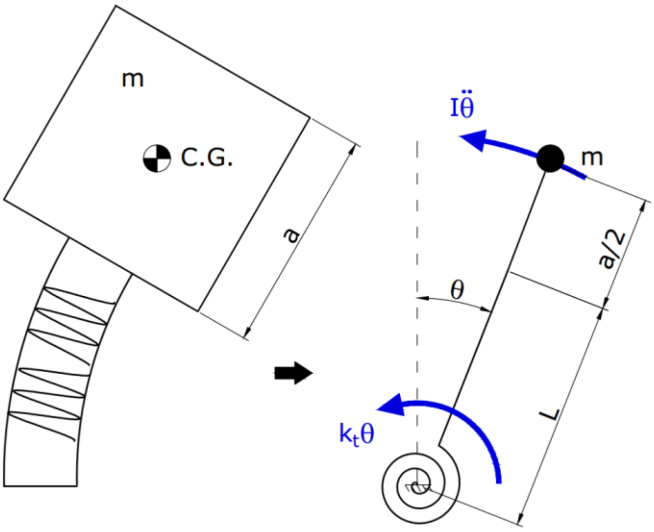

Fig. 3.18: Simplified model to find the bending mode frequency for an Helical spring with test mass

The mass of the simplified model is lumped and free to rotate rigidly around a fulcrum with a distance equal to that of the centre of mass from the base of the spring, that is equal to the length of the spring L, to which a 0.05 mm separator must be added (an artifice necessary for the assembly of the spring and the cube in the CAD-FEM model), plus half of the cube length $a/2$ where the centre of mass is located. The forces involved are those of the elastic return of the torsional spring, which represents our Helical type spring with a bending mode, and the force due to the rotational inertial acceleration of the mass around the pivot point.

The *dynamic equilibrium equation* of the system will be:

$$I\ddot{\theta} + K_t\theta = 0$$

With:

- $I = I_0 + m \cdot r^2$

  Moment of inertia around the rotation centre, according to the *Huygens–Steiner theorem*, where I_0 is the second moment of inertia relative to the cube centroid.

  $$m = V \cdot \rho = (50\,mm)^3 \cdot 7.85E - 09\frac{t}{mm^3} = 0.000981\,t \cong 1\,kg$$

  $$r = 0.05\,mm + L + \frac{a}{2} = 38.5\,mm + \frac{50}{2}mm = 63.5\,mm$$

  $$I_0 = m\frac{a^2}{6} = 0.409\,t\,mm^2$$

- $K_t = 8.63\,\frac{Nmm}{deg} = 494\frac{Nmm}{rad}$

  Torsion spring elastic constant, obtained from the FEM static analysis for a mesh GEL of 4.55 mm (see Tab. 3.3 on page 21), the same mesh used in the modal analysis for a bending oscillation in the *xy* plane of the model.

The equation can be reduced to:

$$\ddot{\theta} + \omega_n^2\theta = 0$$

With:

- $\omega_n = \sqrt{\frac{K_t}{I}}$: Natural angular frequency of the oscillation

From which the frequency can be obtained:

$$f_n = \frac{\sqrt{\dfrac{K_t}{I_0 + m \cdot (L + \frac{a}{2} + 0.5\,mm)^2}}}{2\pi} \quad [Hz] \tag{3.1}$$

$$f_{n,semplif} = 1.69\,Hz$$

This now obtained frequency should refer to the second resonance mode, analogous to the first, according to the FEM modal analysis carried out previously, since the stiffness had been calculated with a bending in the *xy* plane of the model (see Fig. 3.7

on page 20), like that of the second bending (see Fig. 3.14 a page 26). Therefore this value must be compared with the one obtained from the FEM analysis:

$$f_{n,FEM} = 1.44\,Hz$$

We can consequently observe that the value is close but still with an error of almost 17% and this underlines the weaknesses of a simplified model for a complex geometry. This may be due to the fact that the pivot point of the solid rotation cannot be considered around a fulcrum at the base, meaning that both the previously made stiffness calculation and the frequency calculation are incorrect, because they were calculated with the wrong lever arm.

3.1.5 Rotation Centre Determination – Improved Simplified Model

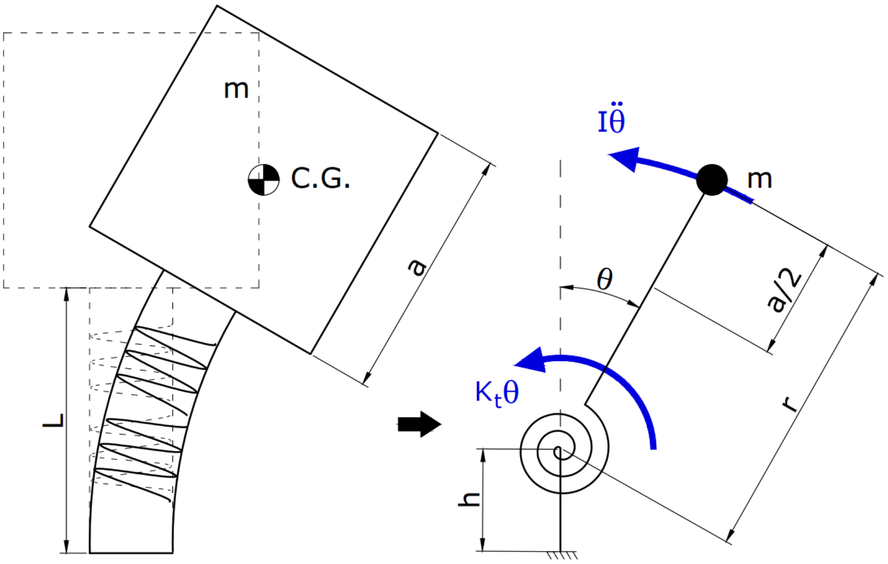

Fig. 3.19: Improved simplified model

The previous model could be adjusted by considering a rotation around a virtual pivot point at a certain height h from the base of the spring, which can be obtained starting from computing the stiffness K_t from the previous oscillatory dynamics equation (3.1), imposing the frequency as a datum, known from FEM analysis:

$$f_{n,FEM} = \frac{\sqrt{\frac{K_t}{I_0 + m \cdot r^2}}}{2\pi}$$

$$K_t = f_{n,FEM}^2 4\pi^2 (I_0 + mr^2)\ \left[\frac{Nmm}{rad}\right]$$

If we write the lever arm r as a function of h, position of the pivot point, we would get:

$$K_t = f_{n,FEM}^2 4\pi^2 m \cdot \left[I_0 + \left(L + 0.5\,mm + \frac{a}{2} - h \right)^2 \right] \left[\frac{Nmm}{rad} \right] \tag{3.2}$$

Now we want to write h instead, according to the relation we used previously (see page 18) to statically estimate the torsion spring elastic constant of the simplified model, but this time considering the lever arm of the improved model:

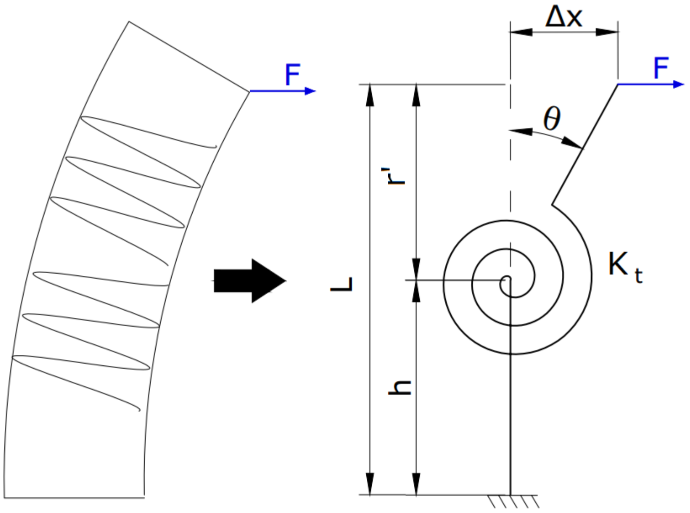

Fig. 3.20: Improved simplified model to find the bending stiffness for a spring with static analysis

$$K'_t = \frac{Fr'}{\vartheta}$$

With:

$$\vartheta \cong \left(\frac{\Delta x}{r'} \right) [rad]$$

$$h + r' = L = 38\,mm$$

Recalling that in the static calculation model there was no 0.5 mm separator of the modal analysis model, the static stiffness can be written as:

$$K_t = \frac{F(L-h)^2}{\Delta x} \left[\frac{Nmm}{rad} \right]$$

From which we obtain the following relation:

$$h = L - \sqrt{K_t \frac{\Delta x}{F}} \quad [mm] \tag{3.3}$$

It should be taken into consideration that h and K_t are interdependent in the (3.2) and (3.3) equations, therefore we can endure with an iterative or analytical solution:

- **Iterative solution**: We start from a zero value of h, therefore with the centre of rotation considered at the base and we substitute $h = 0$ in the dynamic equation (3.2) from which we find the corresponding stiffness. With this stiffness we repeat the static calculation of the position of the rotation centre (3.3) and so on iteratively:

1. $h_1 = 0\,mm$

$$K_{t,1} = f_{n,FEM}^2 4\pi^2 m \cdot \left[I_0 + \left(L + 0.5\,mm + \frac{a}{2} - 0\right)^2\right] = 355.7\,\frac{Nmm}{rad} \tag{3.2}$$

2. $$h_k = 0.5\,mm - \frac{a}{2} + \sqrt{K_t \frac{\Delta x}{F}} \; [mm] \tag{3.3}$$

3. $$K_{t,k+1} = f_{n,FEM}^2 4\pi^2 m \cdot \left[I_0 + \left(L + \frac{a}{2} - h_k\right)^2\right] \; \left[\frac{Nmm}{rad}\right] \tag{3.2}$$

4. - If $|h_{k+1} - h_k| < 0.01$ then *STOP*
   - If $|h_{k+1} - h_k| > 0.01$ then *Repeat 2.*

k	h_k $[mm]$	$K_{t,k+1}$ $\left[\frac{Nmm}{rad}\right]$
1	0.000	355.7
2	5.773	299.7
3	8.416	275.9
4	9.616	265.4
5	10.16	260.8
6	10.41	258.7
7	10.52	257.8
8	10.57	257.3
9	10.59	257.1
10	10.60	257.1
11	**10.60**	**257.0**

Tab. 3.5: Iterations results of the rotation centre and stiffness of the bending mode values

Results of the position of the centre of rotation and bending stiffness of the suspension are therefore obtained:

$$h = 10.6\,mm$$

$$K_t = 257\,\frac{Nmm}{rad}$$

- **Analytic solution**: The iterative method does not require complex calculations, however it is computationally expensive, requiring 11 iterations to obtain a satisfactory result. If instead we want to pursue an analytical method we have to solve the nonlinear system of two equations (3.2) and (3.3) to find a formulation that provides the exact results.

Replacing the (3.3) into the (3.2) equation:

$$K_t = f_{n,FEM}^2 4\pi^2 m \cdot \left[I_0 + \left(L + 0.5\,mm + \frac{a}{2} - h \right)^2 \right] \tag{3.2}$$

- $$h = L' - \sqrt{K_t \frac{\Delta x}{F}} \tag{3.3}$$

$$K_t = f_{n,FEM}^2 4\pi^2 I_0 + f_{n,FEM}^2 4\pi^2 m \cdot \left(L + 0.5\,mm + \frac{a}{2} - L + \sqrt{K_t \frac{\Delta x}{F}} \right)^2$$

$$K_t \left(\frac{\Delta x}{F} f_{n,FEM}^2 4\pi^2 m - 1 \right) + \sqrt{K_t} \left[2 f_{n,FEM}^2 4\pi^2 m \left(0.5 + \frac{a}{2} \right) \sqrt{\frac{\Delta x}{F}} \right] + f_{n,FEM}^2 4\pi^2 I_0 + f_{n,FEM}^2 4\pi^2 m \left(0.5 + \frac{a}{2} \right)^2 = 0$$

We obtain a second degree equation if the variable $\sqrt{K_t}$ is considered instead:

$$C_1 \left(\sqrt{K_t} \right)^2 + C_2 \sqrt{K_t} + C_3 = 0$$

From the quadratic formula two solution can be resolved:

$$K_t = \left(\frac{-C_2 \pm \sqrt{C_2^2 - 4C_1C_3}}{2C_1}\right)^2 \tag{3.4}$$

With:

- $C_1 = \frac{\Delta x}{F} f_{n,FEM}^2 4\pi^2 m - 1$
- $C_2 = 2f_{n,FEM}^2 4\pi^2 m \left(0.5\,mm + \frac{a}{2}\right)\sqrt{\frac{\Delta x}{F}}$
- $C_3 = f_{n,FEM}^2 4\pi^2 I_0 + f_{n,FEM}^2 4\pi^2 m \left(0.5\,mm + \frac{a}{2}\right)^2$

Once K_t has been calculated from (3.4), h is obtained through the (3.2) equation. The rotation lever arm of the mass-spring system can also be obtained as:

$$r = L + 0.5\,mm + \frac{a}{2} - h$$

The first solution of the (3.4) equation will give the following values:

$$K_t = 48.183\ \frac{Nmm}{rad} = 0.841\ \frac{Nmm}{deg}$$
$$h = 26.139\,mm$$
$$r = 37.362\,mm$$

The second solution of the (3.4) equation provides instead:

$$K_t = 256.98\ \frac{Nmm}{rad} = 4.485\ \frac{Nmm}{deg}$$
$$h = 10.607\,mm$$
$$r = 52.893\,mm$$

The second analytical solution is the same attained by the iterative method and provides reasonable values, while the first would indicate a rotation pivot point too far above the base and therefore physically impossible, with a stiffness value resulting only as a mathematical artifice. Therefore this second analytical solution is chosen to model the bending oscillation behaviour with the lumped parameter model of the "pendulum" analogy, as shown in the following figure.

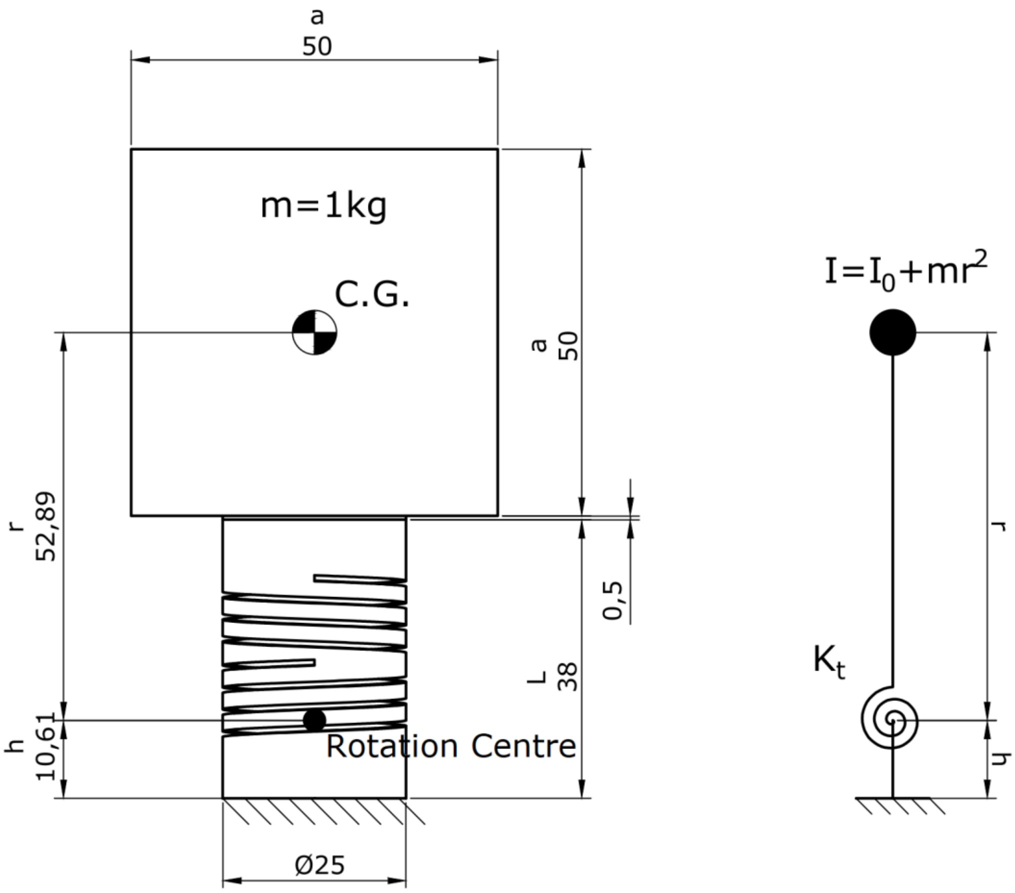

Fig. 3.21: Dimensioned CAD of the results of the rotation centre position computation of the bending oscillation mode of the Helical-A

3.2 Influence of the Geometry on the Modal Behaviour

Using the previously analysed Helical-A model as a starting base, we want to study how the behaviour of an elastic system of this type changes as the design parameters vary. The influence of the material and the external diameter will be studied in the next chapter and will be the criteria for choosing from different design proposals, while the number of coil starts is fixed at 1 to minimize stiffness, subsequently will be imposed a number of coils and size of the carving in order to minimize the thickness of the coils to the limits allowed by traditional machining methods. In this paragraph we want to study instead the influence of the thickness of the wall, starting from the Helical-A model.

The behaviour is defined through modal analyses, in which we want to determine how the natural frequencies of oscillation vary and consequently the stiffness of the different modes of vibration. The objective is to obtain low frequencies of bending oscillation and a large torsional resistance which means a high frequency for the torsional mode around the longitudinal axis. For a thickness of 1 mm of the Helical-A model it was realized that the torsional stiffness was not high enough, as it resulted in a low frequency, the third in ascending order (see Fig. 3.15 on page 26).

As a starting point of this study, it was decided to keep the geometry of the Helical-A model unaltered and vary only the wall thickness parameter, i.e. by changing the diameter of the axial hole. Each analysis was done with an automatic mesh refinement, separately between the test mass and the spring. The test mass is always of about 1 kg and the properties assigned for the material are always fixed for a generic steel:

Elastic Modulus: $\mathrm{E} = 210000$ [MPa]
Poisson's Ratio: $\nu = 0.3$
Density: $\rho = 7.85\mathrm{e}{-9}$ [Ton/mm^3]

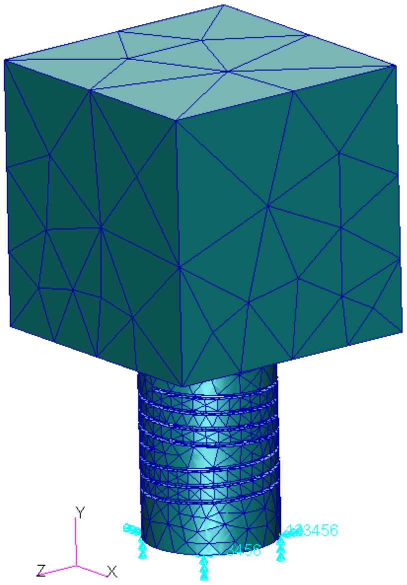

Fig. 3.22: Model for FEM modal analysis as the spring thickness varies, starting from the Helical-A model

Referring to the model in the figure above in which it can be appreciated the reference system, the clamp constraint at the base and the mesh, the frequencies of the first 6 resonance modes are called in the following manner:

- flex-yz [Hz]: Bending mode oscillation frequency in the yz plane
- flex-yx [Hz]: Bending mode oscillation frequency in the yx plane
- tors-y [Hz]: Torsional mode oscillation frequency around the y axis
- long-y [Hz]: Longitudinal mode oscillation frequency through the y axis
- tors-z [Hz]: Torsional mode oscillation frequency around the z axis
- tors-x [Hz]: Torsional mode oscillation frequency around the x axis

Subsequent modes are ignored because they have frequencies more than an order of magnitude larger and therefore of negligible influence. Results of the FEM modal analyses with Nastran SOL 103 as the wall thickness varies are shown below.

Wall thickness [mm]	**F1 [Hz]** flex-yz	**F2 [Hz]** flex-yx	**F3 [Hz]** tors-y	**F4 [Hz]** long-y	**F5 [Hz]** tors-z	**F6 [Hz]** tors-x
0.5	0.5723	0.5820	0.8813	1.758	4.690	4.751
1	1.407	1.432	2.471	4.721	12.74	12.89
2	2.927	2.948	7.119	11.57	33.42	33.78
3	4.120	4.088	13.31	18.22	55.04	55.60
4	5.300	5.268	21.45	25.51	77.57	78.64
5	6.425	6.294	30.59	33.65	98.59	100.0
6	7.271	7.203	40.48	42.01	114.9	116.5
7	8.222	8.046	51.41	52.25	131.4	134.1
8	8.807	8.678	62.13	61.84	143.2	146.1

Tab. 3.6: FEM modal analysis results as function of the wall thickness, for the Helical-A model

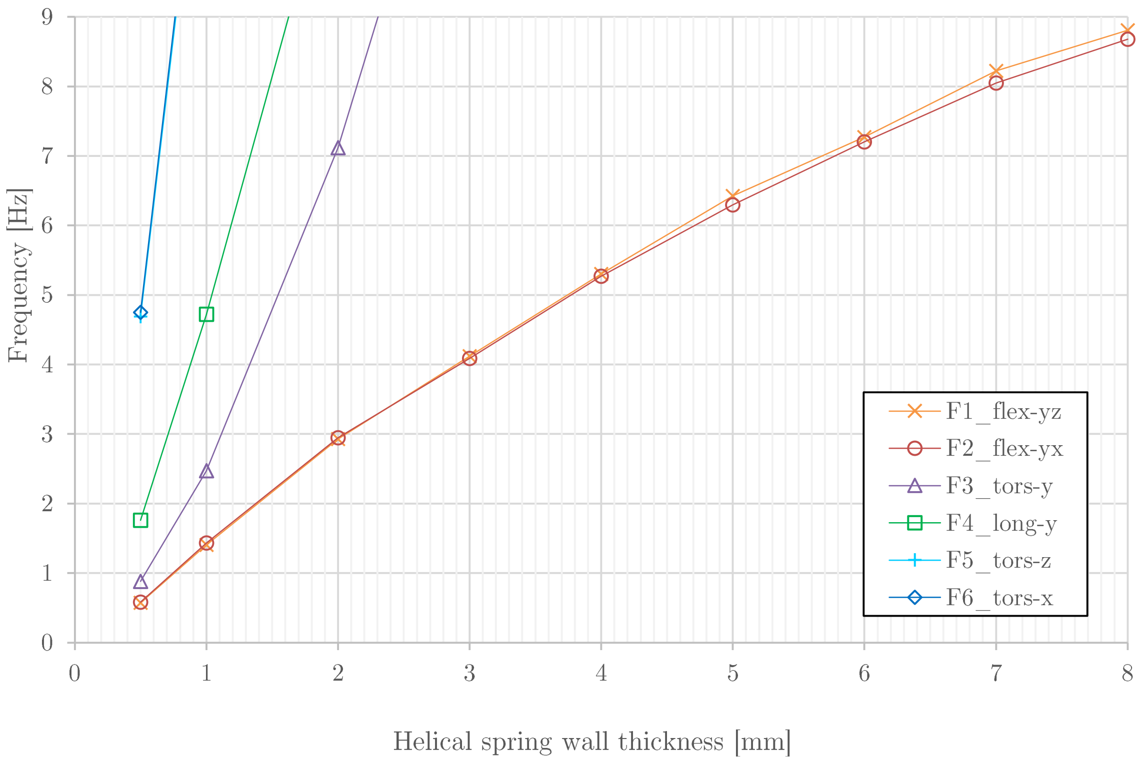

Fig. 3.23: Modal frequencies trends for the Helical-A spring model as the wall thickness varies, detail on the first modes of vibration, i.e. the bending modes of our interest

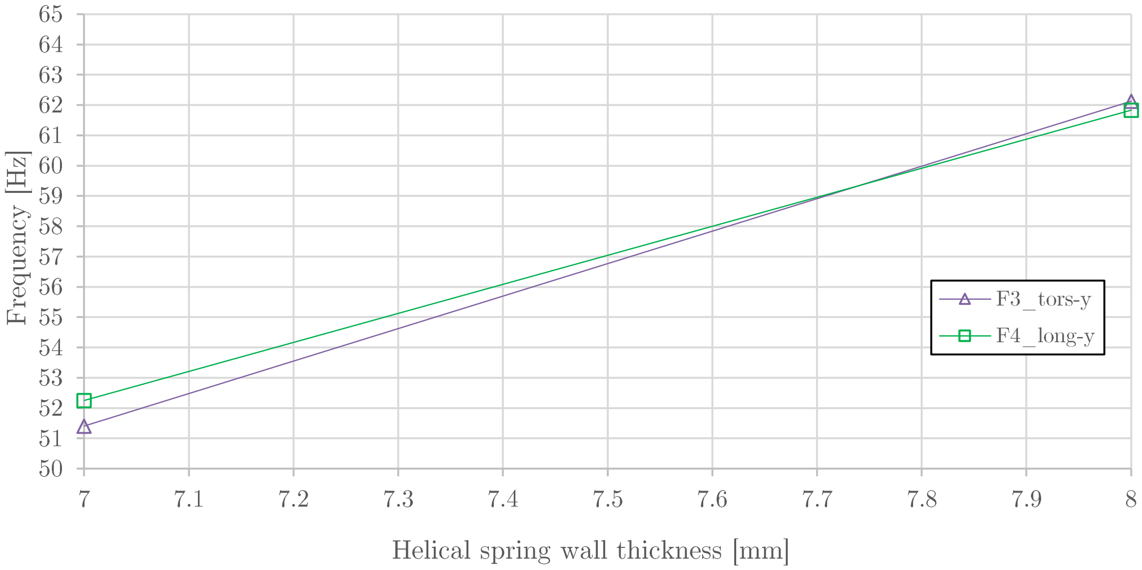

Fig. 3.24: Detail on the trend inversion between longitudinal and torsional frequencies

It can be observed that increasing the thickness results in an increase for all the modal frequencies and that from a certain thickness onwards, the desired trend inversion takes place: for a radial thickness of 8 mm in fact the torsional stiffness becomes greater than the longitudinal one. This makes us understand that we cannot use small radial thickness even if they make the spring looser, because it is better to avoid excessive torsional flexibility.

3.3 Design Proposals

It is subsequently demanded to design a mass-spring system prototype for the accelerometer with an HELI-CAL® type suspension. The requirement is to obtain a resonance frequency of the bending mode lower than 1 Hz and preferably to have adequate axial torsional stiffness. As a constraint, it must be within the dimensions of a box of 40 × 40 × 70 mm. In this section the HELI-CAL® spring is kept with two spirals with a single start each and counter-rotating, adjusting the axial length of the spirals and the number and thickness of the coils in order to maximize flexibility using the geometric limits possible with machining and varying the external diameter for two cases: Model Helical-B and Helical-C.

3.3.1 Materials

The influence of the material on the modal behaviour of the test mass with the elastic suspension is evaluated, choosing from the materials available for the construction of HELI-CAL® springs [9] and for space applications:

- Inox Steel
- 7075-T6 Aluminium
- Beryllium-Copper alloy BeCu C17200
- Titanium BETA C

In space applications it is preferred to use materials with good electrical and thermal conductivity properties. For our purposes, density is also important, in order to obtain greater masses and therefore lower resonance frequencies, and also is the workability. Steel could bring problems related to magnetic induction, for this reason alternatives are being explored.

	Density ρ **[g/cm^3]**	**Young's Modulus E [GPa]**	**Poisson's Ratio** ν	**Yield stress** σ_y **[MPa]**
Inox Steel (15-5 PH) [10]	7.75	197	0.272	1172
7075-T6 Aluminium [11]	2.81	71.7	0.33	503
Beryllium-Copper C17200 [12]	8.25	130	0.30	965-1205
Titanium Beta (UNS R58153) [13]	4.75	82	0.33	770-1172

Tab. 3.7: Mechanical properties of the proposed materials for the Helical suspension prototype

	Electrical Conductivity σ **[S/m]**	**Thermal Conductivity** λ **[kcal/hm°C]**	**Thermal Expansion [µm/m°C]**
Inox Steel (15-5 PH) [10]	9.79E-07	18.4	11.4
7075-T6 Aluminium [11]	1.94E+07	130	23.6
Beryllium-Copper C17200 [12]	1.13E+07	115	17.5
Titanium Beta (UNS R58153) [13]	7.0E+05	8.1	8.5

Tab. 3.8: Physical properties of the proposed materials for the Helical suspension prototype

The axial dimension of the two spirals of the previously studied Helical-A model is maintained, of 10.5 mm each, and we chose to vary the diameter of the internal hole and the parameters of the coil in order to alter the thickness of each coil. The mass-spring system could be made with the same material or using different materials for the test mass and the elastic suspension. If you wanted to decrease the bending resonance frequency, you should ideally use a high density material to increase the test mass, on the other hand it is preferred a high flexibility and therefore a low modulus of elasticity for the spring.

The prototype design study begins by trying to take the parameters to the extremes in order to achieve the desired requirements:

- A frequency of the bending mode in the order of less than 1 Hz, meaning that a very soft spring with many thin coils is preferred.
- An adequate torsion stiffness around the longitudinal axis, therefore the relative resonance frequency must be at least one order of magnitude higher than the bending one and, especially of the frequency of the longitudinal oscillation mode. This has been determined to be possible to obtain for large radial thicknesses.
- A total dimension of the spring-mass system as small as possible, respecting the limit box of 40 × 40 × 70 mm.

3.3.2 Helical-B Model

In order to ensure that the requirements and limits are met, we start with a geometry of the following type, which we will call "Helical-B model" to distinguish it from that of the preliminary FEM study. The external dimensions are dictated by the common commercial models and the parameters of the coils by the available processing limits:

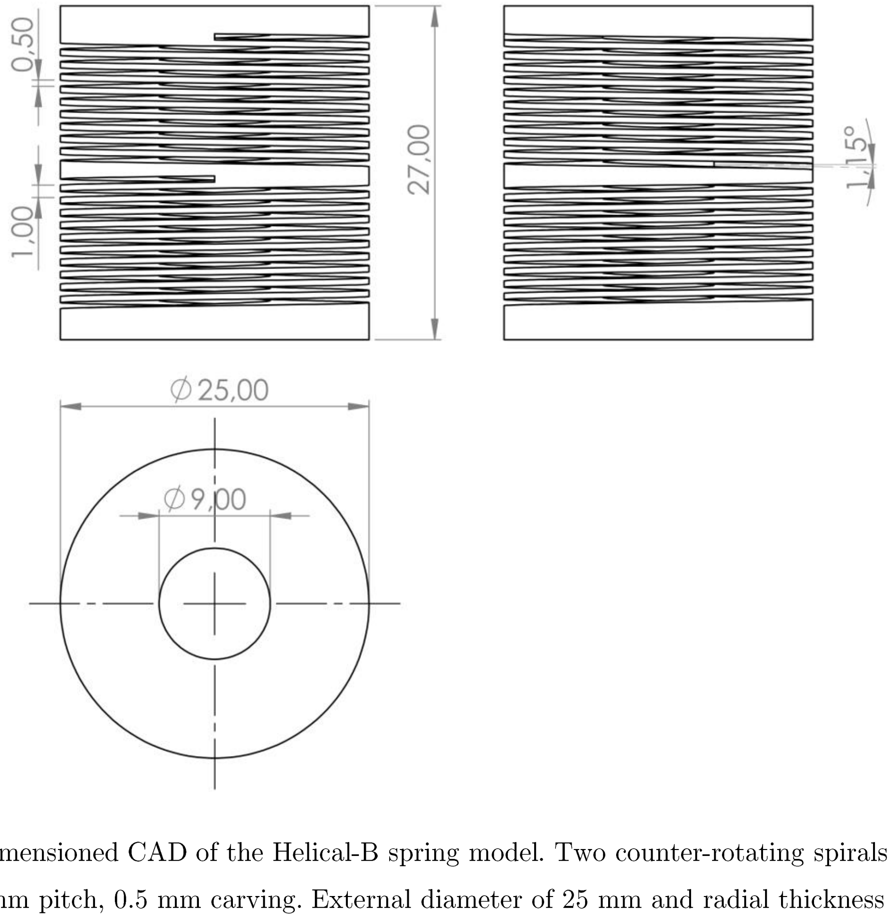

Fig. 3.25: Dimensioned CAD of the Helical-B spring model. Two counter-rotating spirals of 10.5 coils each, 1 mm pitch, 0.5 mm carving. External diameter of 25 mm and radial thickness of 8 mm

Compared to the Helical-A model, the diameter and extension of the spiral section are maintained while the section that does not participate in the bending is reduced to a minimum, in order to reduce axial length. The geometry of the spring derives from the optimization of the geometric parameters with the scope of achieving the desired requirements, based on the study of the influence of the geometry on the elastic characteristics, previously made and according to construction limits.

- For the two spirals, the number of coils (10.5) and the pitch (1 mm) are selected in order to have a thickness (0.5 mm) of the coils as small as possible according to commonly used construction techniques, so as to make the spring softer. The carvings will therefore be 0.5 mm thick;
- The radial thickness (8 mm) is chosen in order to obtain a much higher torsional stiffness around the axial direction than the bending and longitudinal ones, thus to avoid spurious behaviour;
- Two counter-rotating spirals are present to decouple the axial translation and twist kinematics;
- Each spiral has only one coil start, thus it has two continuous spirals in order to minimize stiffness.

The test mass to be coupled will be a cube with a side of 40 mm, so that it remains within the limit box. In the subsequent figure we can see the dimensioned CAD of the mass-spring system of the Helical-B model, which falls within the requirement limit dimensions and of which the resonance frequencies will be established later.

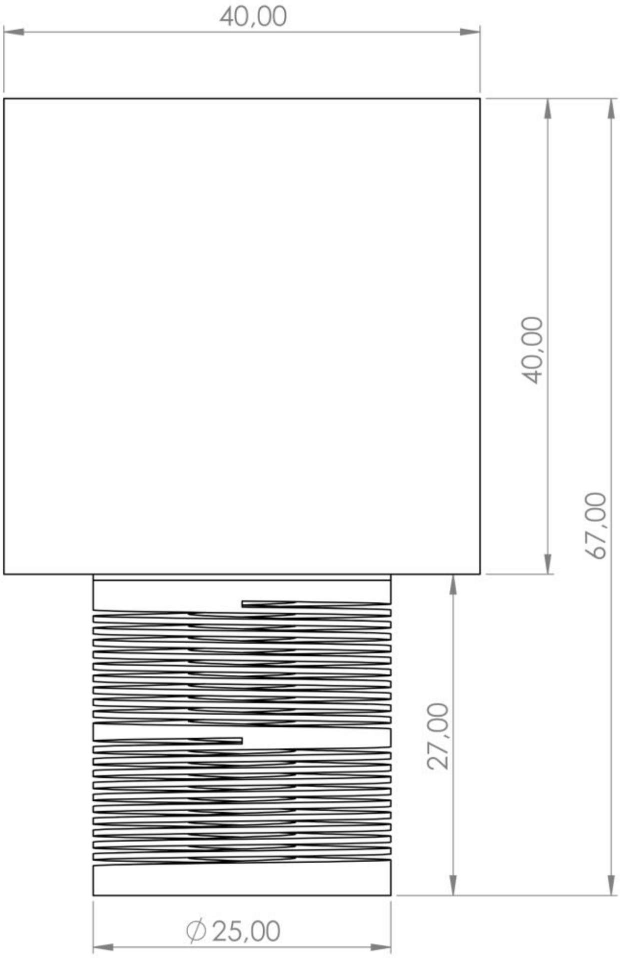

Fig. 3.26: Dimensioned CAD of the Helical-B suspension model for the subsequent modal analysis

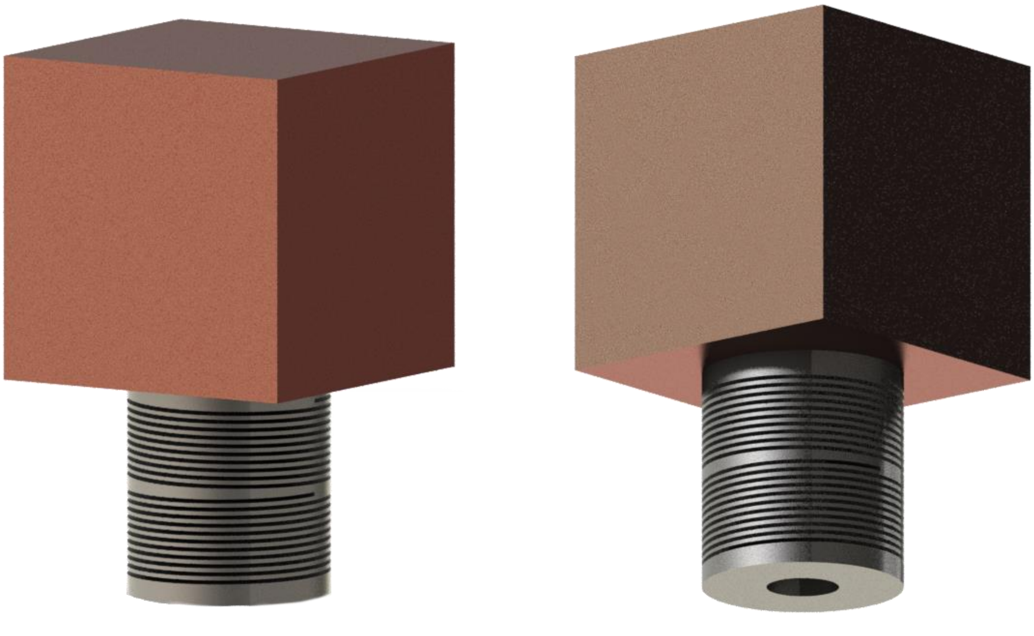

Fig. 3.27: Rendering of the suspension with a Titanium spring and a Beryllium-Copper test mass

3.3.3 Helical-B Model: Modal Analysis

The FEM *MSC Patran* software with *Nastran* solver is used to carry out the modal analysis (solution code Nastran SOL 103) for different materials. The system is clamped at the base of the spring and no loads are applied.

Material		**Resonance Modes (Nastran SOL 103)**					
Spring	**Test mass**	**F_1 [Hz]**	**F_2 [Hz]**	**F_3 [Hz]**	**F_4 [Hz]**	**F_5 [Hz]**	**F_6 [Hz]**
(Helical-B)	(40x40x40 mm)	flex_xz	flex_xz	long_y	tors_x	tors_z	tors_y
Inox Steel 15-5PH	Inox Steel 15-5PH	1.231	1.281	6.833	15.64	16.29	24.91
Aluminium 7075 T6	Aluminium 7075 T6	1.218	1.274	6.628	15.47	16.28	24.92
Titanium Beta R58153	Titanium Beta R58153	1.002	1.048	5.452	12.72	13.39	20.50
BeCu C17200	BeCu 17200	0.965	1.007	5.310	12.28	12.82	19.61
Titanium Beta R58153	BeCu C17200	0.761	0.796	4.171	9.945	10.47	15.61
Aluminium 7075 T6	BeCu C17200	0.712	0.744	3.919	9.461	9.958	14.62

Tab. 3.9: Modal analysis results of the mass-spring, model Helical-B, for different materials combinations

In the following figures are reported the first 6 resonance modes plots of the FEM modal analysis results for the case of the Titanium Beta spring and the Beryllium – Copper test mass.

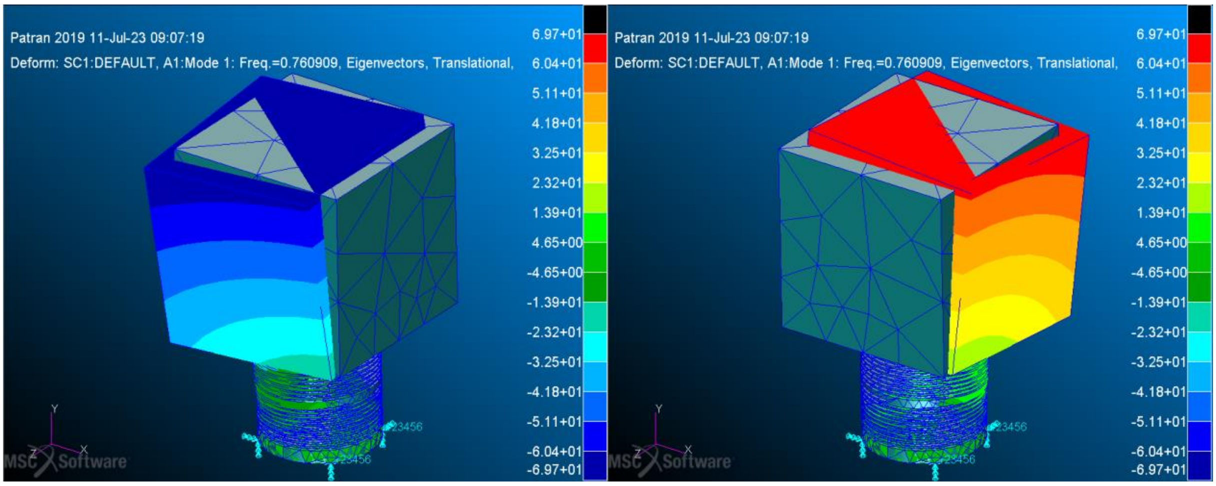

Fig. 3.28: F_1=0.761 Hz (FEM) First bending mode, Titanium Helical-B spring with a 0.53 kg Beryllium-Copper test mass

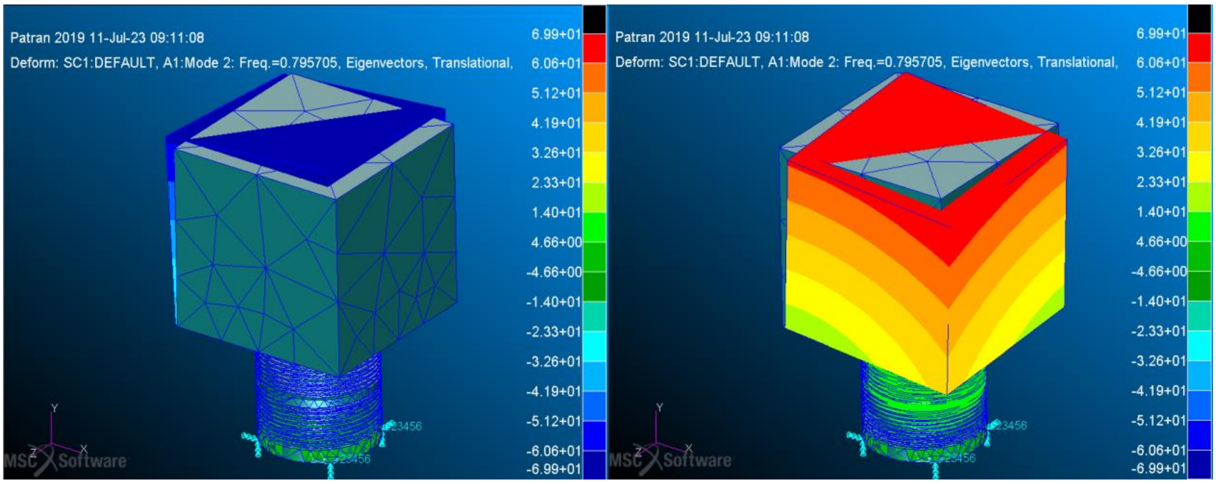

Fig. 3.29: F$_2$=0.796 Hz (FEM) Second bending mode, Titanium Helical-B spring with a 0.53 kg Beryllium-Copper test mass.

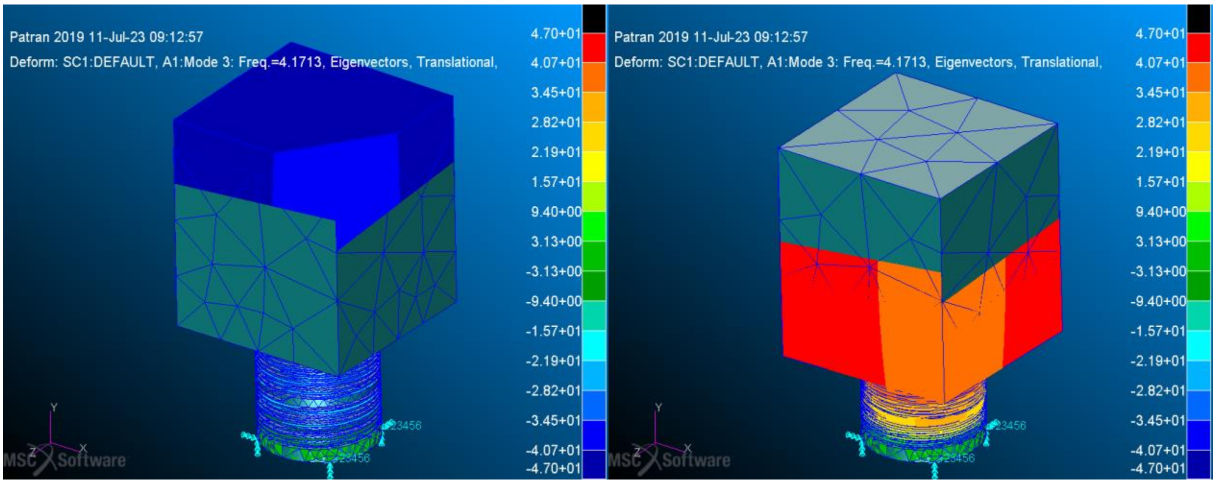

Fig. 3.30: F$_3$=4.17 Hz (FEM) First longitudinal mode, Titanium Helical-B spring with a 0.53 kg Beryllium-Copper test mass

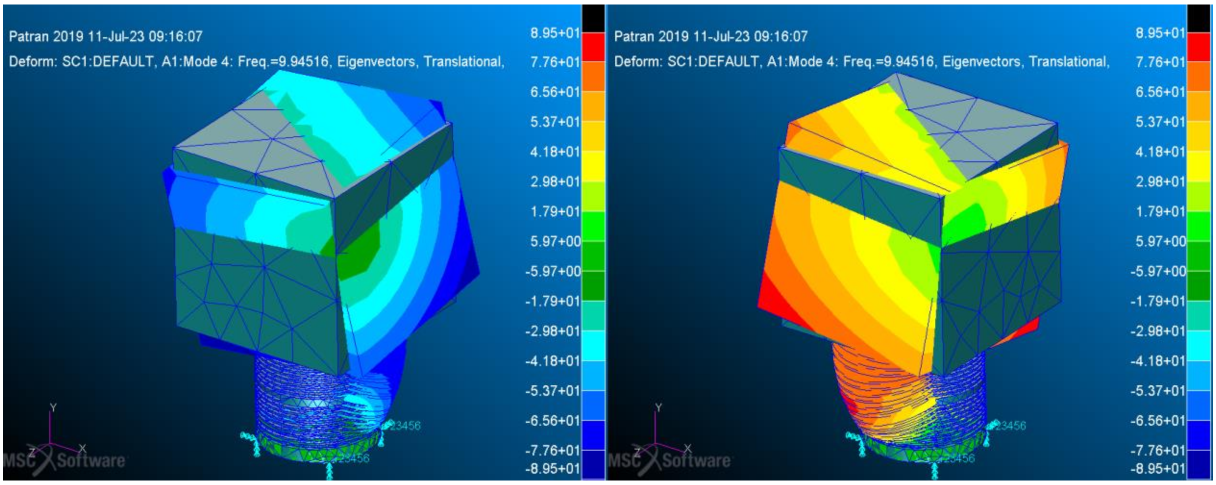

Fig. 3.31: F$_4$=9.95 Hz (FEM) First torsional mode, Titanium Helical-B spring with a 0.53 kg Beryllium-Copper test mass

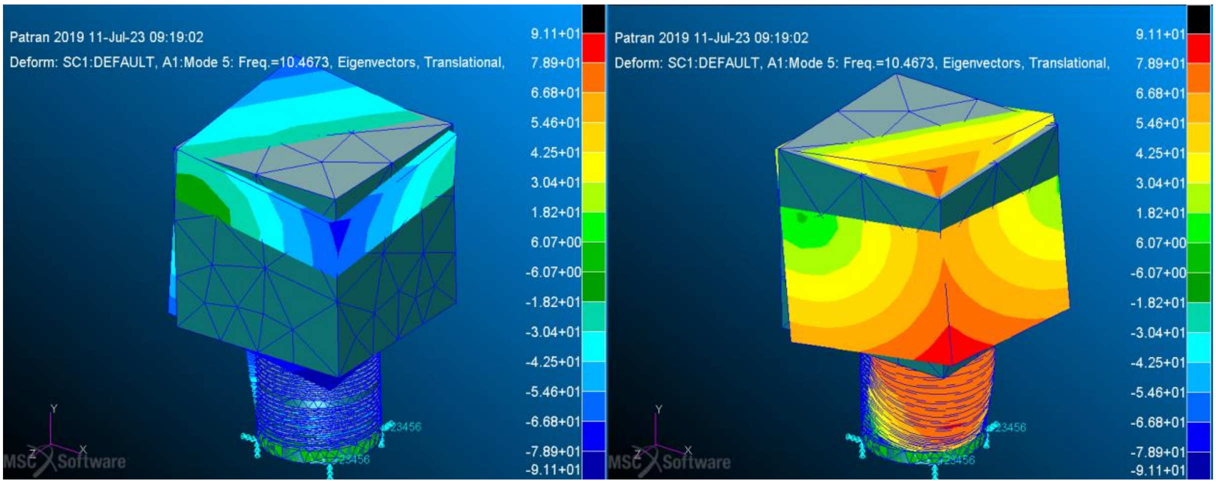

Fig. 3.32: F$_5$=10.47 Hz (FEM). Second torsional mode, Titanium Helical-B spring with a 0.53 kg Beryllium-Copper test mass

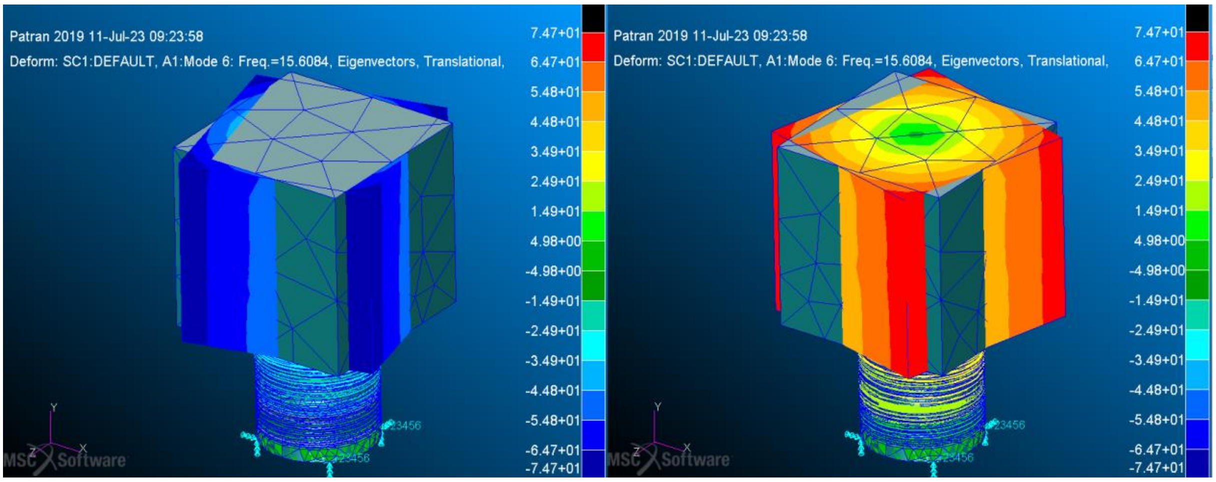

Fig. 3.33: F$_6$=15.61 Hz (FEM). Third torsional mode, Titanium Helical-B spring with a 0.53 kg Beryllium-Copper test mass

As mentioned before, in the context of space applications it is preferable to use materials with good thermal and electrical conductivity to avoid dangerous charge build-ups. In order to minimize the oscillation frequencies, the softest material should be selected for the spring, which is aluminium, while the densest one should be chosen for the test mass, therefore the beryllium-copper alloy. This solution provides indeed the lowest frequencies in the modal analysis results (see Tab. 3.9 on page 43). Furthermore, they are also the materials with the best electrical and thermal conductivity characteristics (see Tab. 3.8 on page 39) among those proposed. However, in this case it is preferable to use titanium for the spring, because it has better thermal expansion characteristics which would invalidate the predictability of the elastic behaviour in the case of aluminium, and for its better mechanical resistance characteristics (see Tab. 3.8 on page 39). Titanium can also withstand greater stresses thanks to its much higher yield strength than aluminium, a fundamental requirement for such a complex and delicate geometry that will have to be subjected to the heavy loads of a space launch.

The resonance frequencies obtained using titanium for the spring and the beryllium-copper alloy for the mass are not so different from those obtained using aluminium, thus justifying the final choice for the Titanium Beta C alloy spring, already widely used for HELI-CAL® type springs.

3.3.4 Helical-C Model

The axial dimension of the spring is near the limit to comply with the design volume constraints and the thickness and number of coils are at the limit of the machine processing capabilities, the only parameter that can therefore be changed is the external diameter of the spring, leaving the radial thickness of the previous case unchanged to maintain axial torsion stiffness.

This new spring model will be called "Helical-C model" and has the same geometric characteristics as the previous B model, except for the external diameter and internal diameter, to maintain a radial wall thickness of 8 mm. The maximum possible external diameter is selected, i.e. equal to that of the side of the cube of the test mass, which is 40 mm of length.

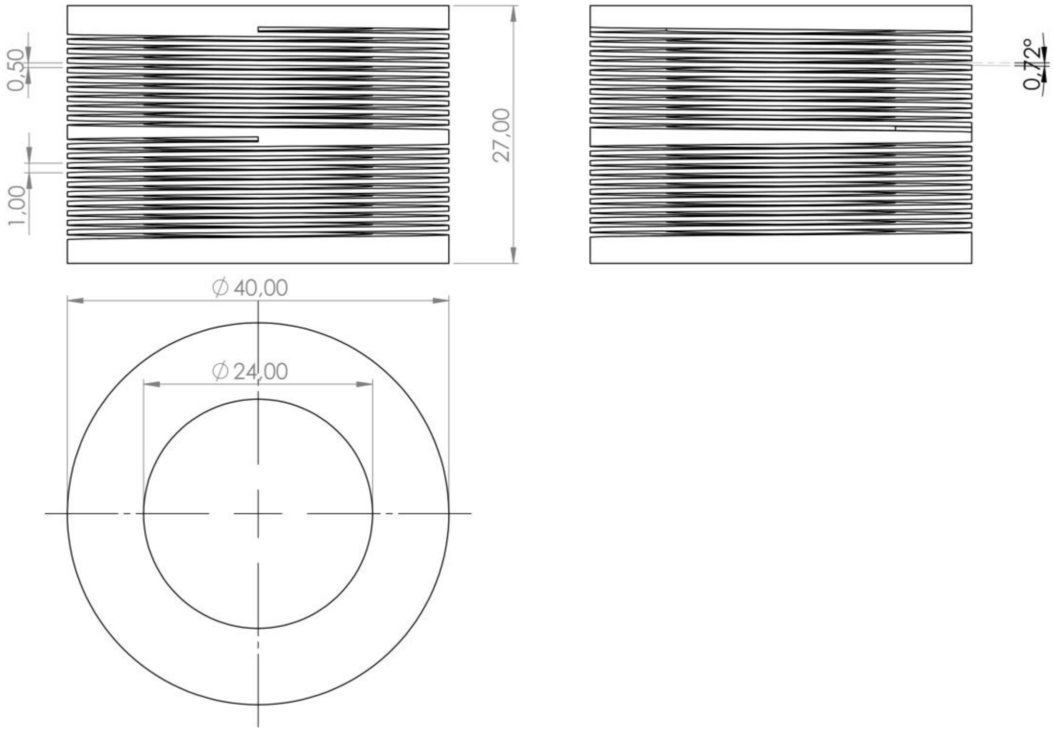

Fig. 3.34: Dimensioned CAD of the Helical-B spring model. Two counter-rotating spirals of 10.5 coils each, 1 mm pitch, 0.5 mm carving. External diameter of 40 mm and radial thickness of 8 mm

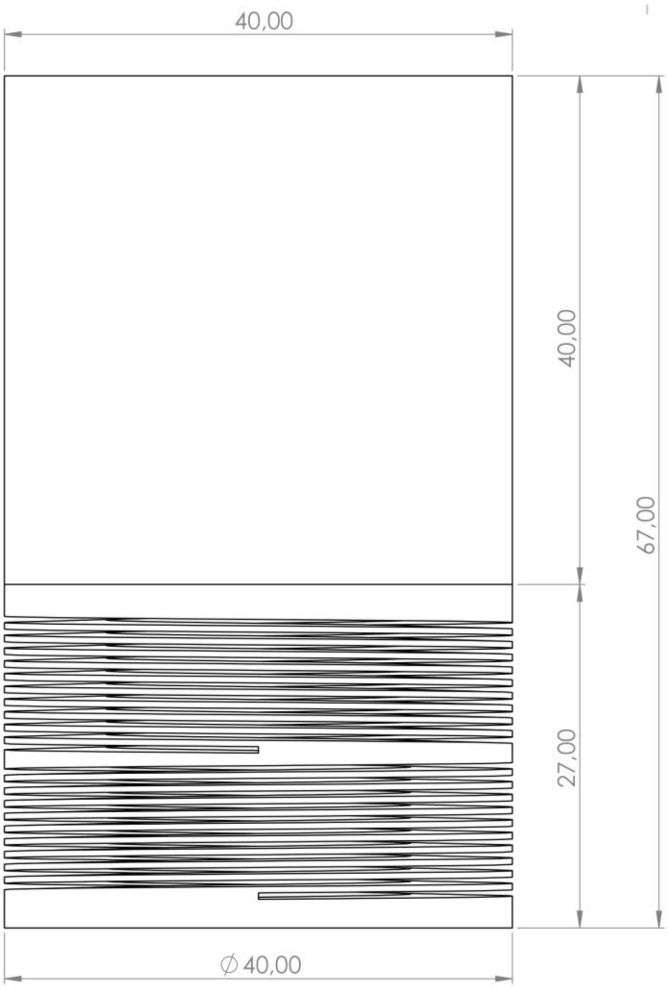

Fig. 3.35: Dimensioned CAD of the Helical-C suspension model for the subsequent modal analysis

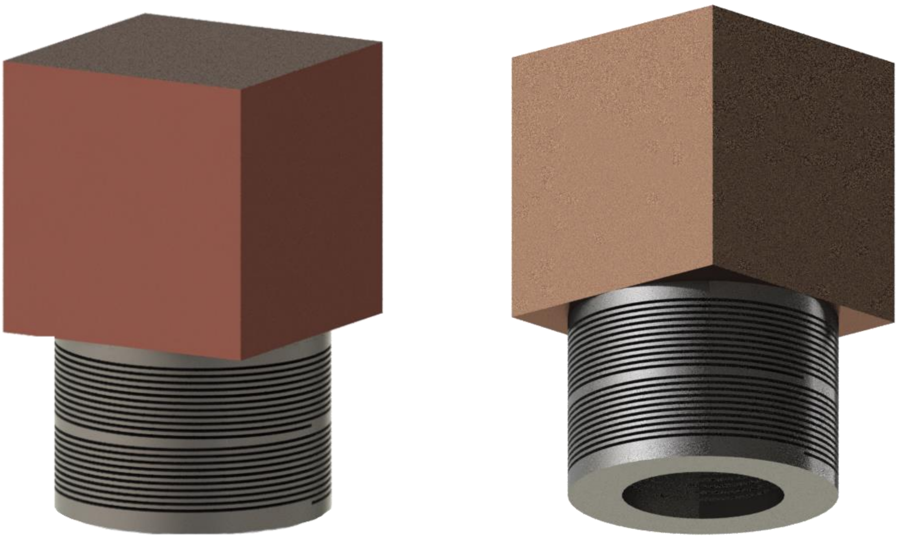

Fig. 3.36: Rendering of the suspension: enlarged Titanium spring with Beryllium-Copper test mass

3.3.5 Helical-C Model: Modal Analysis

The FEM *MSC Patran* software with *Nastran* solver is used to carry out the modal analysis (solution code Nastran SOL 103) for the aforementioned Helical-C suspension model. The system is clamped to the base of the spring and no loads are applied.

Material		**Resonance Modes (Nastran SOL 103)**					
Spring	**Test Mass**	**F_1 [Hz]**	**F_2 [Hz]**	**F_3 [Hz]**	**F_4 [Hz]**	**F_5 [Hz]**	**F_6 [Hz]**
(Helical-C)	(40x40x40 mm)	flex_z	flex_x	long_y	tors_x	tors_z	tors_y
Titanio R58153	BeCu C17200	0.437	0.438	1.134	5.121	5.153	11.27

Tab. 3.10: Modal analysis results for the Helical-C mass-spring system

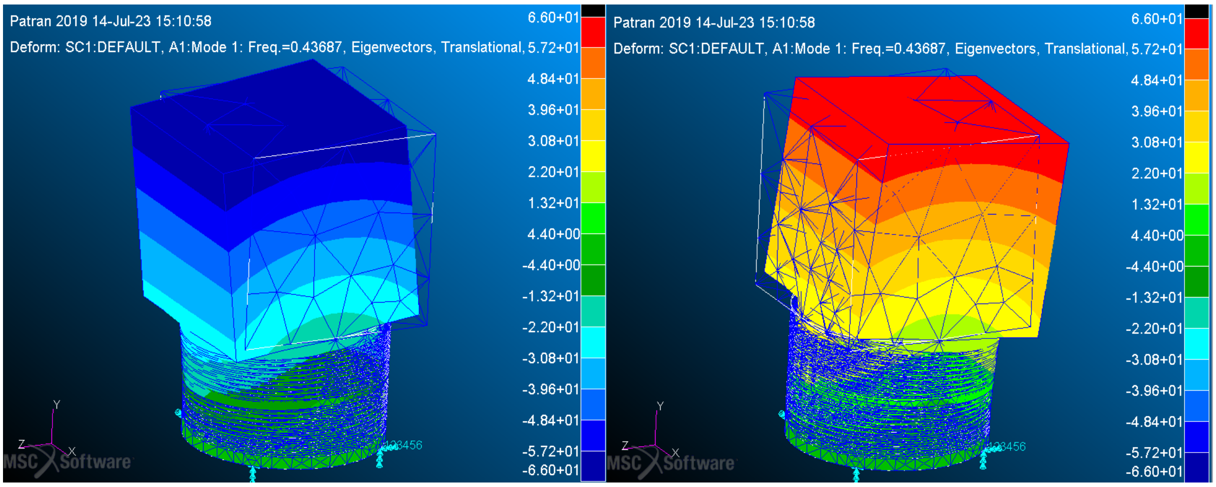

Fig. 3.37: F_1=0.437 Hz (FEM) First bending mode, Titanium Helical-C spring with a 0.53 kg Beryllium-Copper test mass

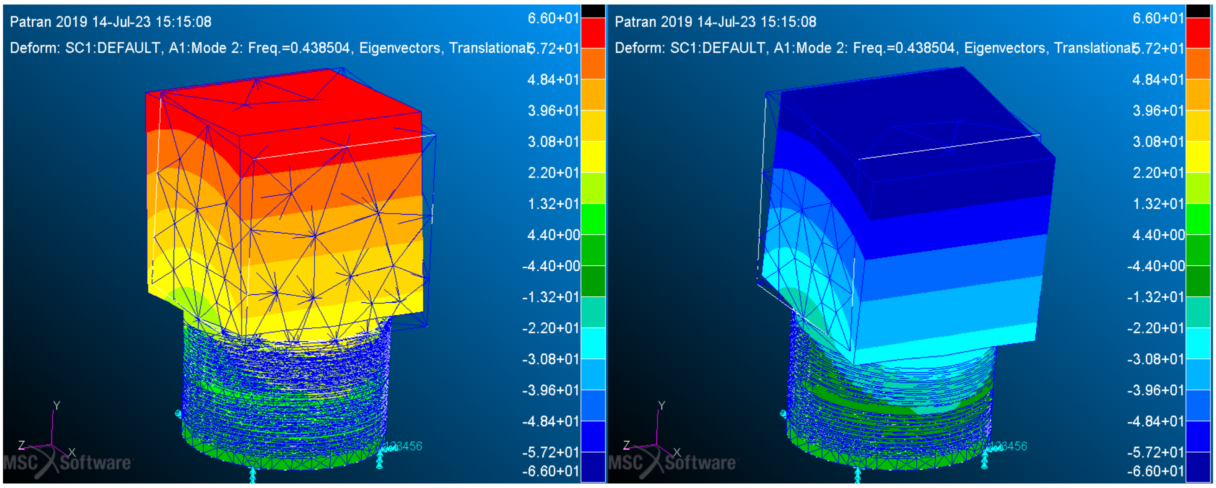

Fig. 3.38: F_2=0.438 Hz (FEM) Second bending mode, Titanium Helical-C spring with a 0.53 kg Beryllium-Copper test mass

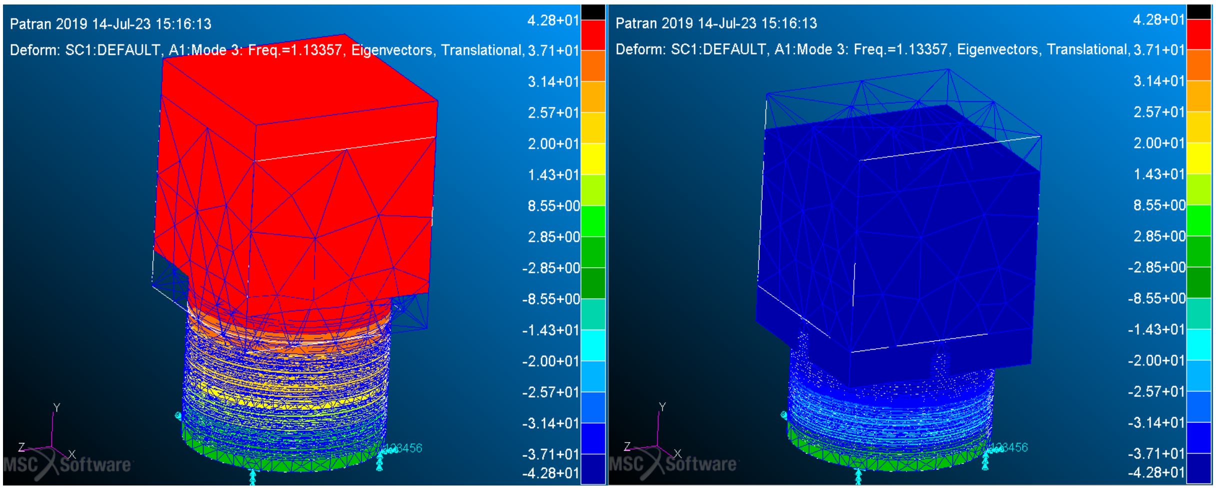

Fig. 3.39: F_3=1.13 Hz (FEM) First longitudinal mode, Titanium Helical-C spring with a 0.53 kg Beryllium-Copper test mass

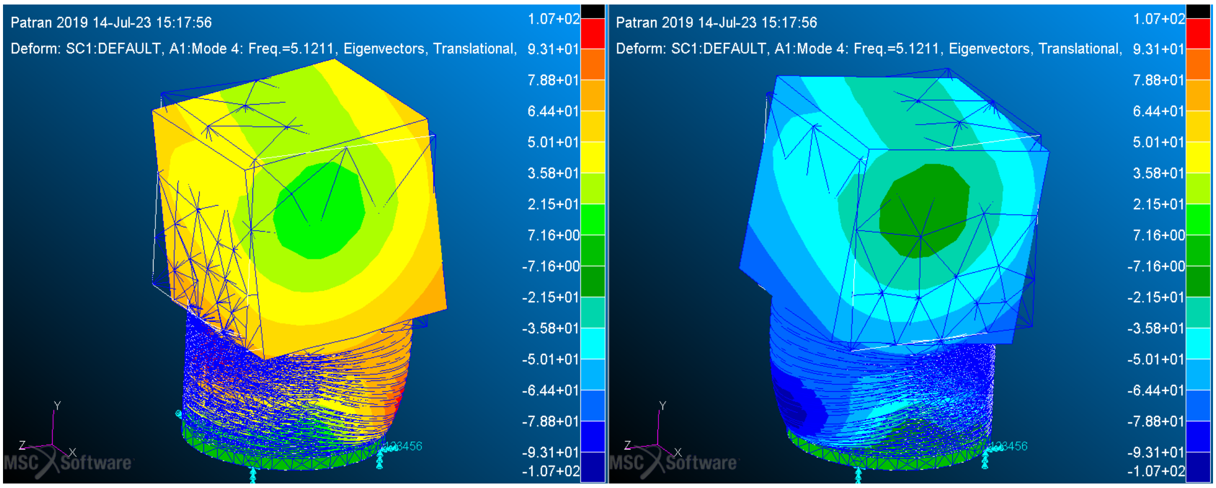

Fig. 3.40: F_4=5.12 Hz (FEM) First torsional mode, Titanium Helical-C spring with a 0.53 kg Beryllium-Copper test mass

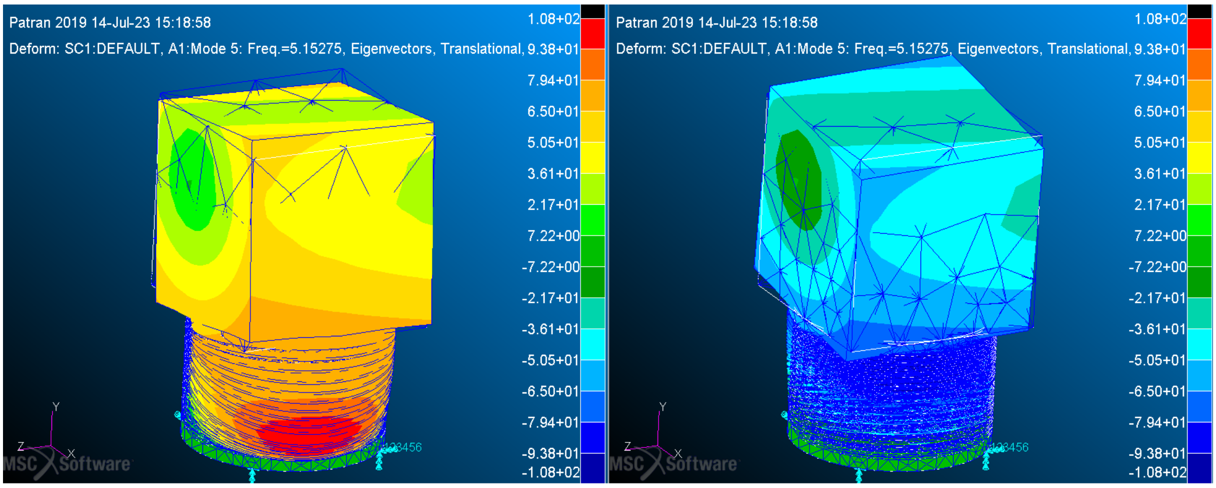

Fig. 3.41: F_5=5.15 Hz (FEM). Second torsional mode, Titanium Helical-C spring with a 0.53 kg Beryllium-Copper test mass

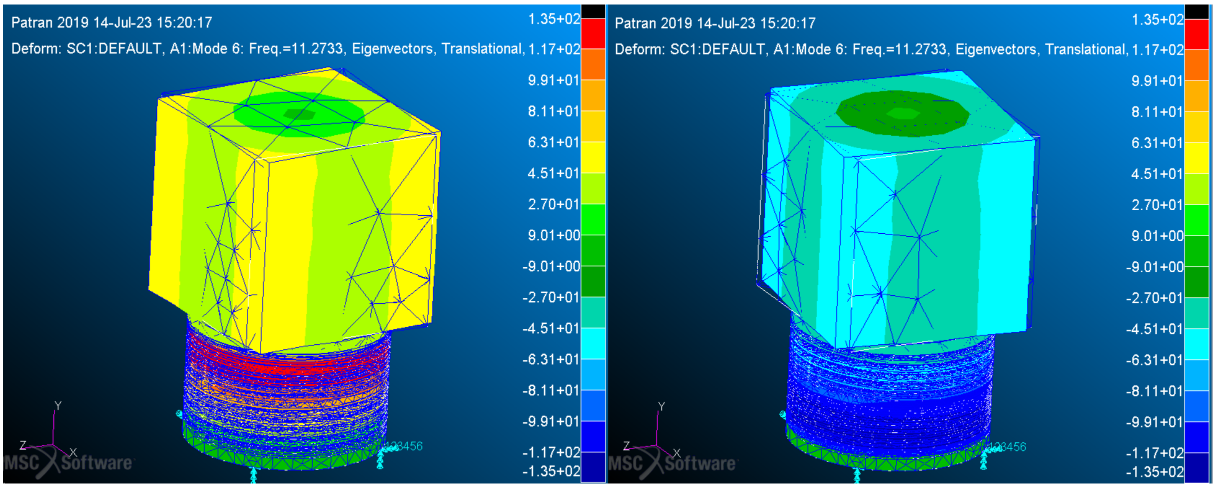

Fig. 3.42: F$_6$=11.3 Hz (FEM). Third torsional mode, Titanium Helical-C spring with a 0.53 kg Beryllium-Copper test mass

It can be observed that, compared to the previous case, all frequencies are almost halved, because the total length of the coils has been increased without changing the section, if we consider a beam analogy, thus increasing flexibility. It is also found that compared to the previous case, the main directions of oscillation are now parallel to the x and z axes and the two lateral bending and torsional modes are closer in frequency. This can be explained because an increase of the spring diameter, the revolution angle decreases and thus geometric asymmetries result to be dampened.

It is useful to recall that all of the previous results of modal frequencies are obtained with non-refined mesh FEM models and that the real results will be closer to lower frequencies, according to a correction of the type presented in the 3.1.3 subparagraph on page 24.

3.3.6 Assembly and Final Design Proposal

Once established that the prototype should be composed of:

- A Beryllium-Copper alloy cubic test mass of 40 mm of side length;
- A Titanium alloy HELI-CAL® type spring with 40 mm external diameter and 24 mm internal diameter, with two single coil start counter-rotating helices with a 1 mm pitch, 10.5 coils and 0.5 mm thickness for each coil.

It is proposed to assemble the components together and to the external support through threaded couplings. A construction solution for the Helical-C mass-spring system prototype is presented in the following figure.

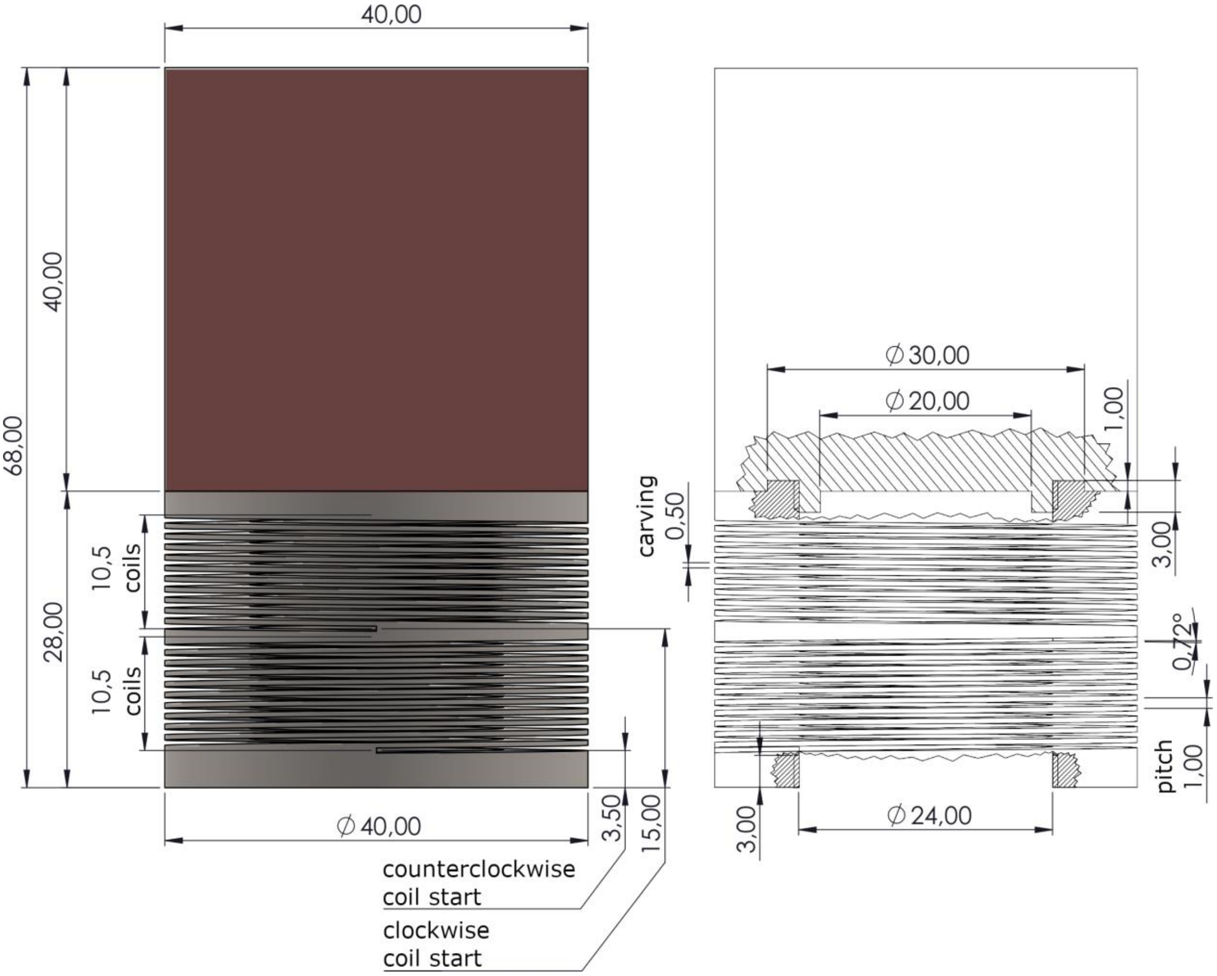

Fig. 3.43: Dimensioned CAD of the proposed suspension system, composed of a C17200 alloy test mass and a Titanium Beta C alloy spring, Helical-C model. Front and right view with cross sections details of the threaded couplings

Increasing the axial length from the bottom side does not affect the modal behaviour since the rotation lever arm is not changed, therefore the bending modal frequencies of the final proposal will be those of the previously FEM computed for the Helical-C model. Adjusting with the correction for mesh convergence we obtain:

Material		**Bending resonance mode**	
Spring	**Test mass**	**F_1 [Hz]**	**F_1 correction [Hz]**
(Helical-C)	(40x40x40 mm)	f_{n_FEM}	$0.95 \times f_{n\_FEM}$
Titanio R58153	BeCu C17200	0.437	0.416

Tab. 3.11: Natural frequency of the bending mode for the Helical-C model mass-spring system, final proposal

3.3.7 Static Analysis – Displacement Limits Determination

The allowable displacements of the components of the elastic suspension in response to an acceleration in a generic direction must be restricted for two reasons:

- To avoid reaching yield stress of the spring material
- To avoid mechanical interference between the coils

In order to establish the displacement limits and therefore the dimensions of a containment box to constrain the displacements of the test mass to avoid the aforementioned two phenomena, linear static analyses (Nastran SOL 101) will have to be carried out with the same FEM model used for the modal analyses of the previous paragraphs. The static model will need as boundary condition, in addition to the clamp at the base, an inertial load, in order to simulate the response of the elastic suspension to an acceleration.

If the maximum stress reached in the spring at the interference is lower than the yield strength of the material, then the problem of the yield can be excluded regardless because a greater displacement and therefore a greater stress than the one corresponding the interference is not possible.

The most critical cases for the displacement which define the maximum dimensions of a cubic containment cage are that of acceleration in the diagonal lateral direction and of longitudinal compression, as shown in the following figures.

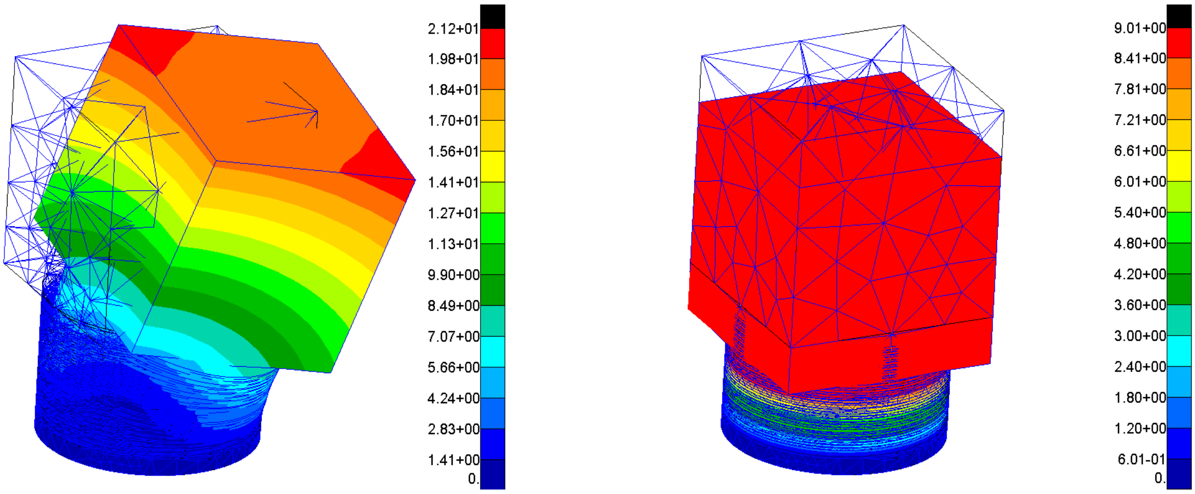

Fig. 3.44: Displacements [mm] plot for the Helical-C suspension in correspondence with the interferences in the two most critical cases

It is derived from these results that the displacement of the mass is limited by the interference of the coils in the lateral diagonal direction along to the x, z (horizontal) and $+y$ (vertical) directions while the deviation in the $-y$ direction is limited due to the interference of the coils in the longitudinal direction. The results of the maximum permitted displacements and of the corresponding maximum stress reached in the two cases in correspondence with the start of mechanical interference are reported below. The diagonal displacement is obtained by setting an acceleration in that direction, while the longitudinal one is obtained directly by setting the displacement of the mass.

a [m/s^2]	Δx [mm]	Δy [mm]	Δz [mm]	σ_{max} [MPa]
0.110	±13.3	+9.77	±13.4	10.5

Tab. 3.12: Maximum displacements of the test mass relative to the start of interference phenomena between the spring coils due to bending oscillation

Δy [mm]	Δx [mm]	Δy [mm]	Δz [mm]	σ_{max} [MPa]
-9	0	-9.00	0	18.0

Tab. 3.13: Maximum displacements of the test mass relative to the start of interference phenomena between the spring coils due to longitudinal oscillation

It turns out that even if interferences were to occur and therefore in correspondence of the maximum permitted displacements, the maximum stress reached would be of the order of 1E+01 MPa and therefore negligible stresses compared to the 770-1172 MPa yield stress of the Titanium Beta alloy [13] of which the spring is made. This means that the displacements will be limited only by the interference phenomenon and that the problem of yielding can be ignored if these deviations are respected.

A constraint system of the displacement of the components consisting of a containment cage for the mass and mechanical stops for the floating supports should allow for smaller deviations than the one we just obtained, also because we are talking about macroscopic deviations and compactness requirements must be respected. The test mass (40 × 40 × 40 mm) containment box, for example, can have the following dimensions for the proposed design model:

	x [mm]	y [mm]	z [mm]
Helical-C	45	45	45

Tab. 3.14: Proposed dimensions for the test mass containment cage

The static analysis performed use linear solutions, Nastran SOL 101, which is valid within the assumptions of small displacements, such as those of interest for high accuracy applications. The FEM model used for the static analysis by setting an acceleration in a generic direction, can be used to predict the behaviour of the suspension and therefore build an acceleration-displacement relationship useful for the calibration of the accelerometer, given that the interferometric system of the LIG-A measures the displacements of the test mass to compute the acceleration of the satellite.

4 MULTIPLE SHEETS ELASTIC SUSPENSION

4.1 Concept

The starting idea for the concept of a multiple sheets elastic suspension is that of having a test mass suspended by a series of parallel metal sheets, bound together by riveting at the vertices, two by two in an alternating way, as shown below. Each plate acts with diagonal bending.

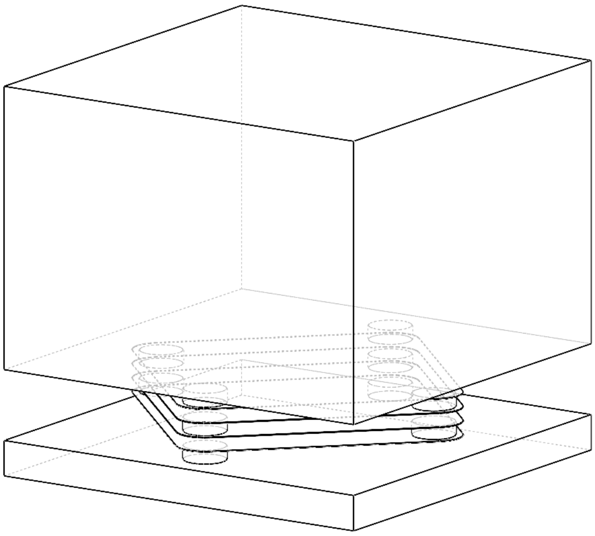

Fig. 4.1: Concept of an elastic suspension system with metal sheets, with test mass and base support

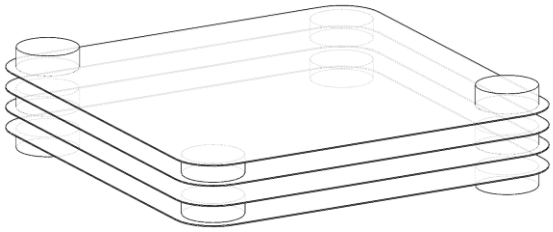

Fig. 4.2: Detail of the elastic suspension only, in this case with four metal sheets

Fig. 4.3: Multiple sheets elastic suspension concept, front and side rendering view

A contraption of this type provides all 6 spatial degrees of freedom for the test mass. The choice of a suspension of this kind is justified by the great overall flexibility and, on the other hand, by a great torsion stiffness. However it requires the assembly of several parts together, which can be critical for space applications where a very high degree of precision is desirable.

Especially interesting for our application as a spring-mass system of an accelerometer, are the first two resonance modes (one in an orthogonal plane relative to the other) which are those that activate the diagonal bending mode of the plates. The third resonance mode, in order of increasing frequency of an elastic system of this type, is the longitudinal one of elongation and compression. It can be of interest both if we want to make a measurement on all three axes with the accelerometer and to absorb the oscillations during the launch stages of the space mission.

The first three resonance modes for a suspension of this type are shown below, thus the two bending and the longitudinal one. The colour gradient in the figures represents the eigenvalue related to the displacements in the solution of the modal analysis.

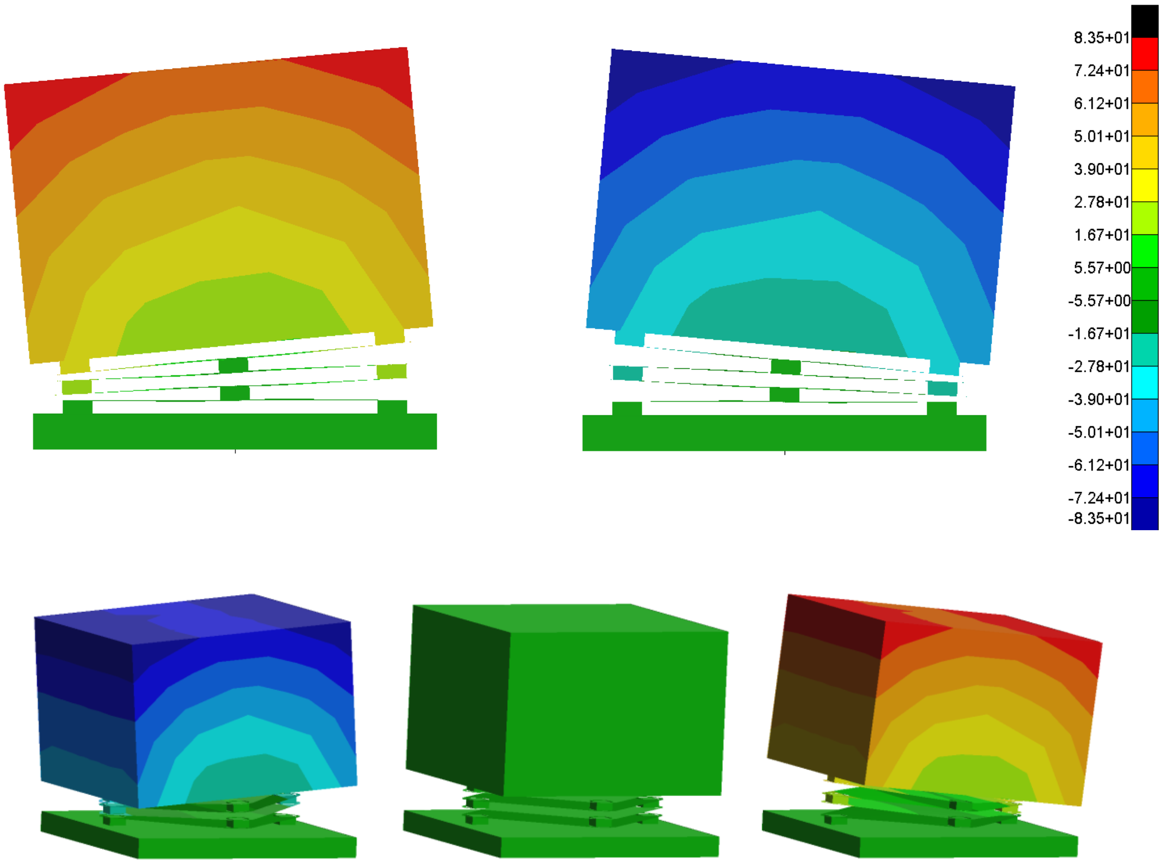

Fig. 4.4: First bending mode of oscillation for a multiple sheets elastic suspension, displacement plot

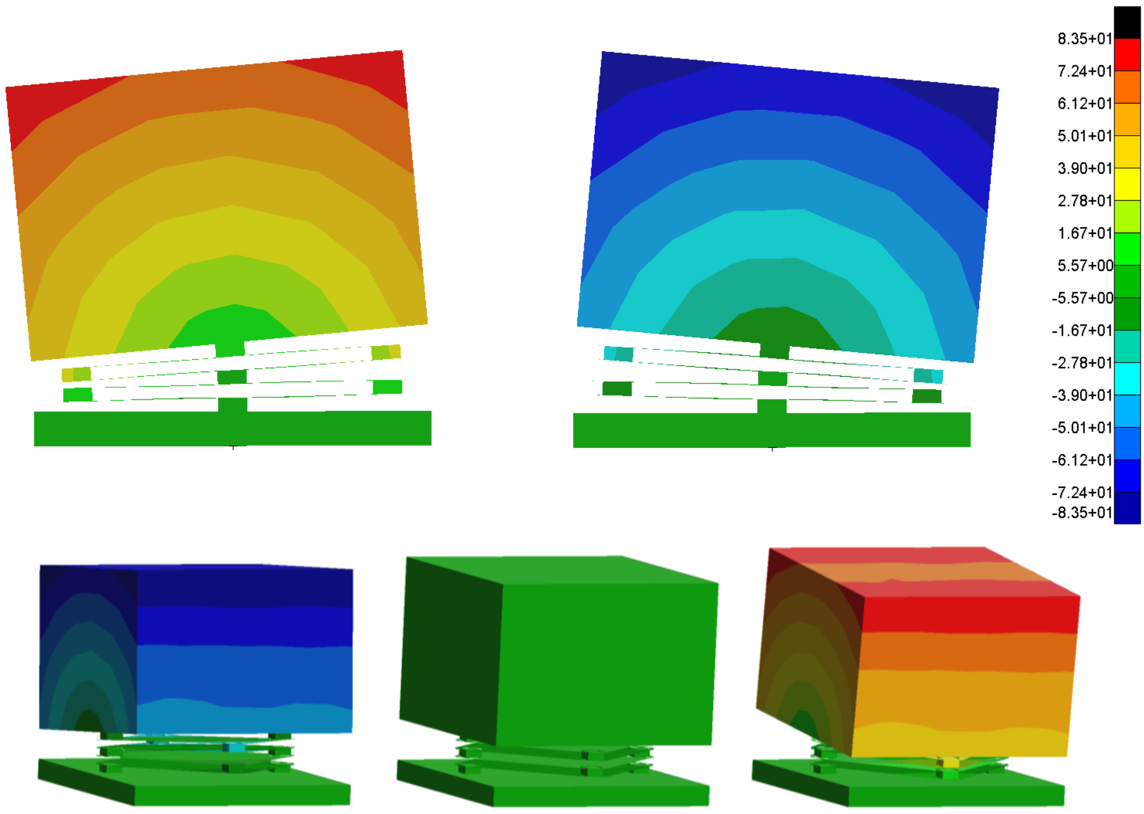

Fig. 4.5: Second bending mode of oscillation for a multiple sheets elastic suspension, displacement plot

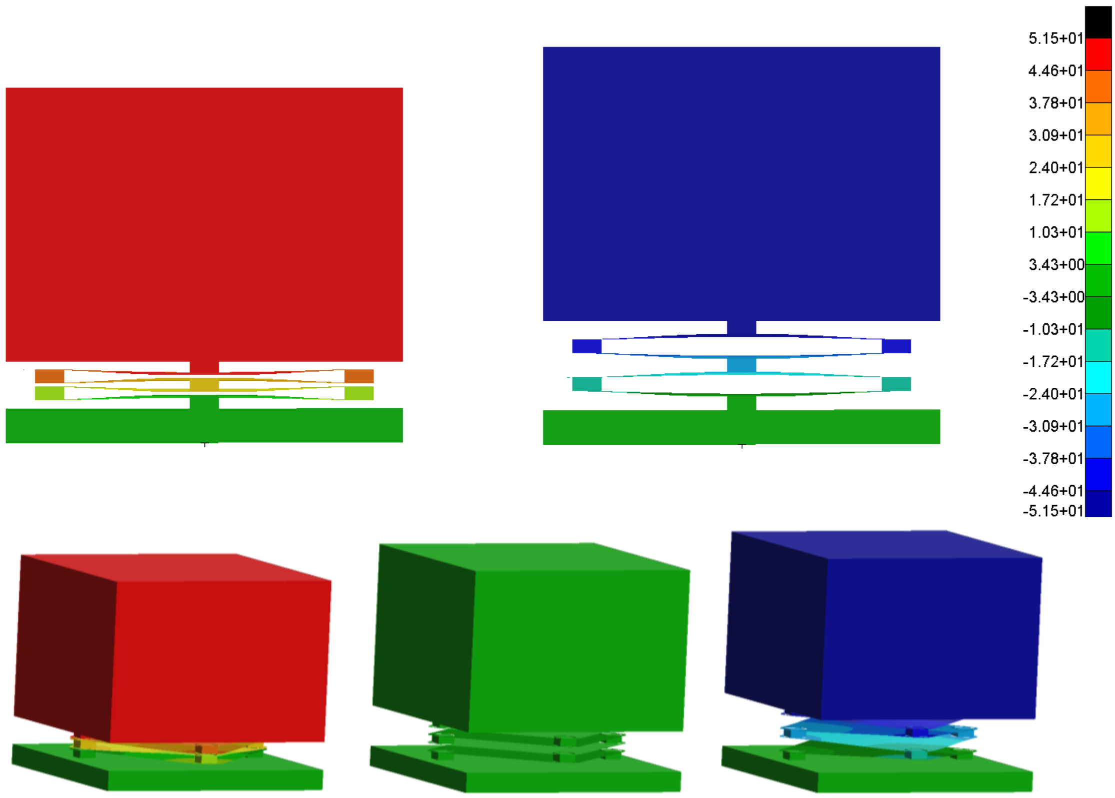

Fig. 4.6: First elongation mode of oscillation of a multiple sheets elastic suspension, displacement plot

4.2 FEM Preliminary Study: Plate-A Model

For a preliminary FEM study of the diagonal bending behaviour of the single plate of the elastic suspension, I draw a CAD that resemble the geometry of that of a preliminary prototype, made at INRiM labs from a spring steel sheet of 0.1 mm of thickness. The geometry of the model in question will be called as “Plate-A”.

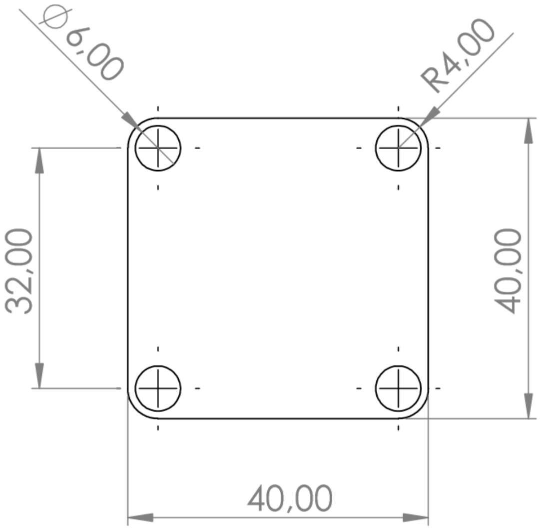

Fig. 4.7: Dimensioned CAD of a single sheet, model Plate-A. Thickness: 0.1 mm

4.2.1 Plate-A Model: Static

It is required to study the diagonal bending behaviour, which is obtained with two diagonally opposite vertices being interlocked and the other two subjected to two forces that generate a bending torque. For small displacements and for the purposes of this preliminary analysis, the system can be modelled with a lumped parameter analogy, with a torsional spring, of stiffness k_t, at the joints (diagonal cut view) that is subjected to a torque given by the two forces at the other two vertices, as represented below.

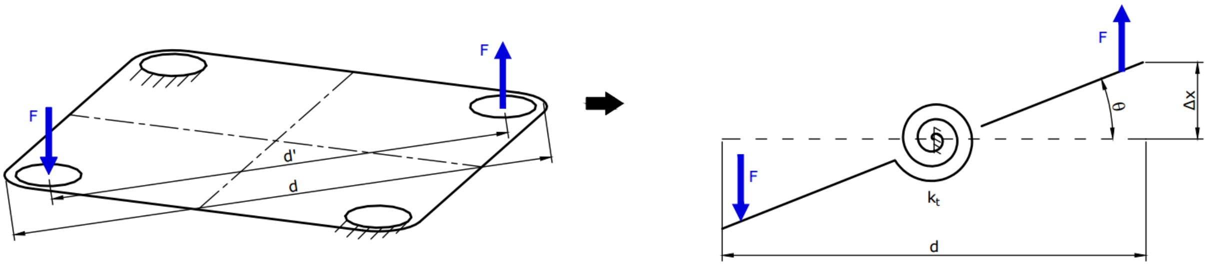

Fig. 4.8: Simplified model made to define the diagonal bending stiffness of the plate

The elastic coefficient k_t is obtained from the lateral displacement Δx as follows:

$$k_t = \frac{Fd'}{\vartheta}$$

For small displacements we can simplify:

$$\vartheta \cong \left(\frac{\Delta x}{d/2}\right) [rad]$$

In general, given the maximum displacement from the FEM analysis, it is valid the geometric relation:

$$\vartheta = 2\, sin^{-1}\left(\frac{max\ displacement}{d}\right)$$

Referring to the CAD and to the FEM analysis, we have that:

- Δx is the maximum displacement obtained from the FEM solution.

- *d* is the maximum diagonal dimension of the plate, corresponding to the maximum displacement position.

  $$d = 53.255\ mm$$

- *d’* is the distance between the two holes in place of the rivets, thus the force application points.

  $$d' = 32 \cdot \sqrt{2}\ mm$$

The *Patran – Nastran* software is used to perform static analyses (SOL 101) of the bending behaviour of the sheet, in the linear and non-linear fields, using a meshing with *Tria* two-dimensional triangular elements, *Hybrid* mesher, with a *Global Edge Length* of 2 mm. The material is modelled as homogeneous and isotropic. Considering that the sheet of the prototype is made from a generic spring steel, the following properties are assigned [14][15]:

Elastic Modulus: E = 206000 [MPa]
Poisson’s Ratio: $\nu = 0.3$
Density: $\rho = 7.85\text{e-}9$ [Ton/mm^3]

It is useful to remind that the *Patran - Nastran* software infers without measurement units, therefore we need to be careful in choosing and respect the selected system:

$$mm - N - MPa - Ton$$

Different analyses are reiterated with a linear static solution (Nastran code SOL 101) and a non-linear static solution (Nastran code SOL 106), thus the maximum displacement values is obtained from which the bending stiffness is derived, for a range of forces in any case low, according to our interests, to verify that consistent results are obtained.

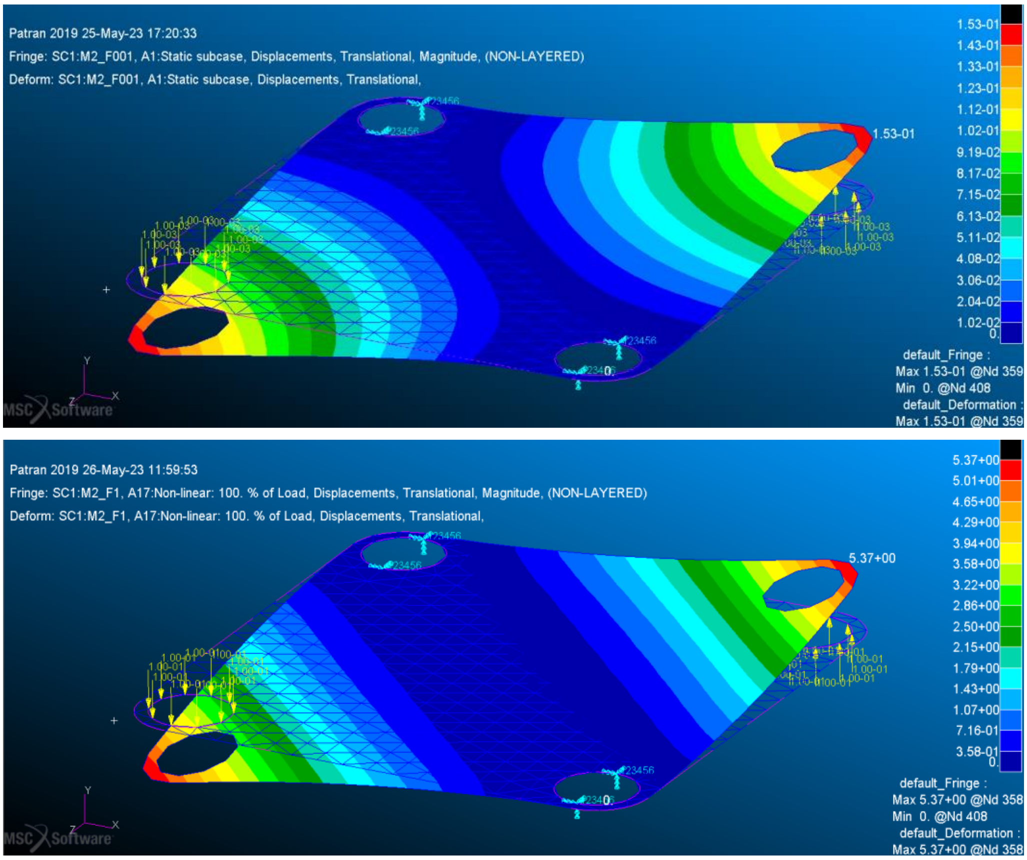

Fig. 4.9: Large displacements phenomena: comparison between the displacement plot from a linear analysis with torque forces of 0.01 N (above) and that from non-linear analysis for torque forces of 1N (below) for the Plate-A, mesh with GEL of 2 mm

		Nastran SOL 101		**Nastran SOL 106**	
		max displ.	**k_t**	**max displ.**	**k_t**
F [N]	**Torque [Nmm]**	**[mm]**	**[Nmm/deg]**	**[mm]**	**[Nmm/deg]**
0.001	4.53E-02	1.53E-02	**1.37**	1.53E-02	**1.37**
0.002	9.05E-02	3.06E-02	**1.37**	3.06E-02	**1.37**
0.005	2.26E-01	7.66E-02	**1.37**	7.59E-02	**1.39**
0.010	4.53E-01	1.53E-01	**1.37**	1.48E-01	**1.42**

0.020	9.05E-01	3.06E-01	**1.37**	2.75E-01	**1.53**
0.050	2.26E+00	7.66E-01	**1.37**	5.50E-02	**1.91**
0.100	4.53E+00	1.53E+00	**1.37**	8.69E-01	**2.42**
0.500	2.26E+01	7.66E-00	**1.37**	2.94E+00	**3.57**
1.000	45.3E+01	1.53E+01	**1.37**	5.37E+00	**3.91**
2.000	9.05E+01	3.06E+01	**1.37**	9.42E+00	**4.44**

Tab. 4.1: Diagonal bending stiffness results with FEM analysis for Plate-A model, *Tria* mesh elements with 2 mm *GEL*

It is deduced from the results that, as naturally expected, the linear analysis always provides the same bending stiffness value while the non-linear analysis provides values close to the linear ones only for tests with torques smaller than about 0.5 1 Nmm/deg, while it diverges a lot for larger loads. The trend of this divergence between linear and non-linear results is reported below, as function of the torque.

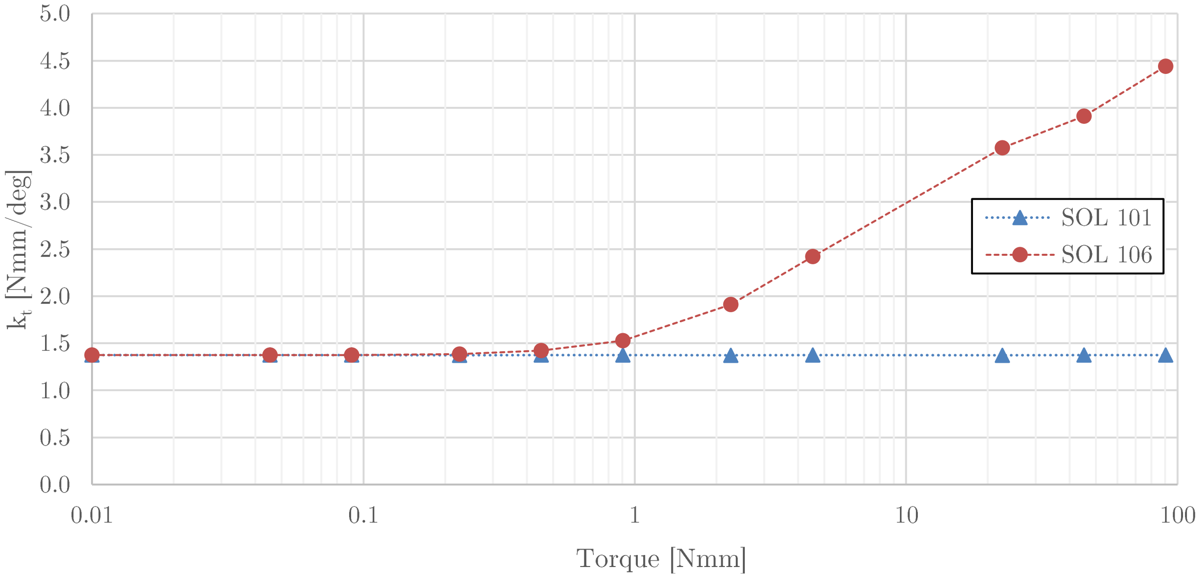

Fig. 4.10: Comparison of bending stiffness results between linear and non-linear solutions as function of the torque, plotted in a logarithmic scale

This non-constant trend of the non-linear results is due to *large displacements phenomena* coming into play for greater loads. In fact, as can be deducted from the comparison of the deformation between small and large displacements cases in Fig. 4.9 on page 60, it can be observed that there is a difference in the topology of the deformation: for small displacements the plate tends to deform radially with respect to the force application points, while for large displacements the displacement is parallel to the diagonal of the plate. Since we are interested in an application where small forces come into play, we should not be interested in these non-linear effects. It will be evaluated in the following chapters if the loads of our interest fall within the range of overlap or divergence between the linear and non-linear solutions.

4.2.2 Plate-A: Mesh Convergence Analysis

With the intent to obtain more realistic values, the mesh could be made thicker at the price of a higher computational cost for each single analysis. To optimize the process, a convergence study can be carried out to find the maximum value of *Global Edge Length* (GEL) of the elements, for example of the *Tria* type, to guarantee results with sufficiently accurate values. Furthermore, this study is important to find a relationship between error and mesh refinement, so as to know in advance how much a result obtained from less refined mesh, for example in a more sophisticated model for saving on computational cost, will deviate from reality. I will start by carrying out the convergence analysis only for linear resolution, therefore Nastran SOL 101, since it should be the field of our interest, furthermore because we already established that the percentage error due to the refinement of the mesh does not depend on the type of solution. In order to obtain consistent results, I choose to evaluate a static case in which the linear solution is superimposable on the non-linear one, therefore for the applied load of 2.00E-03 N which corresponds to a torque of 9.05E-02 Nmm previously seen on Tab. 4.1 on page 61.

The linear SOL 101 analyses are reiterated for the same model with the same load conditions as the mesh refinement varies, starting from the automatic one calculated by the software, i.e. with GEL = 5.153 mm.

Convergence analysis, 2D Mesh - Tria:

1. Element shape: Tria (triangular)
2. Mesher: Hybrid
3. Topology: Tria3

Tria Mesh	**Nastran SOL 101**					
GEL [mm]	**F [N]**	**max. displ. [mm]**	**k_t [Nmm/deg]**	**Run Time [s]**	**N. of nodes**	**Error %**
5.153	0.002	3.08E-02	**1.37**	4.97	122	0.00
4	0.002	3.09E-02	**1.36**	4.64	160	0.324
3	0.002	3.10E-02	**1.36**	5.14	212	0.645
2	0.002	3.06E-02	**1.37**	4.13	437	0.654
1	0.002	3.08E-02	**1.36**	7.09	1583	Ref.

Tab. 4.2: Bending stiffness results as function of the mesh refinement

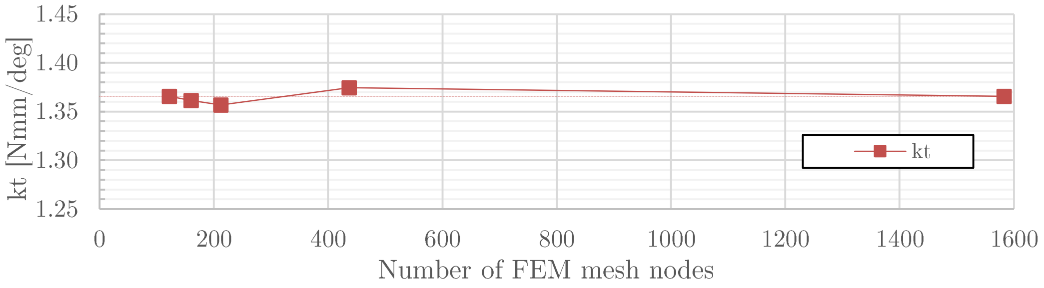

Fig. 4.11: Variation of bending stiffness FEM results with the number of mesh nodes, for the Plate-A model

The same static stiffness value is obtained regardless of the refinement of the mesh, thus we can say that convergence of the results is already obtained and the small oscillations of the values (less than 1%) are probably due to the different shape of the elements. A mean bending stiffness value equal to 1.36±0.01 Nmm/deg is obtained.

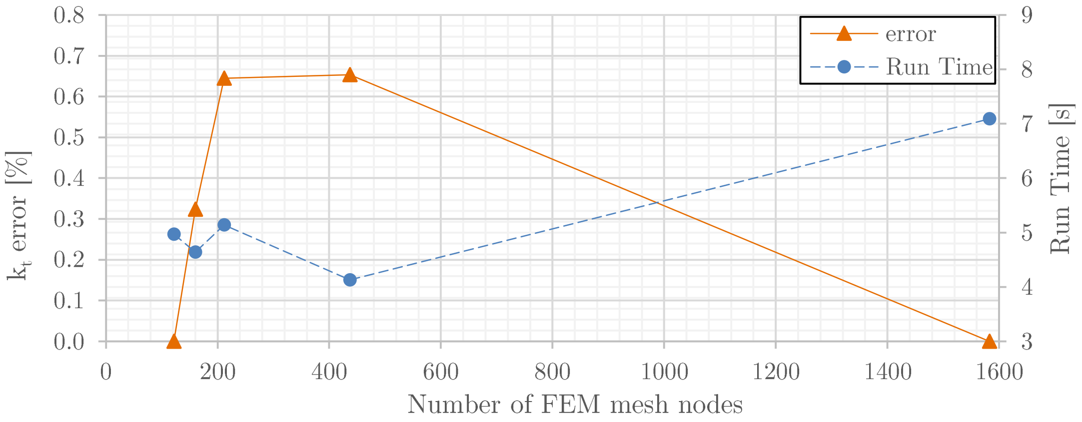

Fig. 4.12: Trend of the error and analysis run time of the FEM results with the number of mesh nodes for the Plate-A model

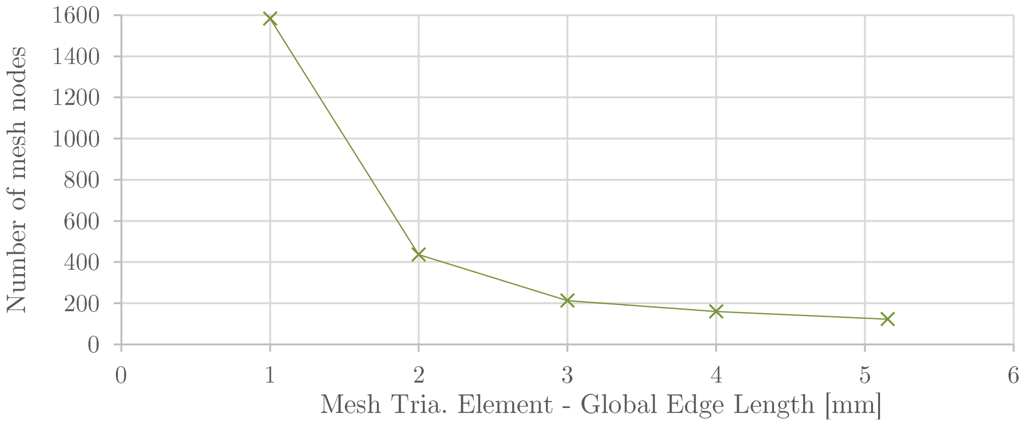

Fig. 4.13: Number of mesh nodes as a function of the average size of the triangular mesh element

The run time is displayed in the “.log” file generated by the Nastran run. It can be observed that the number of nodes increases asymptotically as the size of the mesh elements, thus the GEL parameter, decreases (Fig. 4.13). In fact if we theoretically had an element of zero dimension, the number of nodes would be infinite.

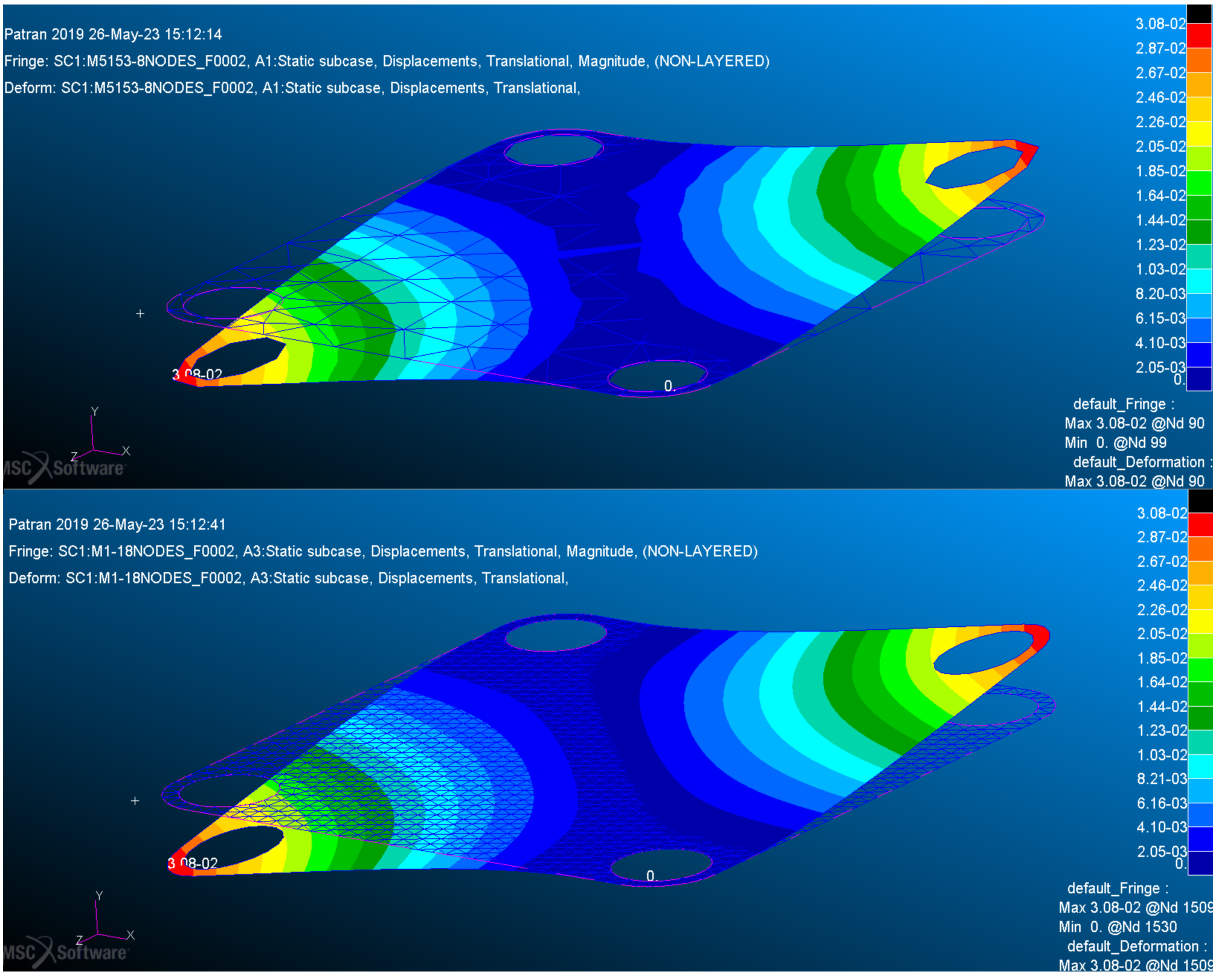

Fig. 4.14: Comparison of two convergence analysis results, between a rough (122 nodes) and a more refined (1583 nodes) mesh

From the picture above it can be observed that the same displacement value is obtained between a less and a more refined mesh, at the only cost of the resolution of the results display. We can therefore comfortably choose to use the rougher mesh, i.e. the one automatically set with GEL of 5.153 mm, in case we want to build a more complex model with several assembled plates, to save on the number of total nodes.

Using a mesh with *Quad* (quadrangular) type elements we obtain the same results as the previous case and an equal number of nodes as the average size of the element varies, but a more irregular shape of the grid than that of the mesh with triangular elements. So in this case we prefer to use *Tria* elements.

4.3 Experimental and FEM Comparison – Bending Mode

First of all we want to verify that the FEM analysis results are reliable for our purposes, thus we prepare an experimental setup where we can make high accuracy measurements for the diagonal bending behaviour, which represents the first oscillation mode of the system of our interest.

For each experimental test there will be a FEM counterpart with modelling and analysis using the *MSC Patran – Nastran* software. From the comparison between computational and experimental results it is possible to calibrate some parameters of the model.

The *Precitec CHRocodile 2 S* instrument was chosen to conduct the measurements, which exploits the confocal chromatic technology of an optical sensor. A polychromatic light source hits the surface whose distance is to be known, the optical lens will be such as to ensure that for each wavelength there will be a different focal length. Only a certain wavelength will be therefore focused and once established which, the distance can be obtained.

This technology allows very robust measurements, for any type of material and at angles up to 45°. For the optical sensor used, a resolution of up to 2 nm and a range of 100 µm can be obtained. The *CHRocodile 2 S* unit allows a signal acquisition frequency up to 4000 Hz, which will be useful in the measurements of the frequencies of the resonance modes [16].

Fig. 4.15: Distance measurement determination unit *Precitec – CHRocodile 2 S*

From the picture above in Fig. 4.15 it can be observed that the spectrum graph has a peak of reflected light at a certain wavelength from which the distance "D1" from the optical sensor lenses is obtained.

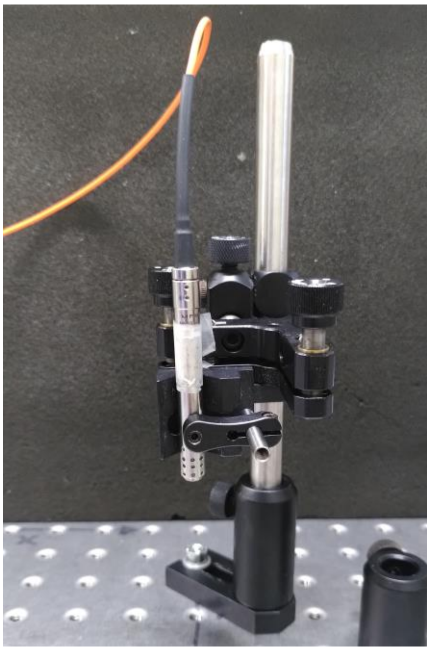

Fig. 4.16: Support stand and optical sensor 5002430

The optical sensor is properly supported so that the angle and distance of the sensor from the surface to be measured can be adjusted with precision screws, so as to fall within the 100 µm range where measurement is possible. This range is placed at a distance of about 1.4 mm from the sensor lenses [16].

The measurement chain therefore starts from the optical sensor which is connected to the *CHRocodile 2 S* unit via optical fiber, the unit in return transmits the digital data to a computer (my personal laptop) via Ethernet, where the data can be processed through a dedicated software.

4.3.1 Free Resonance Vibration of the Single Sheet

Empirical measurement trials

We begin with a preliminary analysis with the measurement of the free plate vibrations, only constrained at two vertices, as shown below.

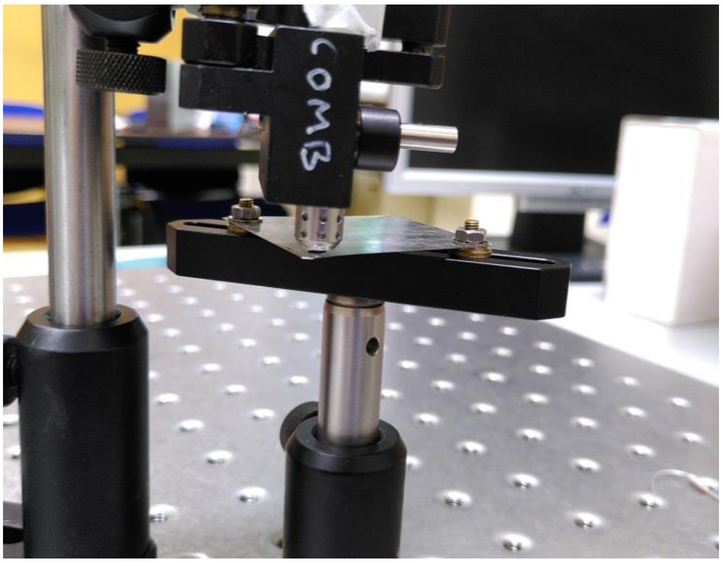

Fig. 4.17: Resonance frequency measurement of the free metal plate

The plate is a square of 40 mm of side length, with four 3 mm diameter holes at the vertices and fitted with 7 mm diameter washers and has a thickness of 0.1 mm. A vibration is induced through a stimulation and the plate is allowed to vibrate freely. The acquisition is here reported:

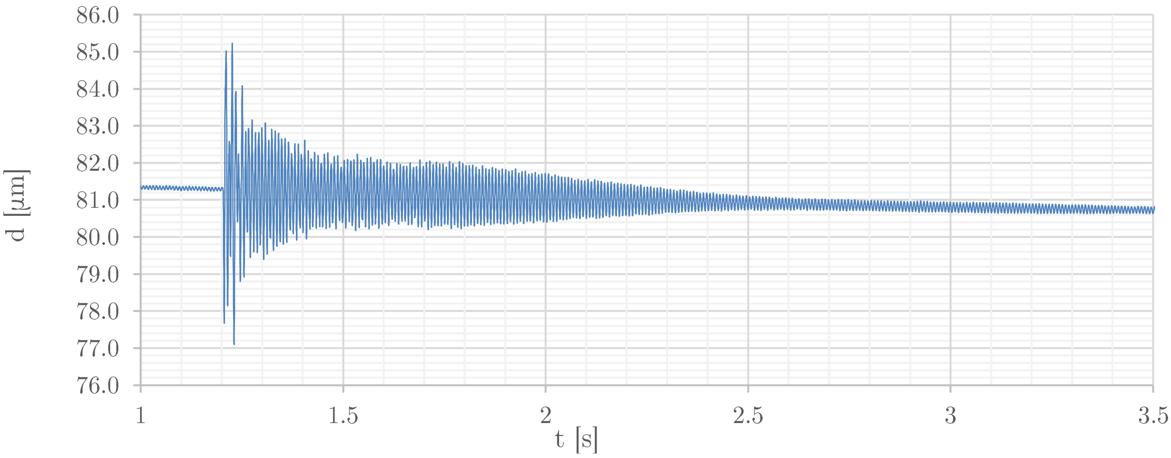

Fig. 4.18: Acquisition data of the free vibration of the plate, clamped at two diagonal vertexes

The oscillations tend to dampen over time and the higher frequency modes dampen first, so we choose to analyse a detail in the trail of the damping, so that the first mode of oscillation is prevailing.

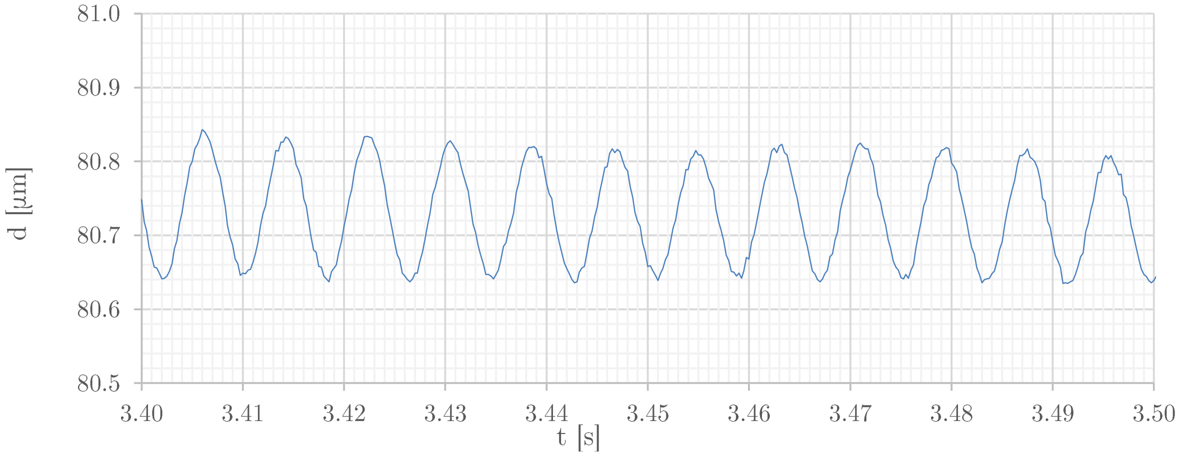

Fig. 4.19: Detail of the acquisition of the free vibration of the plate with a frequency equal to that of the first bending resonance mode, if the plate is clamped at the two diagonal vertices

In the above pictured frame there are 10 periods of oscillation in 0.0815 seconds, resulting in a frequency of 122.7 Hz. This frequency estimate is repeated for two other different segments of the acquisition and we obtain:

Acquisition segment [s]	**Frequency [Hz]**
1.593-1.511	123.077
3.487-3.406	122.699
6.094-6.004	122.222
Mean:	**122.667**

Tab. 4.3: Empirical result of the first resonance mode of the free oscillating plate

FEM Modal Analysis

After creating a CAD model of the plate in question, as similar to the real piece as possible, the geometry is imported into the *Patran* database and the properties of a generic spring steel are assigned [14][15]:

Elastic Modulus: $E = 206000$ [MPa]
Poisson's Ratio: $\nu = 0.3$
Density: $\rho = 7.85\text{e-}9$ [Ton/mm^3]

Having set the clamps constraints in correspondence with the washers, the modal analysis is carried out, Nastran code SOL 103. With a plate thickness of 0.10 mm, according to a micrometre evaluation, a frequency of the first resonance mode of 138 Hz is obtained, different from the measured one of 122 Hz. By adjusting the parameters of the material within the limits of the possible values for steels, a value smaller than 130 Hz cannot be obtained. If a thickness of 0.09 mm is set, a frequency of 124 Hz is obtained, closer to the measured value.

	Nastran SOL 103	Empirical result
Plate Thickness [mm]	**1st resonance frequency [Hz]**	**1st resonance frequency [Hz]**
0.10	138.18	**122.67**
0.09	124.36	

Tab. 4.4: Comparison of FEM and experimental results for the first resonance frequency of the free diagonal bending mode oscillation of the plate

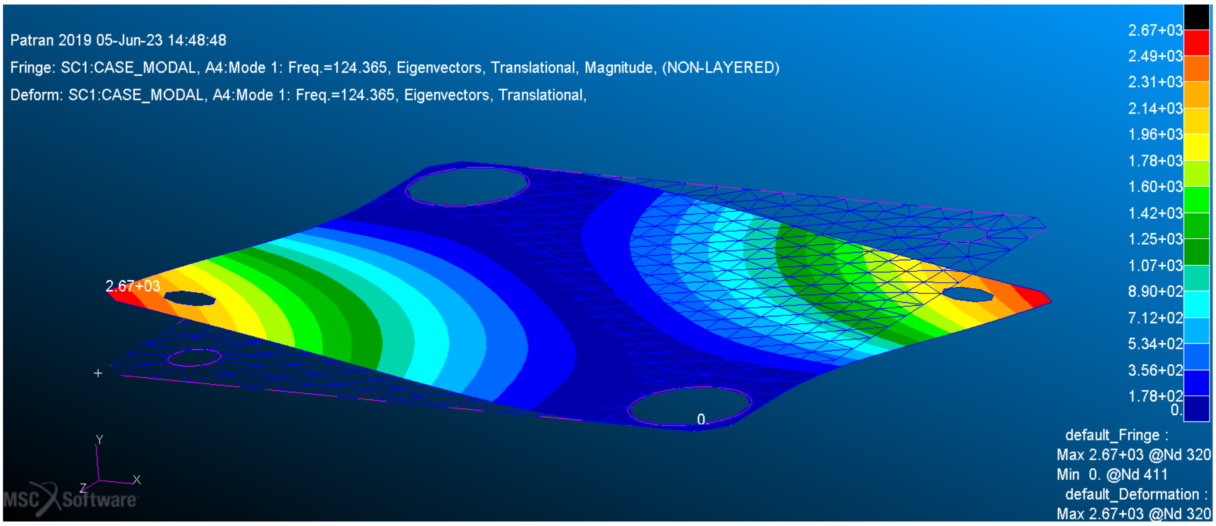
Patran 2019 05-Jun-23 14:48:48
Fringe: SC1:CASE_MODAL, A4:Mode 1: Freq.=124.365, Eigenvectors, Translational, Magnitude, (NON-LAYERED)
Deform: SC1:CASE_MODAL, A4:Mode 1: Freq.=124.365, Eigenvectors, Translational,

default_Fringe :
Max 2.67+03 @Nd 320
Min 0. @Nd 411
default_Deformation :
Max 2.67+03 @Nd 320

Fig. 4.20: FEM model and result for the modal analysis, plate with thickness of 0.09 mm

The assumed error for the micrometric measurement of the thickness to bring the results closer is at the limit of plausibility, meaning that the difference in the results may be due to the limits of the FEM calculation. In fact, the modal analysis is mass dependent and since the plate is free without any tied test mass (and with a tiny inherent mass), the result will be more sensitive to errors relative to the real model. By adding a test mass to the system we will see that the FEM results will coincide with the experimental ones, this can be also recognized with a static analysis as following.

4.3.2 Static Response of the Plate

The next experimental campaign to perform has the goal of measuring the stiffness of the single plate (model Plate-A, see Fig. 4.7 on page 58, but clamped with 7 mm diameter washers instead) subjected to diagonal bending. We therefore want to recreate the load conditions of the single plate of the aforementioned multiple sheets elastic suspension.

Two opposite diagonal vertexes of the plate are clamped to a fixed support, the other two are rigidly bound together by a small beam made from a carbon fiber laminate. At the centre of the beam there is a bolting which acts as a support to the masses to be applied, so as to generate a torque acting in the bending mode. The optical sensor is placed in such a way as to measure the displacement of the beam as a function of the applied load, as shown below:

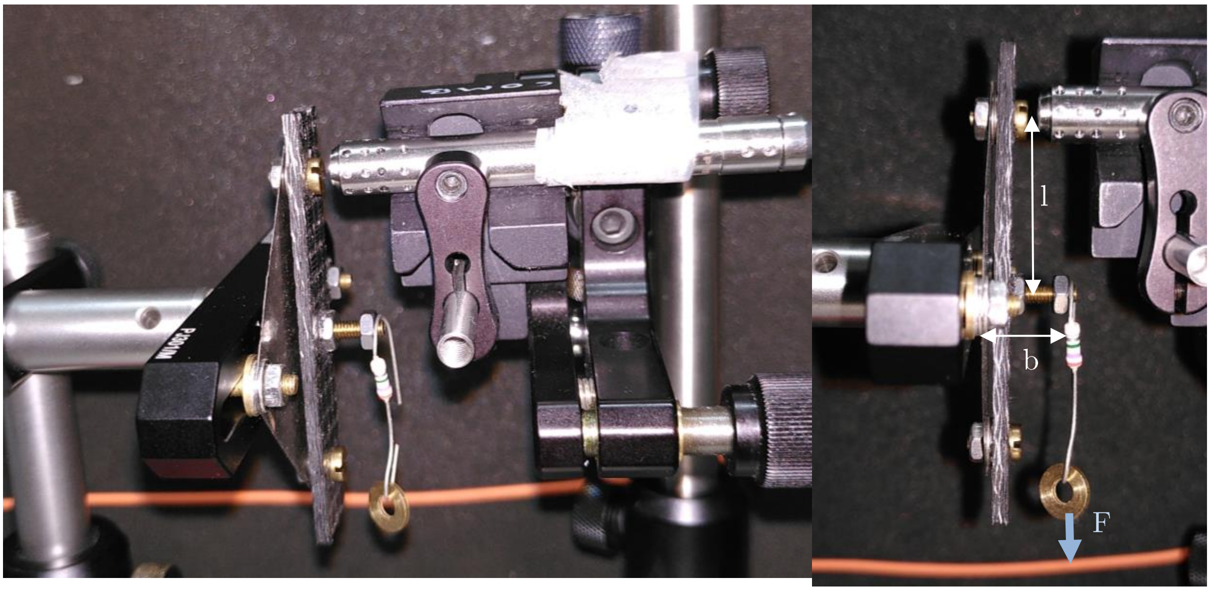

Fig. 4.21: Experimental measurement setup of the diagonal bending stiffness of the plate

This setup is the equivalent of simulating the static response of the elastic suspension made from a single metal sheet, with a certain test mass and a certain lateral acceleration acting upon it. If the stiffness were known, once the displacement was measured, the acceleration can be derived: this is therefore basically a simplified model of the accelerometer object of the thesis.

The lever arms are measured with a calliper and the proof masses with a precision scale from the INRiM biomedical laboratory from which the applied torque can be derived. Measurements are made for two different proof masses resulting in different loads. Referring to Fig. 4.21 for the lengths, we have.

l:	24.3 mm
b:	11.6 mm
mass 1:	0.492 g
mass 2:	1.05 g

The distance measurements from the optical sensor are then carried out as the load varies: first for a zero load and then for the two masses applied, always with the *CHRocodile 2 S* unit.

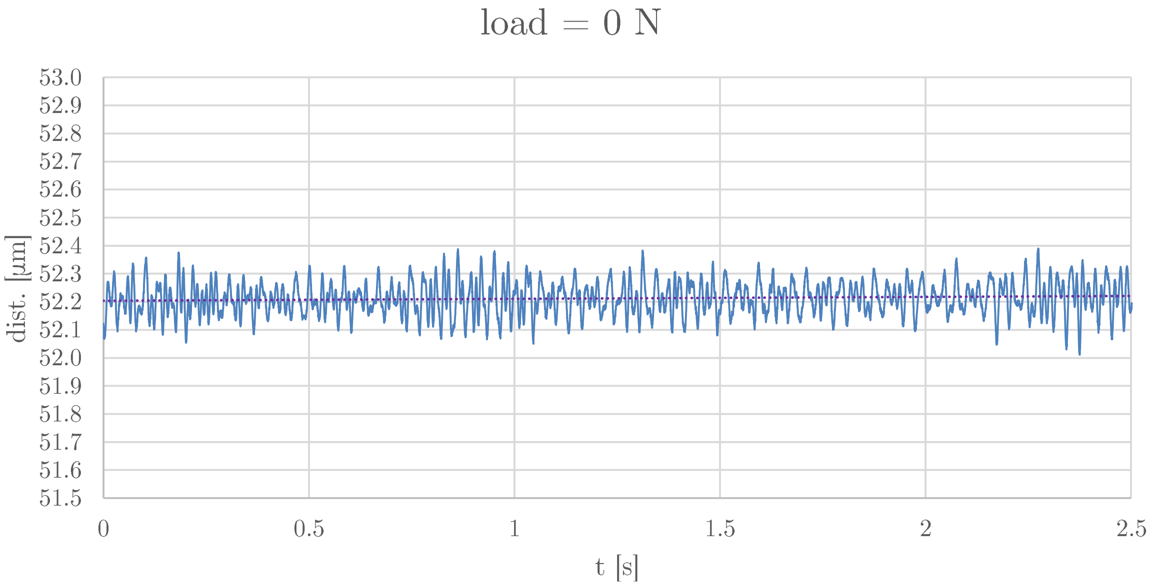

Fig. 4.22: Distance measurement of the carbon beam from the sensor for the unloaded case, reference point: 52.21 µm

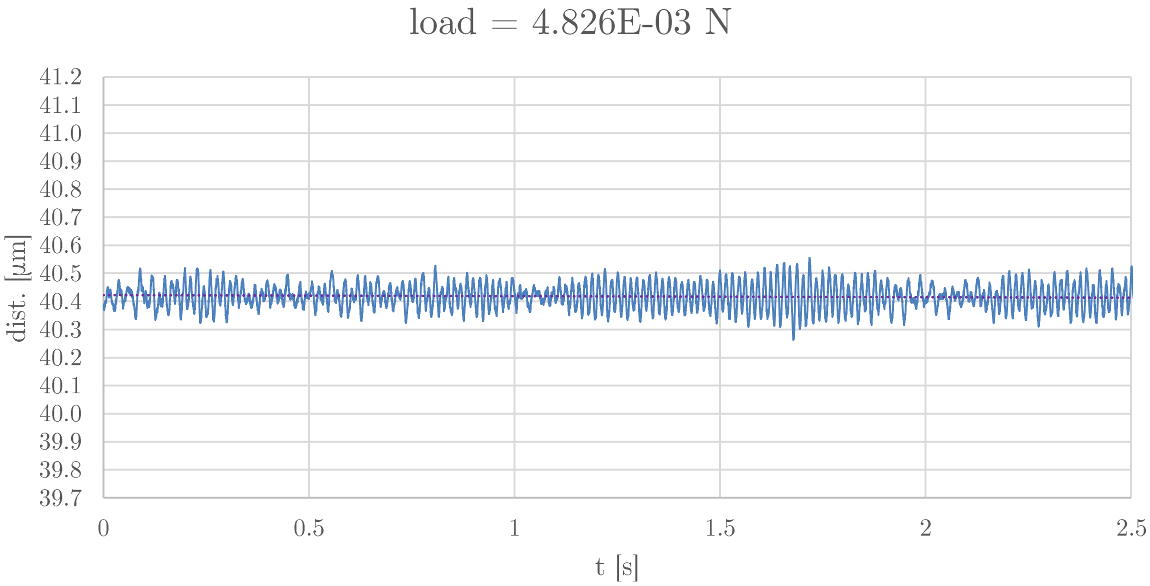

Fig. 4.23: Distance measurement of the carbon beam from the sensor for the first load applied: 40.42 µm

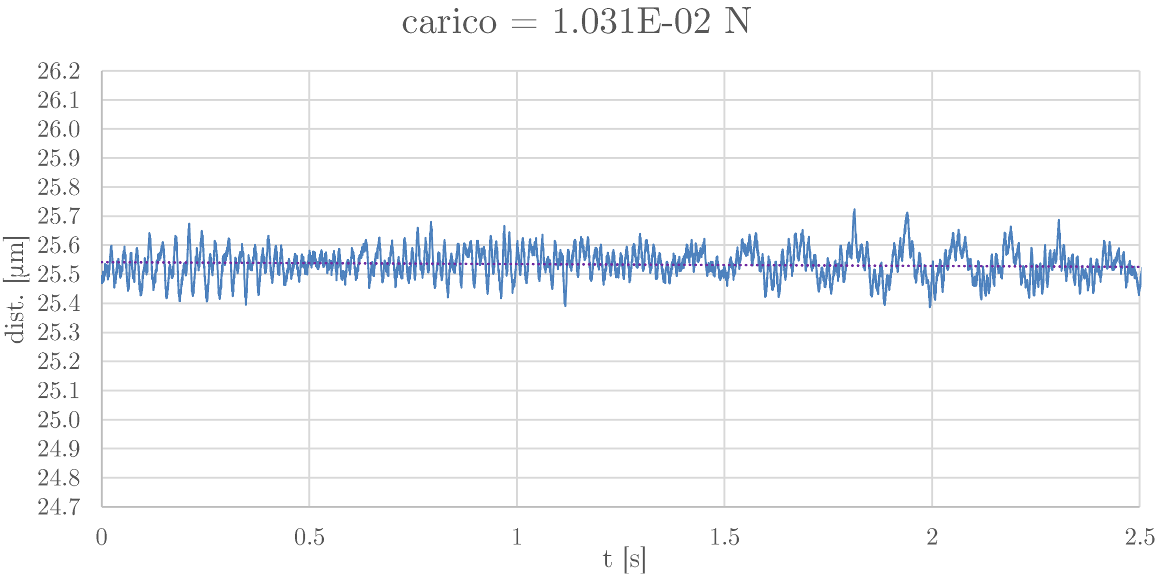

Fig. 4.24: Distance measurement for the second load applied: 25.53 µm

By evaluating the average values from the distance measurements and thus calculating the displacement, the diagonal bending stiffness of the plate can be obtained, referring to a simplified lumped parameter model (see Fig. 4.8 on page 58):

$$k_t = \frac{Fb}{\vartheta}$$

With Δx obtained from the aforementioned measurements, for small displacements:

$$\vartheta \cong \left(\frac{\Delta x}{l}\right) [rad]$$

This measurement is repeated several times, therefore the l and b dimensions would also vary because each time there are small displacements and it is necessary to recalibrate. It is also noted that the reference point changes with each measurement, up to a few micrometres, so the results must be considered with a certain margin of error. The results obtained are reported as follows:

Torque [Nmm]	**Δx [mm]**	**k_t [Nmm/deg]**
5.60E-02	1.18E-02	**2.01**
1.20E-01	2.67E-02	**1.91**
6.05E-02	1.39E-02	**1.80**
1.29E-01	2.68E-02	**2.00**
	Media:	**1.93±0.1**

Tab. 4.5: Empirical results for the diagonal bending stiffness of the plate

The measurement campaign is followed by FEM analysis which aims to simulate the same experimental conditions and then compare the results. The model bases its geometry from the real plate and a thickness of 0.1 mm is imposed, as resulting from micrometre measurements. An *MPC RBE2* constraint is used to simulate the carbon support. The torque is applied with a lever arm b = 11.6 mm and a force equal to 4.826E-03 N, as in the test case using the "mass 1":

Torque [Nmm]	**Δx [mm]**	**k_t [Nmm/deg]**
5.60E-02	1.35E-02	**1.93**

Tab. 4.6: FEM simulation results for the diagonal bending stiffness

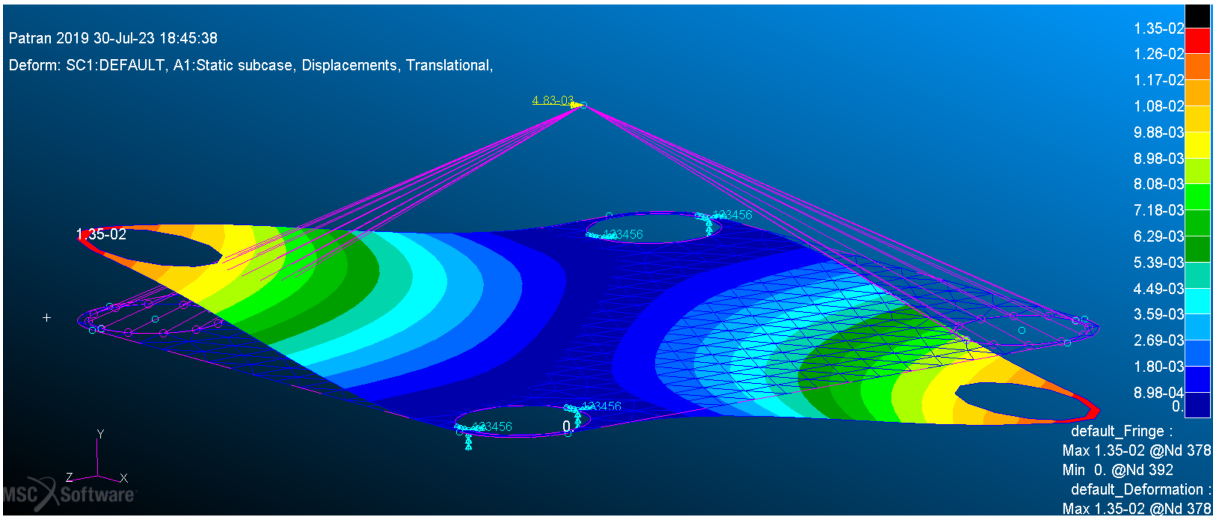

Fig. 4.25: Static FEM analysis, simulating the experimental test, plate loaded with the "mass 1" of 0.492 grams

The comparison between the experimental result and the FEM simulation results in an overlap of the bending stiffness results, confirming the goodness of the FEM results and the reliability of the *finite element method* for modelling the systems described in the following chapters. Furthermore, it can be deduced that the thickness of the plate is actually 0.1 mm as in the FEM solution above, meaning and that the error of the modal analysis of the free plate in the previous paragraph (see Tab. 4.4 on page 69) is not due to an error of thickness measurement, but to the fact that the modal analysis depends on the mass, thus the free vibrations FEM resulted to be more sensitive to errors.

4.4 Influence of Design Parameters on Modal Behaviour

A necessity to study how the different design parameters of a multiple sheets elastic suspension influence the modal behaviour of a mass-spring system emerges, with the goal of understanding the best way to design the suspension thus achieving the desired characteristics within project requirements.

The design parameters for a suspension of this kind that influence the frequency response of the relative mass-spring system could be: the material, the geometry of the elastic sheets, the number of sheets used, the position of the rotation pivot point or the assembly constraints. Different modal analyses will be reiterated as each parameter varies, once the others have been fixed. We choose to always keep the materials and the oscillating mass fixed, using a Beryllium-Copper cubic test mass with a side length of 40 mm, to meet the dimensions required for the accelerometer design.

The Beryllium-Copper alloy C17200 was chosen for both the test mass and the metal sheets of the suspension for its good mechanical characteristics and high electrical and thermal conductivity, desirable for space applications where electrical charges accumulation or thermally isolated areas are better to be avoided.

Electrical Conductivity σ [S/m]	**Thermal Conductivity λ [kcal/hm°C]**	**Density ρ [g/cm^3]**	**Young's Moduls E [GPa]**	**Poisson's Ratio ν**	**Yield Stress σ_y [MPa]**
1.13E+07	115	8.25	130	0.30	965-1205

Tab. 4.7: Mechanical and physical properties of the Beryllium-Copper alloy C17200 [12]

The FEM models that will be used in this stage are simplified, they include only the sheets and the test mass with connections of the parts via *Multi Body Element* of type *RBE2* (see Fig. 4.26). The test mass is modelled with a three-dimensional rough mesh with *Tet10* type elements, while the plates are modelled with a finer two-dimensional mesh composed by triangular elements of the *Tria3* type. The rivets washers interfaces to the plates are modelled as holes, while those attached to the base have translations and rotations of the relative nodes blocked, hence clamped. The connecting rivets are modelled with *Multi Body Element* of type *RBE2* which constrains the mutual rigid motion (magenta in Fig. 4.26).

4.4.1 Sheets Thickness Variation

To study the influence of the variation in thickness of the plates on the modal behaviour of the suspension, a FEM model of the type shown in the figure below is created:

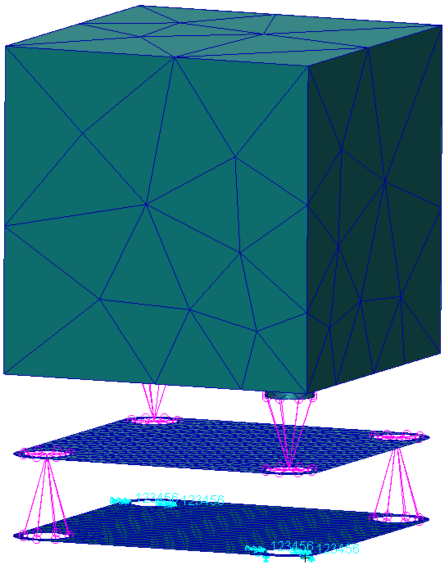

Fig. 4.26: FEM model for the study of the influence of sheets thickness variation on the modal frequencies of the elastic suspension

A two sheets suspension is used. The sheets are of the Plate-A model already used for the preliminary FEM study, which is a simple square plate with a side length of 40 mm, spaced 10 mm in height from each other and from the test mass. The results of the analyses are reported up to the fifth mode because after there is an increase of more than one order of magnitude in the frequency and therefore those higher modes are not influential. Furthermore, the sixth mode is a spurious oscillation of the sheets only and is not the torsion around the axial direction, which would be an undesired mode.

	Nastran SOL 103				
Sheet thickness t [mm]	**F_1 [Hz]** flex_xz	**F_2 [Hz]** flex_xz	**F_3 [Hz]** long_y	**F_4 [Hz]** tors_xz	**F_5 [Hz]** tors_zx
0.05	0.346	0.349	1.178	4.133	6.385
0.07	0.573	0.579	1.951	6.837	10.56
0.10	0.978	0.988	3.329	11.65	18.01
0.15	1.797	1.814	6.113	21.33	32.98

Tab. 4.8: FEM modal analysis results (Nastran SOL 103) of a sheets elastic suspension as the thickness of the plates varies

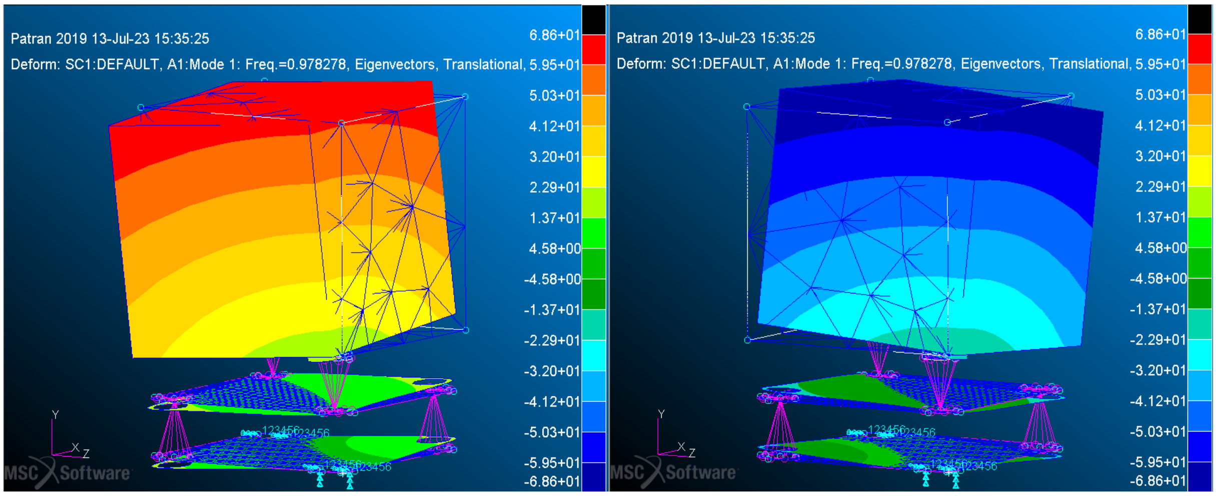

Fig. 4.27: F_1=0.978 Hz (FEM); First bending resonance mode, sheet thickness t=0.1 mm

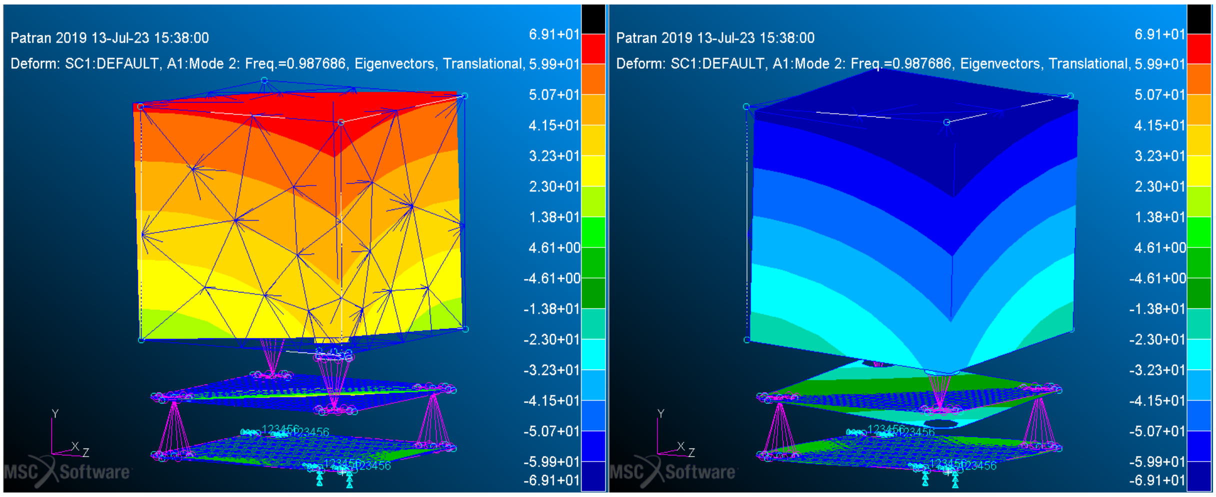

Fig. 4.28: F_2=0.988 Hz (FEM); Second bending resonance mode, sheet thickness t=0.1 mm

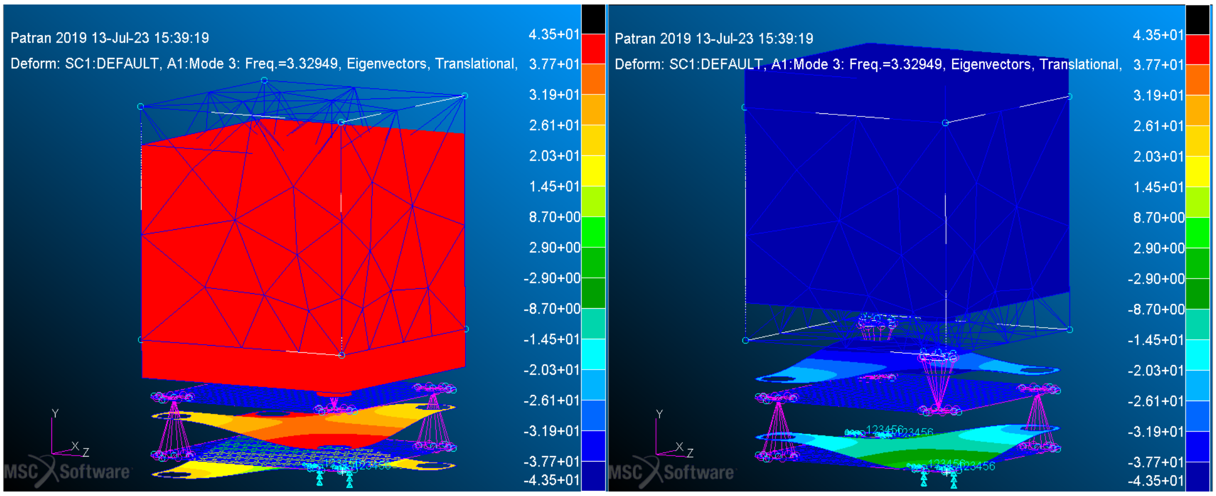

Fig. 4.29: F_3=3.33 Hz (FEM); First longitudinal resonance mode, sheet thickness t=0.1 mm

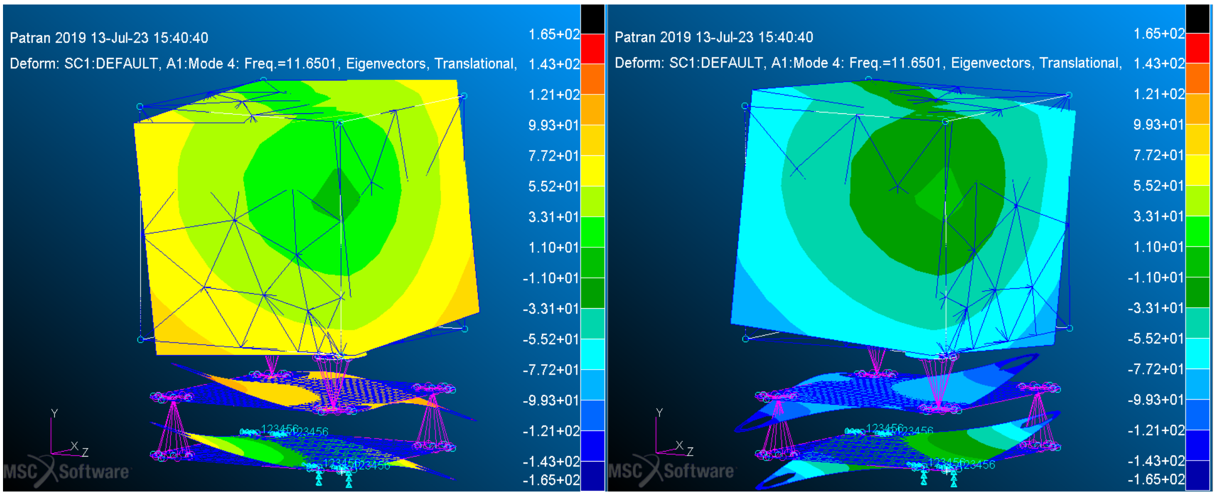

Fig. 4.30: F$_4$=11.7 Hz (FEM); First torsional resonance mode, sheet thickness t=0.1 mm

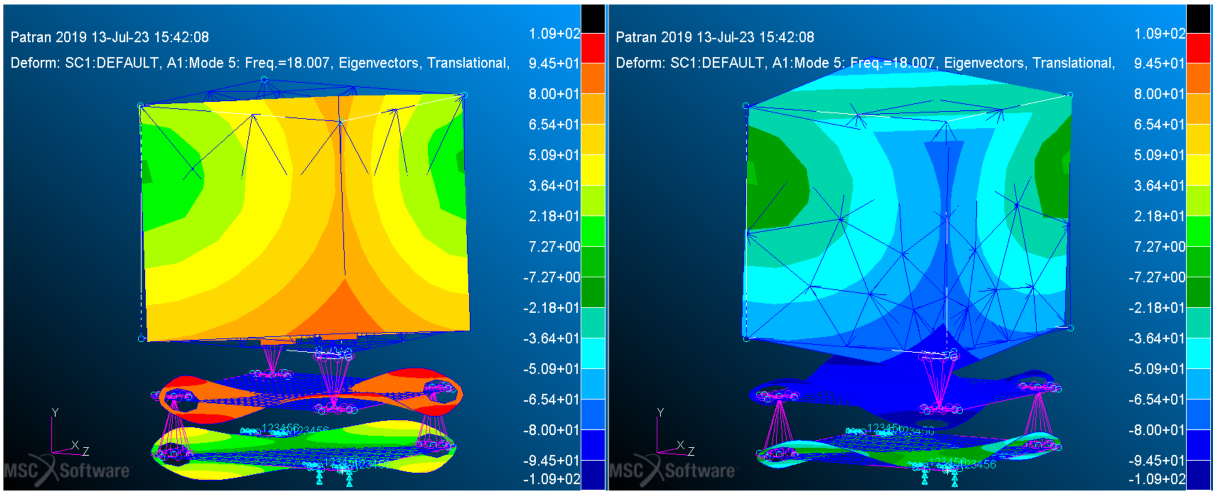

Fig. 4.31: F$_5$=18.0 Hz (FEM); Second torsional resonance mode, sheet thickness t=0.1 mm

Graphs of the sheet thickness – resonance frequencies relation are reported below.

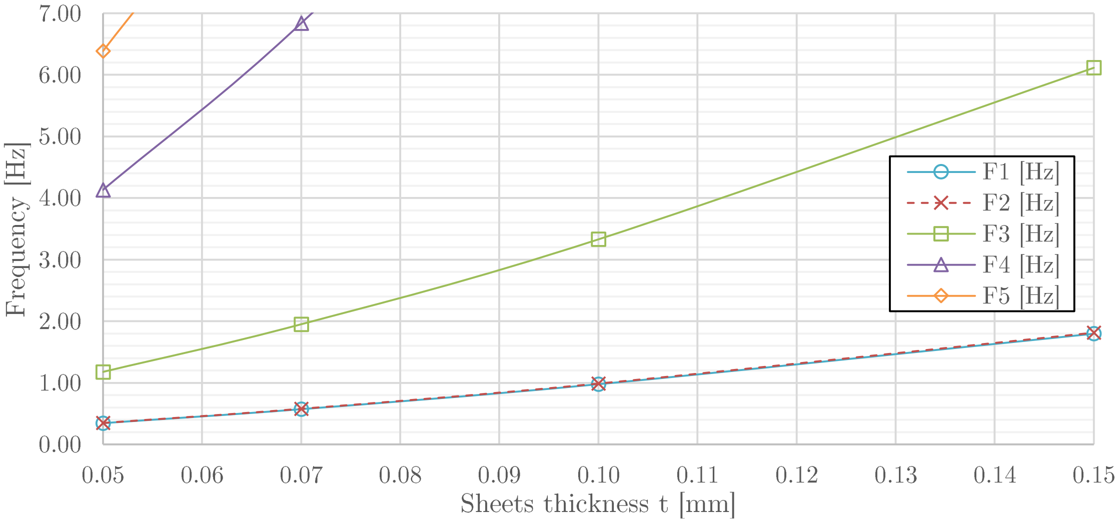

Fig. 4.32: Sheets thickness influence on the modal frequencies of the elastic suspension

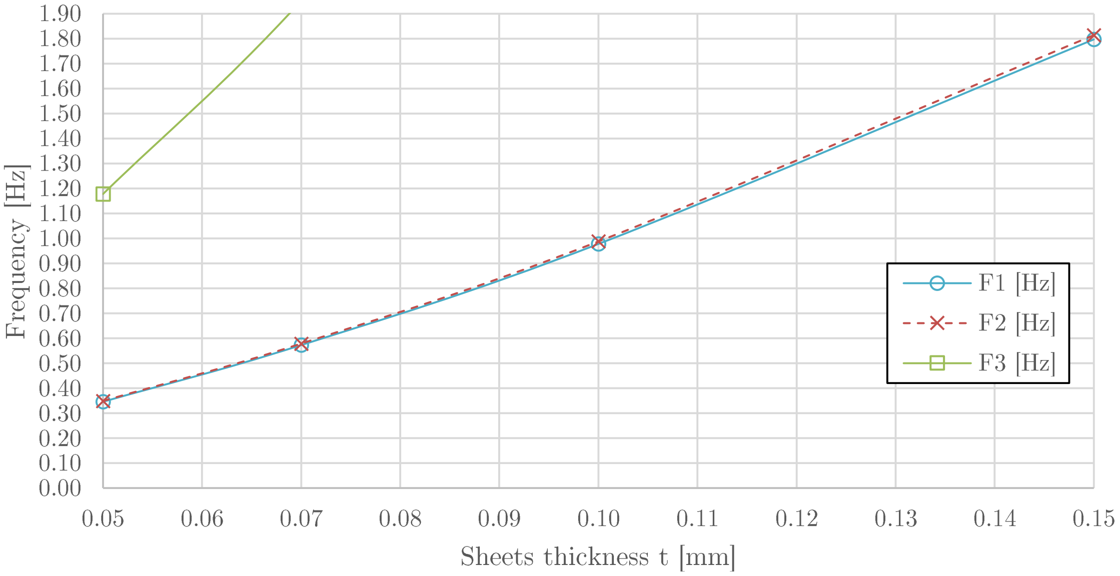

Fig. 4.33: Detail on the first resonance modes of the thickness influence graph

It is found that the suspension becomes softer as the thickness decreases and vice versa, the frequency of the modes increases as the thickness increases, more than proportionally. The results now obtained for the simple full plate will be the reference ones when evaluating the influence of the shape of the plate, cutting a central hole or from the edges.

4.4.2 Sheets Shape Variation: Central Hole

In this stage, starting from the previous model and fixing the thickness value at 0.1 mm, the shape of the plate is changed, removing material with a central hole. The reference frequencies are therefore those in Tab. 4.8 on page 75 of the ordinary plate.

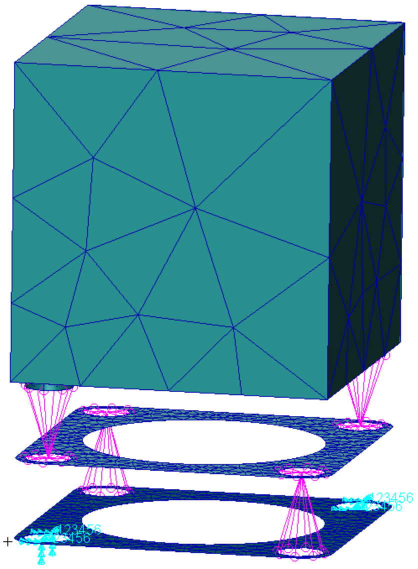

Fig. 4.34: FEM model for the study of the influence of plate shape variation, 30 mm diameter hole

In this case also, from the FEM analysis results, we see that the torsional oscillation resonance mode around the axial direction does not appear and the sixth mode is not reported because it is more than an order of magnitude higher in frequency and involves only the mutual oscillation of the plates, as in the case of the solid ordinary plate, so it is not of our interest.

	Nastran SOL 103				
Hole diameter D [mm]	**F_1 [Hz]** flex_xz	**F_2 [Hz]** flex_xz	**F_3 [Hz]** long_y	**F_4 [Hz]** tors_xz	**F_5 [Hz]** tors_zx
0	0.978	0.988	3.329	11.65	18.01
6	0.978	0.987	3.291	11.64	17.99
12	0.973	0.982	3.184	11.56	17.90
18	0.953	0.962	3.028	11.21	17.55
30	0.808	0.819	2.351	8.575	14.96

Tab. 4.9: FEM modal analysis results for a sheets elastic suspension model as the diameter of a central hole varies

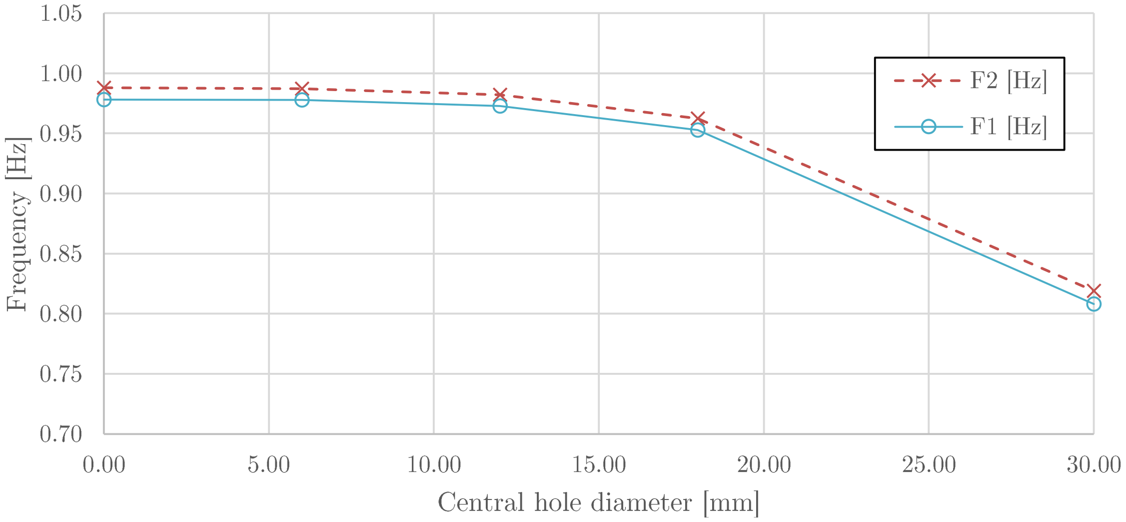

Fig. 4.35: Detail of the first two resonance modes from the graph of the influence of the central hole diameter on modal frequencies

In the following pages are reported the first five oscillation modes plots in the case of a central hole of 30 mm in diameter.

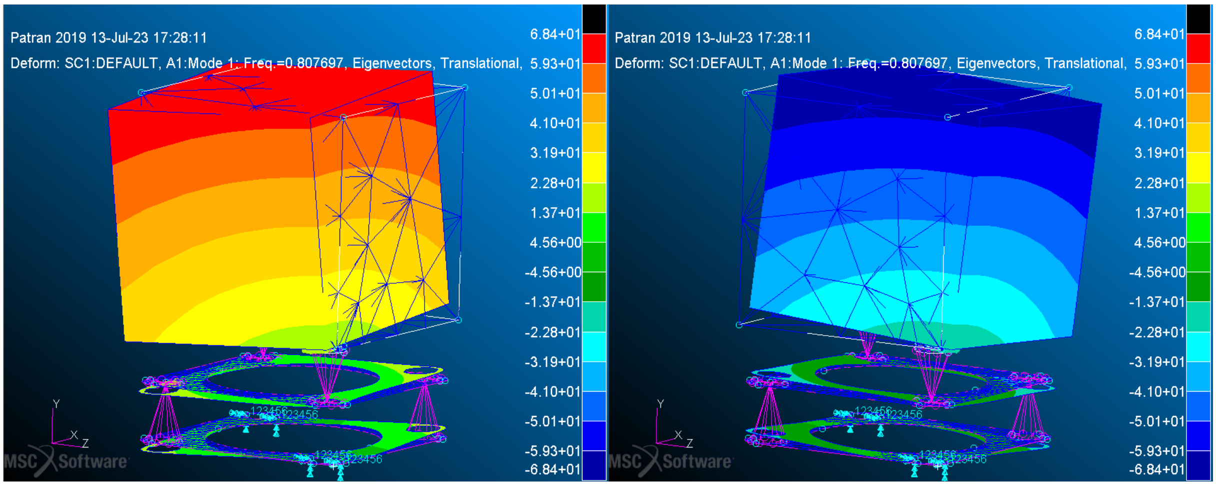

Fig. 4.36: F₁=0.808 Hz (FEM); First bending resonance mode, central hole D = 30 mm

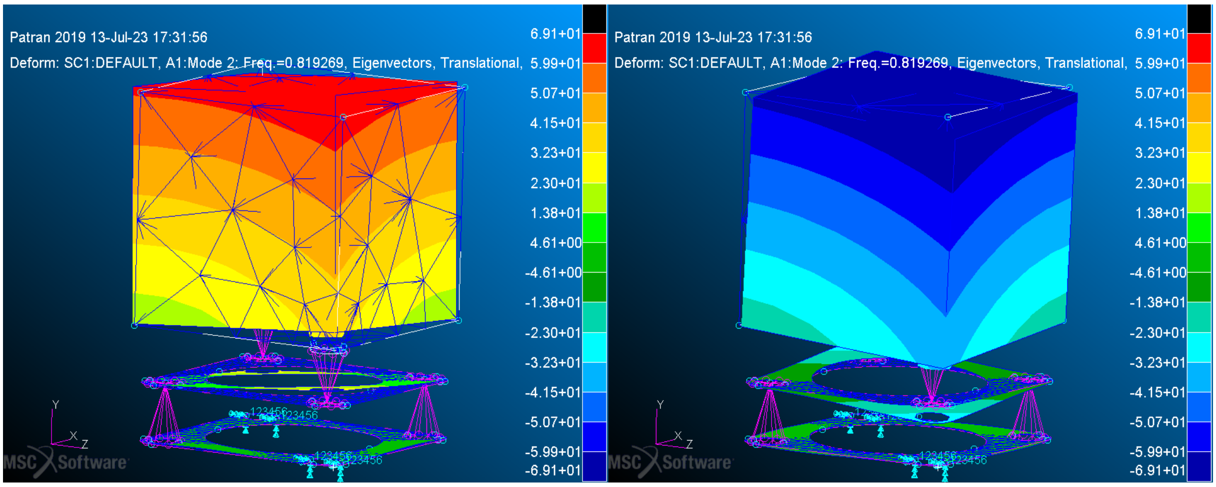

Fig. 4.37: F₂=0.819 Hz (FEM); Second bending resonance mode, central hole D = 30 mm

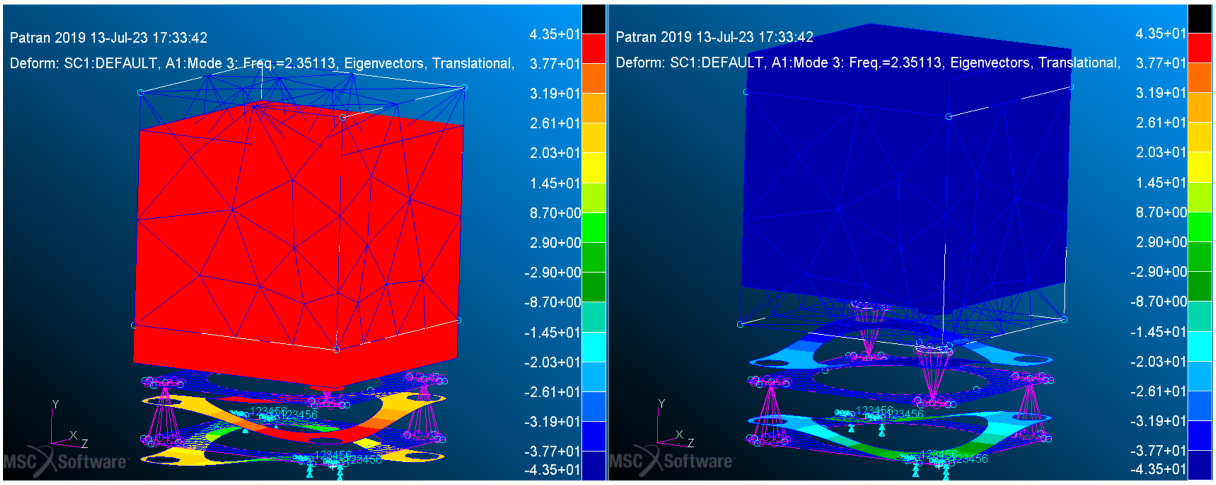

Fig. 4.38: F₃=2.35 Hz (FEM); First longitudinal resonance mode, central hole D = 30 mm

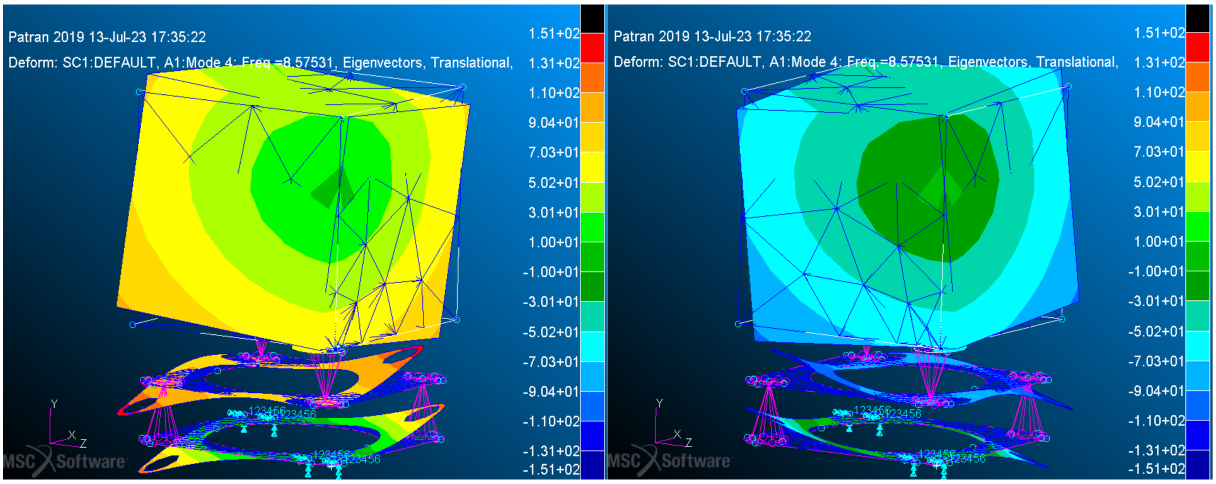

Fig. 4.39: F_4=8.57 Hz (FEM); First twisting resonance mode, central hole D = 30 mm

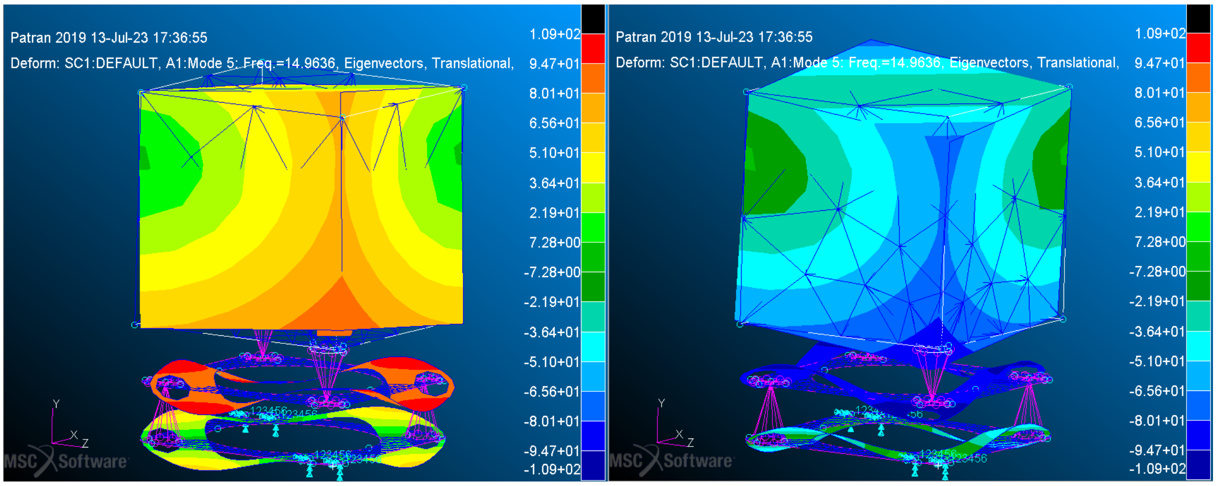

Fig. 4.40: F_5=14.96 Hz (FEM); Second twisting resonance mode, central hole D = 30 mm

The analysis shows that for small holes there is no significant variation in rigidity compared to the solid plate, because they fall within the limits of the section of the diagonal of the plate that does not deform during bending, as can be seen in the following figure.

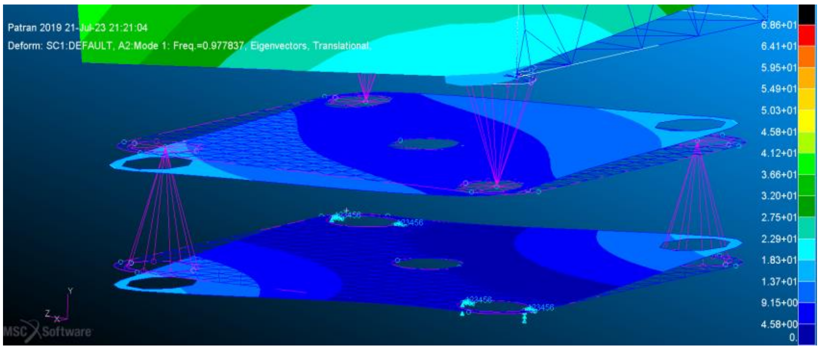

Fig. 4.41: Detail of the first bending mode of the suspension in the case of a plate with a 6 mm hole

Even for holes of large dimensions, the bending rigidity does not decrease significantly, this is because a portion of the plate is removed which already does not contribute much to the deformation in the bending mode.

4.4.3 Sheets Shape Variation: Edge Carving

We now want to evaluate how the modal behaviour of the suspension changes by carving the edges from the outside, so as to reduce the area of the plate that collaborates with the bending mode. In this case everything else will be kept fixed, therefore central holes are not considered and the thickness of the plates is kept at 0.1 mm, as in the previous case.

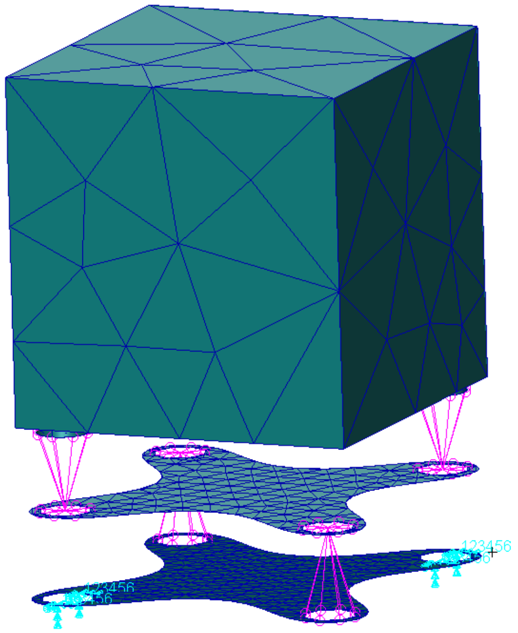

Fig. 4.42: FEM model for the study of the influence of the shape of the plates on the modal frequencies of the elastic suspension, by carving from the outside of the edges such as to remove 534 mm^2 of area compared to the original plate, in the depicted case

Compared to the previous cases, it will now also be necessary to analyse the sixth mode since, although it is still at a much higher frequency, for significant edge cuts it represents the torsional mode around the axial direction which is a displacement mode flexibility that is better to be avoided for our applications.

Carved area from the edges	Nastran SOL 103					
A’ [mm^2]	**F$_1$ [Hz]** flex_xz	**F$_2$ [Hz]** flex_xz	**F$_3$ [Hz]** long_y	**F$_4$ [Hz]** tors_xz	**F$_5$ [Hz]** tors_zx	**F$_6$ [Hz]** tors_y
0	0.978	0.988	3.329	11.65	18.01	-
259	0.858	0.866	3.103	10.059	15.79	-
534	0.679	0.686	2.670	8.066	12.54	127.7

Tab. 4.10: Results of FEM modal analyses for a sheets elastic suspension as the shape of the edges of the sheets varies

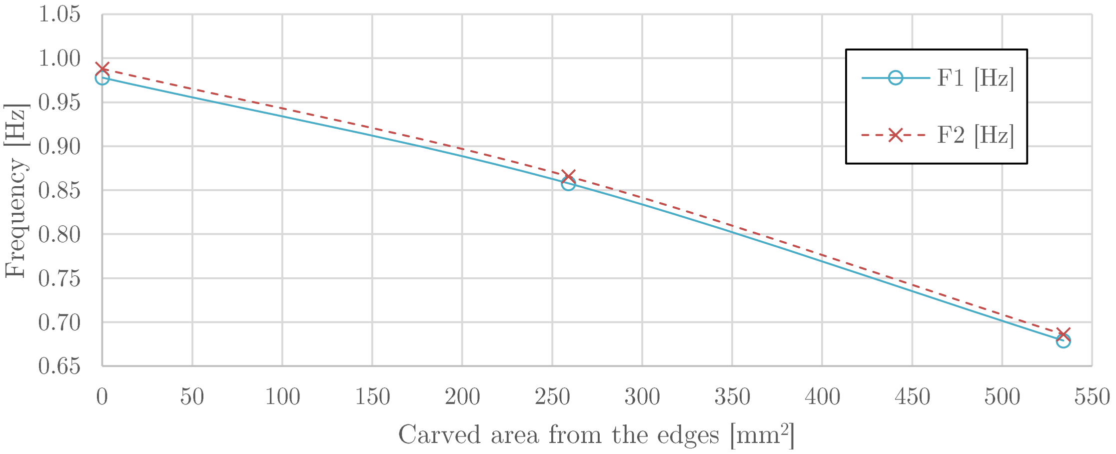

Fig. 4.43: Detail of the first two resonance modes from the graph of the influence of the carved area from the edges on modal frequencies

The plots of the first six resonance modes are reported on the following pages, for the case of a carved area of 534 mm^2 from the edges.

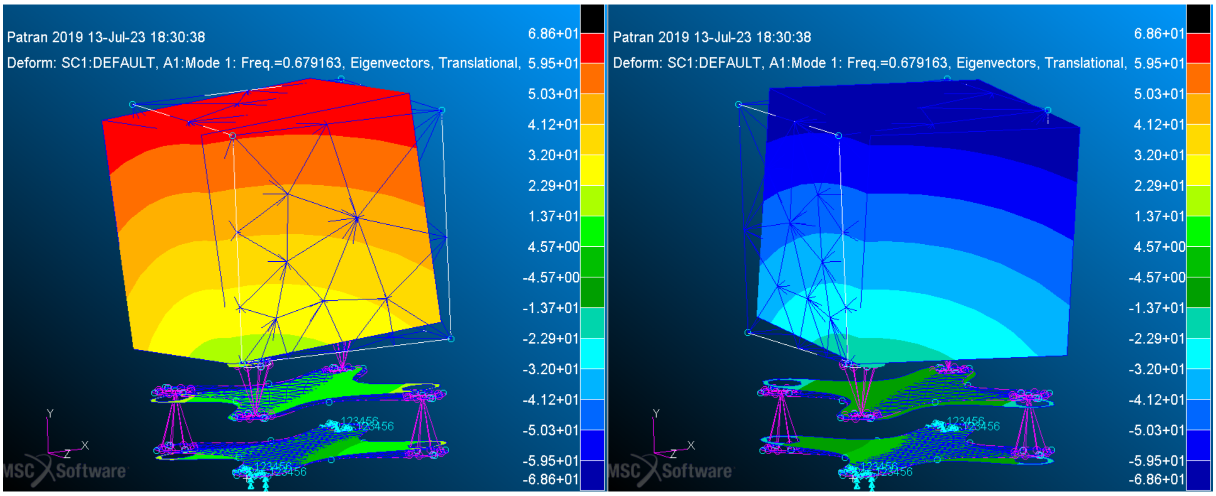
Patran 2019 13-Jul-23 18:30:38

Deform: SC1:DEFAULT, A1:Mode 1: Freq.=0.679163, Eigenvectors, Translational,

Patran 2019 13-Jul-23 18:30:38

Deform: SC1:DEFAULT, A1:Mode 1: Freq.=0.679163, Eigenvectors, Translational,

Fig. 4.44: F$_1$=0.679 Hz (FEM); First bending resonance mode, carved area of 534 mm^2

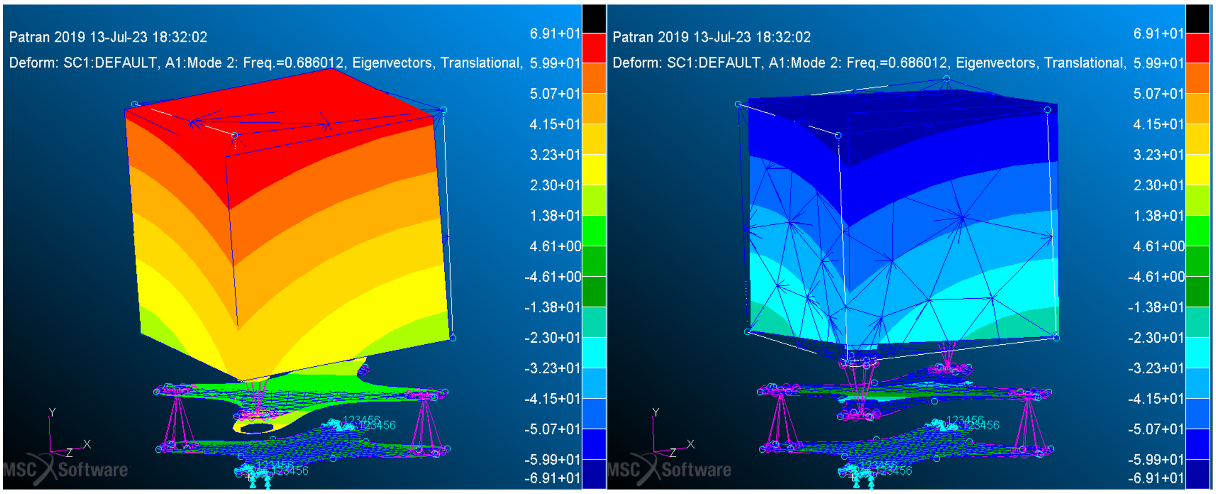

Fig. 4.45: F_2=0.686 Hz (FEM); Second bending resonance mode, carved area of 534 mm^2

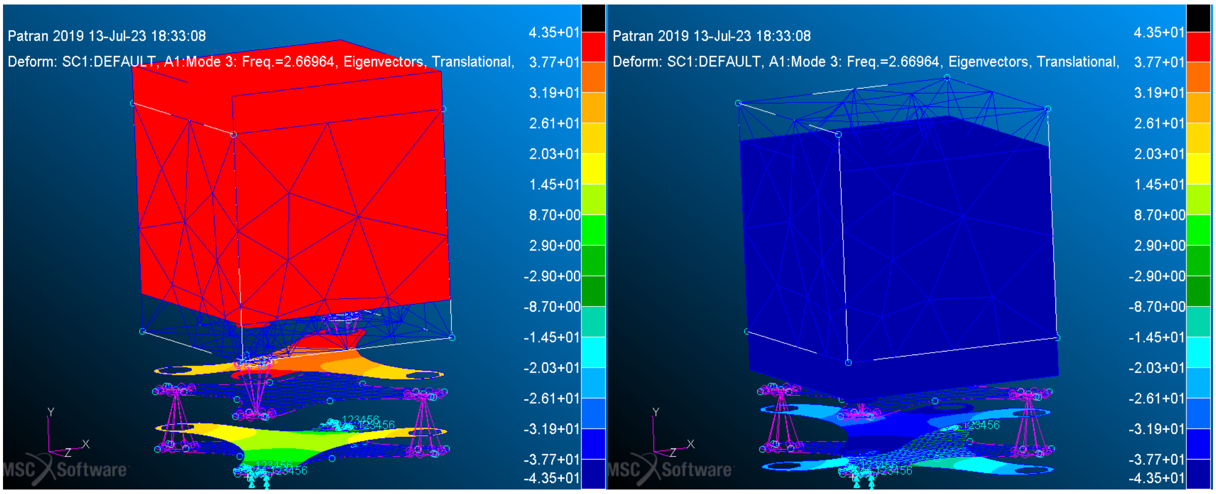

Fig. 4.46: F_3=2.67 Hz (FEM); First elongation resonance mode, carved area of 534 mm^2

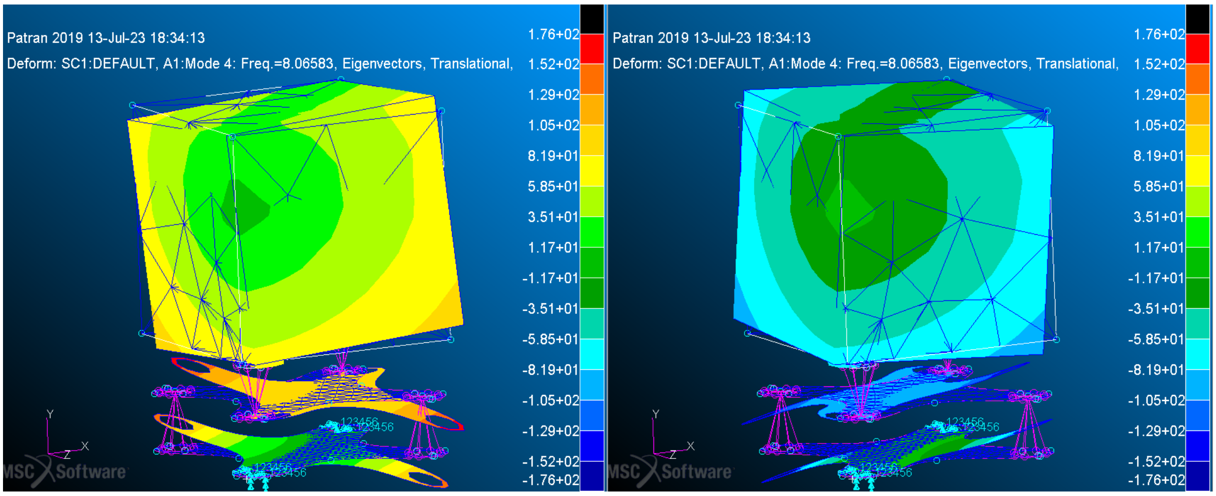

Fig. 4.47: F_4=8.07 Hz (FEM); First torsional resonance mode, carved area of 534 mm^2

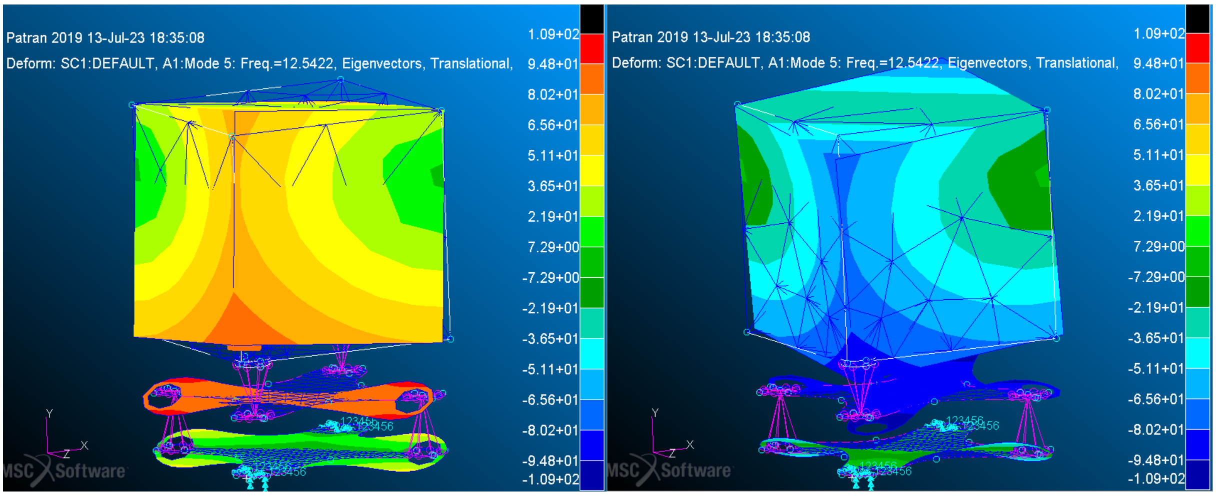

Fig. 4.48: F$_5$=12.5 Hz (FEM); Second torsional resonance mode, carved area of 534 mm^2

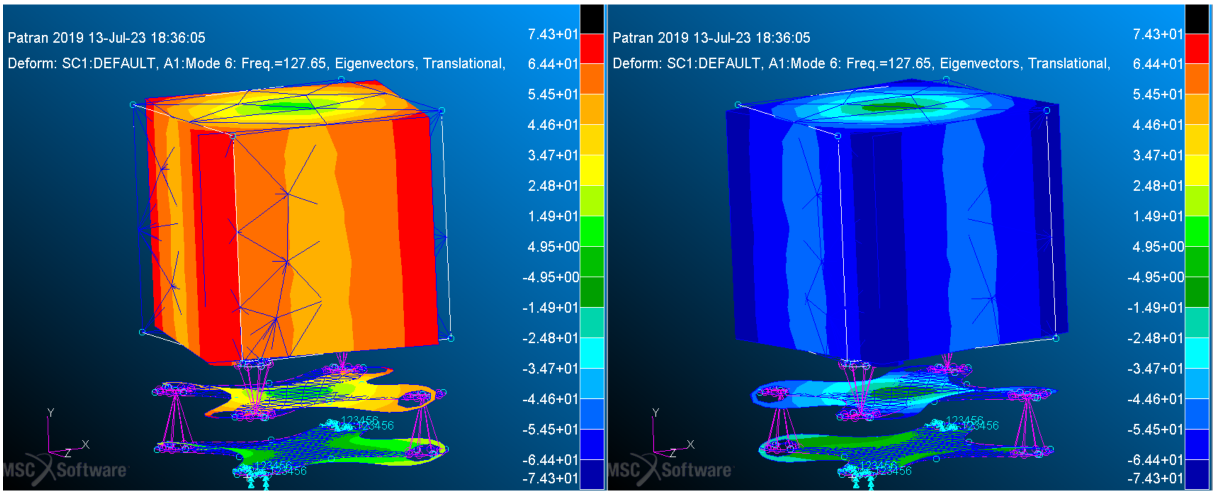

Fig. 4.49: F$_6$=127.7 Hz (FEM); Third torsional resonance mode, carved area of 534 mm^2

It can be observed that for the same cut area from the square plate, if you remove it from the edges you would make the structure more yielding than if you remove it from the centre, as seen previously. This is explained because the central part is the one that contributes the least to the bending rigidity.

Bending stiffness has a quadratic proportionality relative to the frequency:

$$f_n = \frac{\omega}{2\pi}$$

$$\omega = \sqrt{\frac{k}{m}}$$

$$k \propto f_n^2$$

We can compare the influence of the shape variation influence on the bending stiffness between the use of a central hole or carving from the edges:

Central hole diameter D [mm]	**Cut out area from the central hole** A' [mm²]	**Bending resonance mode frequency** F_1 [Hz]	**Bending stiffness relative decrease** $\frac{k}{k_{ref}} = \frac{f^2}{f_{ref}^2}$
0	0.00	0.978	1.000
6	28.27	0.978	0.999
12	113.1	0.973	0.989
18	254.5	0.953	0.948
30	706.9	0.808	0.682

Tab. 4.11: Central hole cut influence on the bending stiffness decrease

Cut out area from the edges A' [mm²]	**Bending resonance mode frequency** F_1 [Hz]	**Bending stiffness relative decrease** $\frac{k}{k_{ref}} = \frac{f^2}{f_{ref}^2}$
0.00	0.978	1.000
259.06	0.858	0.769
534.00	0.679	0.482

Tab. 4.12: Edge carving influence on the bending stiffness decrease

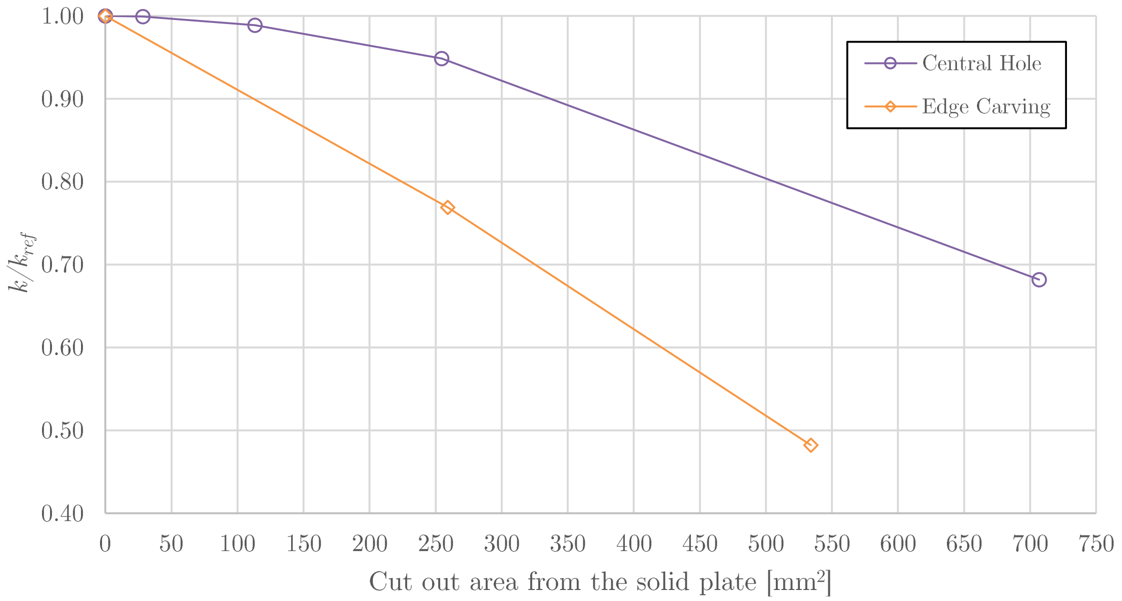

Fig. 4.50: Comparison of the influence between the two solutions for removing material from the square plate on the bending stiffness reduction

4.4.4 Rotation Centre Determination Method

If we wanted to evaluate the influence of the variation in the number of sheets and that of the relative spacing in an independent way, it would be necessary to know how to determine the rotation lever arm of the oscillation, the variation of which would influence the oscillation frequency.

Let's consider a simplified lumped parameter model of the bending behaviour of the sheets elastic suspension, seen as a torsional spring. We want to find an analytical method to calculate the position of the virtual rotation centre of the mass-spring oscillating system, with a pendulum analogy, in a similar fashion to what was previously accomplished in the 3.1.5 subsection. The resolution comes from setting the resonance frequency, calculated by the FEM analysis, in the equation of the dynamics of the pendulum oscillation of the simplified model, thus deriving the elastic constant of the lumped spring which is to be matched with the bending stiffness obtained with static FEM tests. The lumped parameter model of the pendulum oscillation is therefore an undamped mechanical system free to oscillate according to a single rotational degree of freedom, whose behaviour is described by the dynamic equilibrium equation:

$$I\ddot{\theta} + K_t\theta = 0$$

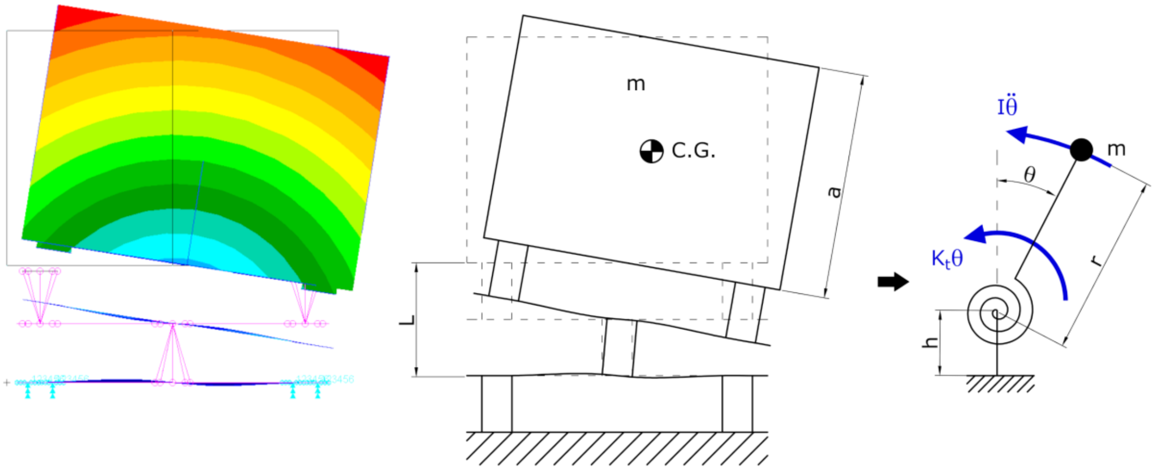

Fig. 4.51: From FEM model to a lumped parameter model for the generic bending resonance mode for a multiple sheets elastic suspension

The test mass of the simplified model is considered to be concentrated and free to rotate rigidly around a pivot point at a certain height h from the clamp, i.e. from the first plate rigid with the base support, with a lever arm r with respect to the centre of gravity of the test mass which is the radius of the rotation centre that we want to obtain. The forces at play are those of the elastic return of the lumped torsional spring, which represents the sheets elastic suspension bending stiffness, and the force due to the rotational inertial acceleration of the mass around the fulcrum.

Let's see the terms of the dynamic equilibrium equation of the lumped parameter system:

$$I\ddot{\theta} + K_t\theta = 0$$

Adopting as a reference the model previously used to study the influence of the design parameters (2 sheets, solid plates, thickness of 0.1 mm and mutual spacing of 10 mm, see Fig. 4.27 on page 76):

- $I = I_0 + m \cdot r^2$
  Moment of inertia around the rotation centre, according to the *Huygens–Steiner theorem*, where *I_0* is the second moment of inertia relative to the cube centroid, the rotation radius *r* is unknown. Knowing the Beryllium-Copper test mass:
  $$m = V \cdot \rho = (40\,mm)^3 \cdot 8.25E-09\frac{t}{mm^3}$$
  $$m = 5.28E-4\,t = 0.528\,kg$$
  $$I_0 = m\frac{a^2}{6} = 0.1408\ \,t\,mm^2$$
- The distance between the sheet clamped to the base support and the centre of gravity of the test mass is known from the geometry:
  $$h + r = L + \frac{a}{2} = 20\,mm + \frac{40}{2}mm = 40\,mm$$
- K_t
  Elastic constant of the lumped torsion spring which represents the overall bending stiffness of the bending resonance mode. It can be evaluated both from the FEM static analysis of the same model (see Fig. 4.52 on page 89), with a bending load in the same direction as the first resonance mode, and from the FEM modal analysis (see Fig. 4.27 on page 76).

It can be traced back to a homogeneous second degree differential equation:

$$\ddot{\theta} + \omega_n^2\theta = 0$$

With:

- $\omega_n = \sqrt{\frac{K_t}{I}}$: Natural angular frequency of the oscillation

The natural resonance frequency can be therefore written as following:

$$f_n = \frac{\sqrt{\frac{K_t}{I_0 + m \cdot r^2}}}{2\pi} \quad [Hz] \tag{4.1}$$

From the FEM modal analysis, the frequency of the first bending resonance mode has already been established (see Fig. 4.27 on page 76):

$$f_{n,FEM} = 0.978\, Hz$$

Setting the frequency as a datum, the stiffness K_t can be obtained from the (4.1):

$$K_t = f_{n,FEM}^2 4\pi^2 (I_0 + mr^2) \left[\frac{Nmm}{rad}\right]$$

If we write r as a function of h, rotation centre position of the suspension, we get:

$$K_t = f_{n,FEM}^2 4\pi^2 m \cdot \left[I_0 + \left(L + \frac{a}{2} - h\right)^2\right] \left[\frac{Nmm}{rad}\right] \tag{4.2}$$

At this point we want to obtain the same stiffness from a static FEM analysis, as previously done for the single plate (see subparagraph 4.2.1 on page 58) but for the overall suspension instead. In the FEM model made for the static analysis that will investigates the K_t, the elastic suspension is kept unchanged but the test mass is cut out and the torque is imposed by a force in the same direction of oscillation of the first bending mode and from a point in a different position from the centre of the test mass, to avoid obtaining the trivial solution. This point is placed at 30 mm from the base.

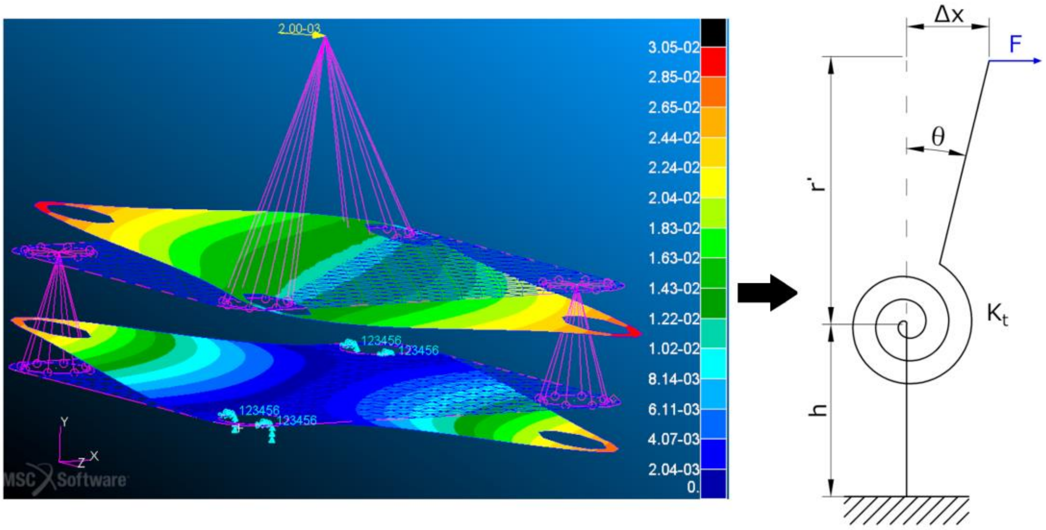

Fig. 4.52: FEM model and pendulum analogy made for investigating the bending stiffness K_t

$$K_t = \frac{F\,r'}{\vartheta}$$

with:

$$\vartheta \cong \left(\frac{\Delta x}{r'}\right)\ [rad]$$

$$h + r' = L' = 30\,mm$$

A FEM linear static analysis (Nastran SOL 101) is carried out to find the stiffness *Kt* of the aforementioned elastic suspension, which resulting graphs are shown in Fig. 4.52, with a force F in the direction of the first resonance mode (see Fig. 4.27 on page 76) of a value of 2.00E-03 N, set to fall within the limits in which the sheets have a linear elastic response (see Fig. 4.10 on page 61). The displacement values of the nodes are obtained in the output file with “f06” extension. The node of interest is the one corresponding to the force F application and has a node identifier of ID 1531, from which the displacements in the three directions can be read in the file, equal to:

```
                         D I S P L A C E M E N T   V E C T O R
      POINT ID.            T1                      T2                      T3
           1531      3.137928E-02           -3.231237E-06            3.135951E-02
```

The overall displacement is thus calculated, which can be approximated to be the aforementioned *Δx* of the lumped parameter model in Fig. 4.52:

$$diplac._{ID1530} \approx \Delta x$$

$$diplac._{ID1530} = \sqrt{(\Delta T1)^2 + (\Delta T2)^2 + (\Delta T3)^2}$$

$$\Delta x = 4.4363E - 02\,mm$$

Recalling that in the lumped parameter model we have:

$$K_t = \frac{F\,r'^2}{\Delta x}\left[\frac{Nmm}{rad}\right]$$

$$h + r' = L' = 30\,mm$$

We can therefore write the rotation centre position as follows:

$$h = L' - \sqrt{K_t \frac{\Delta x}{F}}\quad [mm] \tag{4.3}$$

It is worth noting that h and K_t are interdependent in the (4.2) and (4.3) equations, in order to find a solution we can thus proceed with an iterative or analytical method:

- **Iterative solution**: Starting from a zero value of h, therefore with the centre of rotation considered at the bottom, we substitute $h = 0$ in the dynamic equation (4.2) from which we find the corresponding stiffness. With this stiffness we repeat the static calculation of the position of the rotation centre (4.3) and so on iteratively:

1. $h_1 = 0\,mm$

$$K_{t,1} = f_{n,FEM}^2 4\pi^2 m \cdot \left[I_0 + \left(L + \frac{a}{2} - 0\right)^2\right] = 31.92\,\frac{Nmm}{rad} \tag{4.2}$$

2. $$h_k = 0.5\,mm - \frac{a}{2} + \sqrt{K_t\frac{\Delta x}{F}}\;[mm] \tag{4.3}$$

3. $$K_{t,k+1} = f_{n,FEM}^2 4\pi^2 m \cdot \left[I_0 + \left(L + \frac{a}{2} - h_k\right)^2\right]\;\left[\frac{Nmm}{rad}\right] \tag{4.2}$$

4. - If $|h_{k+1} - h_k| < 0.01$ then *STOP*
   - If $|h_{k+1} - h_k| > 0.01$ then *Repeat 2.*

$\boldsymbol{k}$	$\boldsymbol{h_k}$ $\boldsymbol{[mm]}$	$\boldsymbol{K_{t,k+1}}$ $\boldsymbol{\left[\frac{Nmm}{rad}\right]}$
1	0.000	37.24
2	1.260	35.26
3	2.034	34.07
4	2.508	33.36
5	2.797	32.93
6	2.973	32.67
7	3.081	32.51
8	3.146	32.41
9	3.186	32.36
10	3.210	32.32
11	3.225	32.30
12	3.234	32.29
13	**3.239**	**32.28**

Tab. 4.13: Iteration results to find the centre of rotation and stiffness for the first bending resonance mode

The results of the position of the centre of rotation of the two sheets elastic suspension and the bending stiffness are thus obtained from the iteration:

$$h = 3.24\,mm$$

$$K_t = 32.3\,\frac{Nmm}{rad}$$

- **Analytic solution**: The iterative method does not require complex calculations, however it is computationally expensive, requiring 18 iterations to obtain a satisfactory result. If instead we want to pursue an analytical method we have to solve the nonlinear system of two equations (4.2) and (4.3) to find a formulation that provides the exact results.

  By replacing the (4.3) into the (4.2) equation, we can write:

$$K_t = f_{n,FEM}^2 4\pi^2 m \cdot \left[I_0 + \left(L + \frac{a}{2} - h\right)^2\right] \tag{4.2}$$

- $$h = L' - \sqrt{K_t \frac{\Delta x}{F}} \tag{4.3}$$

$$K_t = f_{n,FEM}^2 4\pi^2 I_0 + f_{n,FEM}^2 4\pi^2 m \cdot \left(L + \frac{a}{2} - L' + \sqrt{K_t \frac{\Delta x}{F}}\right)^2$$

$$K_t\left(\frac{\Delta x}{F} f_{n,FEM}^2 4\pi^2 m - 1\right) + \sqrt{K_t}\left[2 f_{n,FEM}^2 4\pi^2 m \left(L + \frac{a}{2} - L'\right)\sqrt{\frac{\Delta x}{F}}\right] + f_{n,FEM}^2 4\pi^2 I_0 + f_{n,FEM}^2 4\pi^2 m\left(L + \frac{a}{2} - L'\right)^2 = 0$$

We thus obtain a second degree equation if the variable $\sqrt{K_t}$ is considered instead:

$$C_1\left(\sqrt{K_t}\right)^2 + C_2\sqrt{K_t} + C_3 = 0$$

Using the quadratic formula we can resolve the two solutions of the equation:

$$K_t = \left(\frac{-C_2 \pm \sqrt{C_2^2 - 4C_1C_3}}{2C_1} \right)^2 \tag{4.4}$$

with:

- $C_1 = \frac{\Delta x}{F} f_{n,FEM}^2 4\pi^2 m - 1$
- $C_2 = 2 f_{n,FEM}^2 4\pi^2 m \left(L + \frac{a}{2} - L' \right) \sqrt{\frac{\Delta x}{F}}$
- $C_3 = f_{n,FEM}^2 4\pi^2 I_0 + f_{n,FEM}^2 4\pi^2 m \left(L + \frac{a}{2} - L' \right)^2$

Once K_t has been calculated from (4.4), h is obtained through the (4.2) equation, in fact the rotation lever arm of the mass-spring system can also be written as:

$$r = L + \frac{a}{2} - h$$

The first solution of the (4.4) formula, will give the following results:

$$K_t = 5.335 \, \frac{Nmm}{rad} = 0.0931 \, \frac{Nmm}{deg}$$

$$h = 19.122 \, mm$$

$$r = 20.878 \, mm$$

The second solution of the (4.4) is instead:

$$K_t = 32.266 \, \frac{Nmm}{rad} = 0.5631 \, \frac{Nmm}{deg}$$

$$h = 3.2474 \, mm$$

$$r = 36.753 \, mm$$

The second analytical solution is the same obtained by the iterative method and provides reasonable values, while the first would indicate a rotation pivot point too far above the bottom and therefore physically impossible, with a stiffness value resulting only as a mathematical artifice. Consequently this second analytical solution is chosen to model the bending oscillation behaviour of the elastic suspension with the lumped parameter model of the "pendulum" analogy, as shown in the following figure.

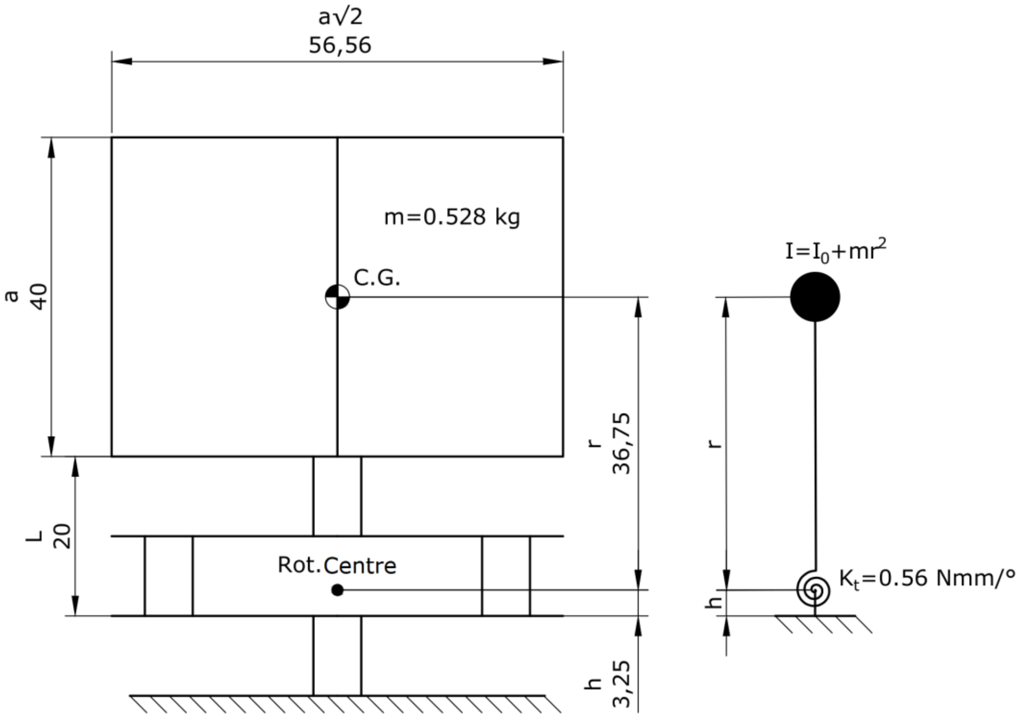

Fig. 4.53: CAD con quotature del risultato del calcolo del centro di rotazione del primo modo flessionale per sospensione a 2 lamine.

The same method can be applied for the second bending resonance mode, which frequency is known from the FEM modal analysis (see Fig. 4.28 on page 76), close in value to that of the first mode:

$$f_{n,FEM} = 0.988\,Hz$$

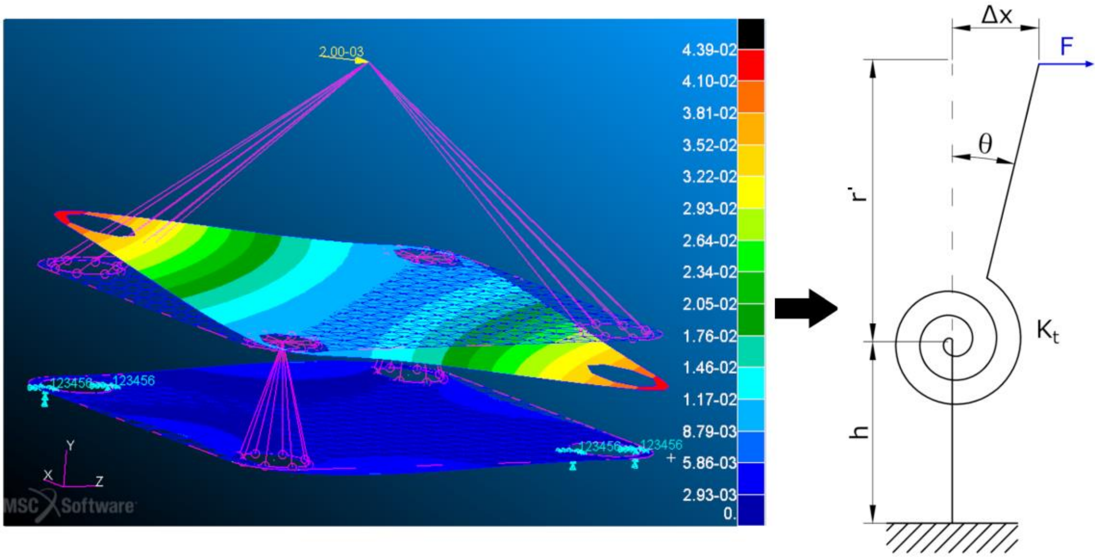

Fig. 4.54: FEM model and static test with displacements results plot [mm] and lumped parameter analogy to find the stiffness K_t of the second bending resonance mode for a two-sheets suspension

Results of the rotation centre obtained for the second bending mode are very similar to those of the first mode, as could be anticipated:

$$K_t = 31.225\,\frac{Nmm}{rad} = 0.5450\,\frac{Nmm}{deg}$$
$$h = 4.3782\,mm$$
$$r = 35.622\,mm$$

The method here presented can therefore be used to carry out analyses as the number of sheets of the suspension varies but at a fixed rotation lever arm or, in alternative, to evaluate the influence of the rotation radius as the spacing of the sheets increases.

4.4.5 Number of Sheets Variation

We proceed to evaluate the influence of different number of plates used in the suspension on the frequency response. In this analysis all other variables are kept constant, including the rotation lever arm of the first bending mode, as the one just calculated for two sheets case before. The sheets have standard geometry without cuts or holes and a thickness of 0.1 mm is maintained. We also want to study the difference between having an odd or even number of sheets, so the analyses are carried out from 1 to 4 sheets, equally spaced out.

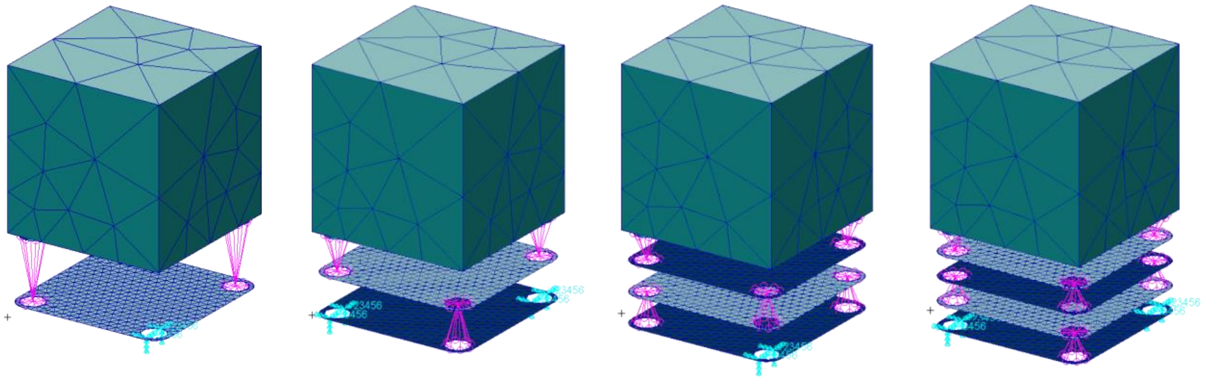

Fig. 4.55: FEM models to study the influence of the plates number, keeping the rotation radius fixed

To keep the rotation arm constant when the number of plates varies, the distance between the clamped bottom sheet and the mass will have to change. The resulting models are directly reported in the previous figure, omitting the iterative trial and error procedure that defined the spacing, based on the search for the centre of rotation presented in the previous paragraph, to ensure that we always have approximately the same rotation lever arm *r*.

Number of sheets	**Nastran SOL 103** **F_1 [Hz]** flex_xz	 **F_2 [Hz]** flex_xz	 **F_3 [Hz]** long_y	 **F_4 [Hz]** tors_xz	 **F_5 [Hz]** tors_zx
1	1.352	1.356	4.719	-	-
2	0.978	0.988	3.329	11.65	18.01
3	0.797	0.797	2.717	10.24	10.27
4	0.692	0.693	2.353	8.412	8.891

Tab. 4.14: FEM modal analysis results for different multiple sheets elastic suspensions as the number of sheets varies, at a constant rotation radius

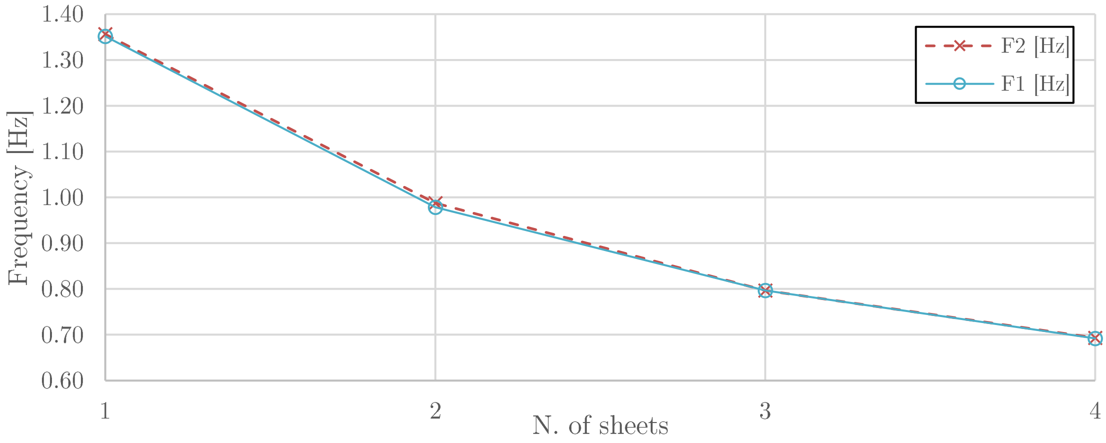

Fig. 4.56: Detail on the first two resonance modes from the graph of the influence of the number of plates of the elastic suspension on the modal frequencies, for the same virtual rotation arm

For the single sheet case suspension, the resonance modes after the third one are deformations of the plate alone at high frequencies, thus not of interest.

Referring to the terms reported in the following Fig. 4.57, the data and results of the *rotation centre determination method* are reported for the four cases, in order to achieve a constant rotation arm r. The method is described in the previous section, from which the distance L, in which the n sheets must be equally spaced, is derived.

N. of sheets	**Modal (SOL 103)** **L [mm]**	**f_1 [Hz]**	**Static (SOL 101)** **L' [mm]**	**F [N]**	**Δx [mm]**	**r [mm]**	**h [mm]**	**K_t [Nmm/rad]**
1	16.75	1.352	16.75	0.002	0.009	**36.68**	0.07	61.69
2	20.00	0.978	30.00	0.002	0.044	**36.75**	3.25	32.27
3	22.80	0.797	32.80	0.002	0.067	**36.66**	6.14	21.31
4	24.00	0.692	34.00	0.002	0.088	**36.65**	7.35	16.07

Tab. 4.15: Determination of L for suspension of different sheets number, in order to obtain a constant r using the aforementioned *rotation centre determination method*

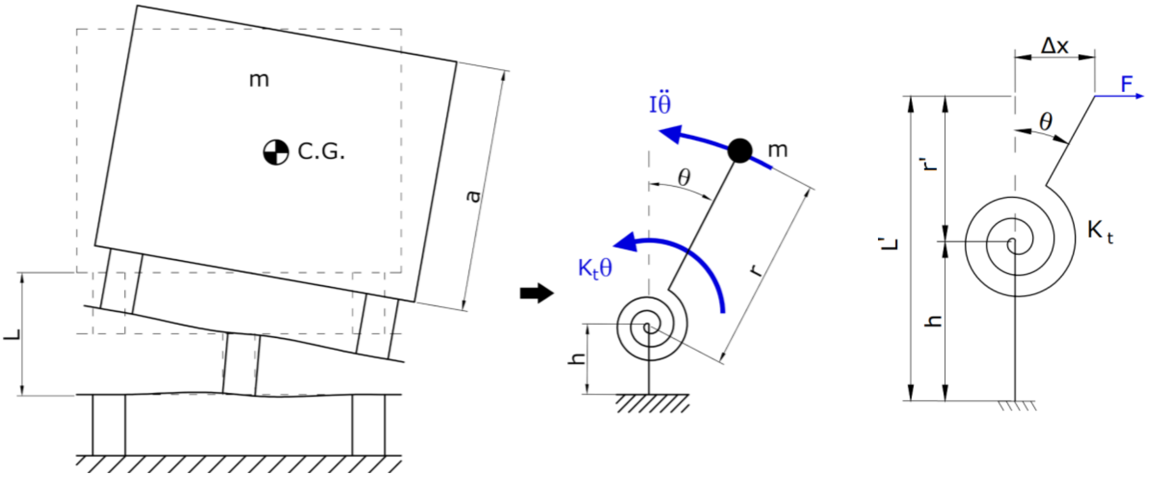

(a) (b)

Fig. 4.57: Modal analysis model (a) and static analysis model (b) necessary to determine the position of the rotation centre

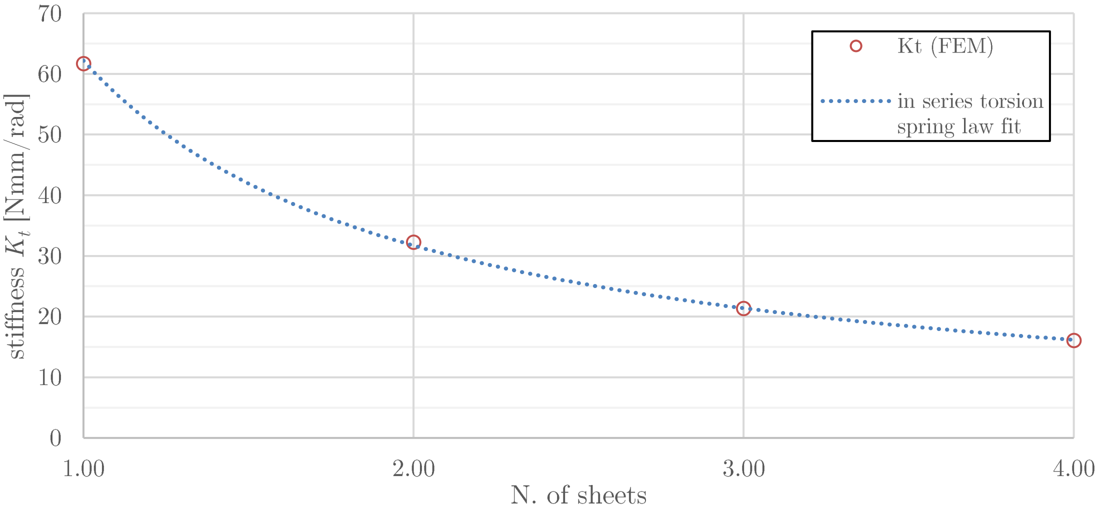

Fig. 4.58: Bending stiffness of the suspension as the number of sheets varies and comparison with the hyperbolic law considering torsion springs in series

It can be observed how the stiffness K_t varies as the number of laminae varies in accordance to the lumped parameter model, in which each lamina $K_{t,i}$ constitutes a torsion spring with stiffness equal to that of the case of the single sheet and the equivalent stiffness in the case of n sheets is obtained from the torsion springs in series formula:

$$\frac{1}{K_{t,eq}} = \sum_{i=1}^{n} \frac{1}{K_{t,i}}$$

$$K_{t,eq} = \frac{K_{t,i}}{n}$$

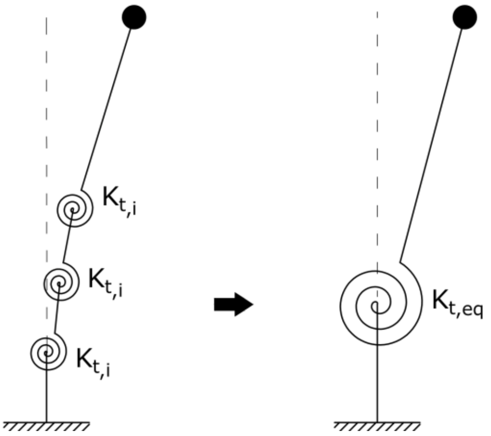

Fig. 4.59: Torsion springs in series, analogous to the multiple sheets elastic suspension

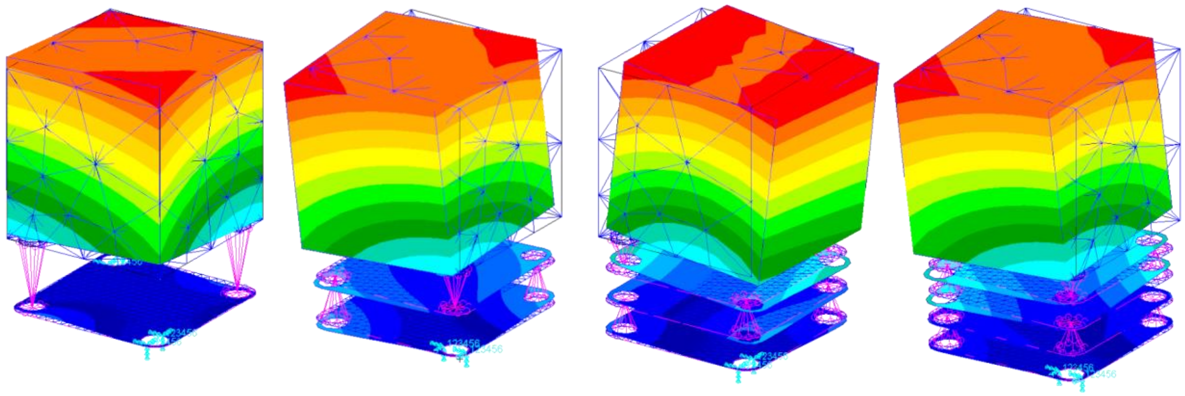

Fig. 4.60: Displacements plots comparison of the first bending resonance mode of the foil suspension types as the number of sheets changes, keeping the rotation lever arm constant

From the results of the modal analyses it can be observed that for the three-sheets case, the two bending modes oscillate in the directions of the sides of the cube and not of the diagonals as in the other cases and both the two bending modes and the first two torsional modes are more similar in frequency between each other compared to the other cases, indicating greater symmetry of the system. Of course this results are valid for the simplified FEM model in which there were not considered additional masses of the rivets or supports that would alter the symmetry, in fact by considering these, we will see that the results are homogenized also for the two-sheets case. Furthermore we have to take into consideration that even if ideally giving better results, a greater number of plates implies a greater assembly complexity.

4.4.6 Sheets Distancing Variation

Having set the number of sheets at 2, as for the other influence studies, we want to investigate how the modal behaviour changes as the distance between the first clamped bottom plate and the test mass varies, therefore as the rotation arm of the oscillation changes. 4 FEM modal analyses are thus reiterated with the reference model (the one of the analyses reported in Fig. 4.27 on page 76) by varying the parameter L (see Fig. 4.57 (a) on page 97) from 5 to 20 mm and subsequently, from time to time, the bending mode rotation arm r will be evaluated with the method in section 4.4.4, where we considered the case with L equal to 20 mm. The second plate is located at $L/2$ between the first plate and the bottom surface of the test mass.

Nastran SOL 103

	F$_1$ [Hz]	**F$_2$ [Hz]**	**F$_3$ [Hz]**	**F$_4$ [Hz]**	**F$_5$ [Hz]**
***L* [mm]**	flex_xz	flex_xz	long_y	tors_xz	tors_zx
10	1.192	1.197	3.330	19.03	29.70
15	1.077	1.084	3.330	14.09	21.87
20	0.978	0.988	3.329	11.65	18.01
25	0.894	0.905	3.330	10.20	15.70

Tab. 4.16: FEM modal analysis results of a 2-sheets elastic suspension as the spacing between plates $L/2$ varies

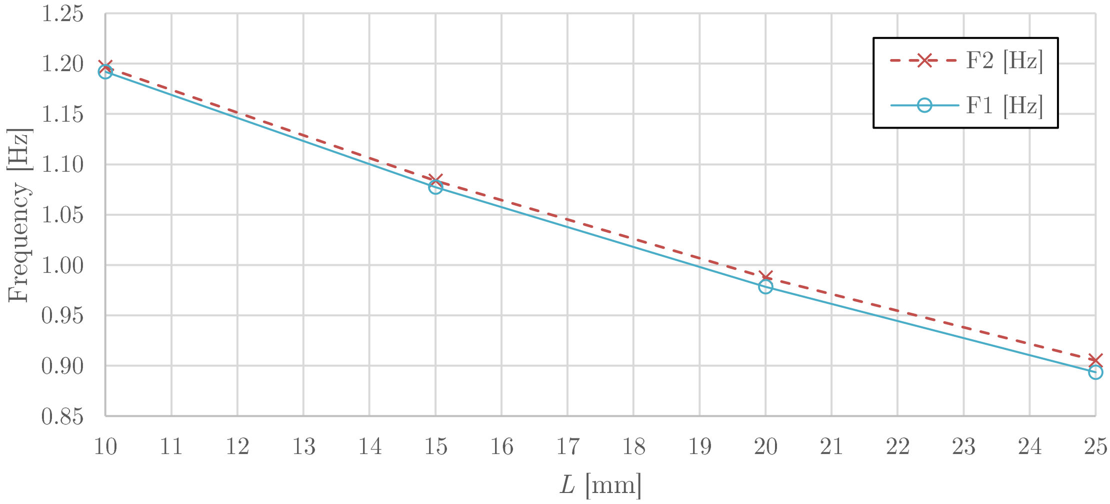

Fig. 4.61: Detail of the first two bending modes from the graph of the influence of the vertical length of a two-sheets suspension on the resonance frequencies

Referring to the geometric terms in Fig. 4.57 on page 97, the data and results of the *rotation centre determination method* for the four cases are subsequently reported.

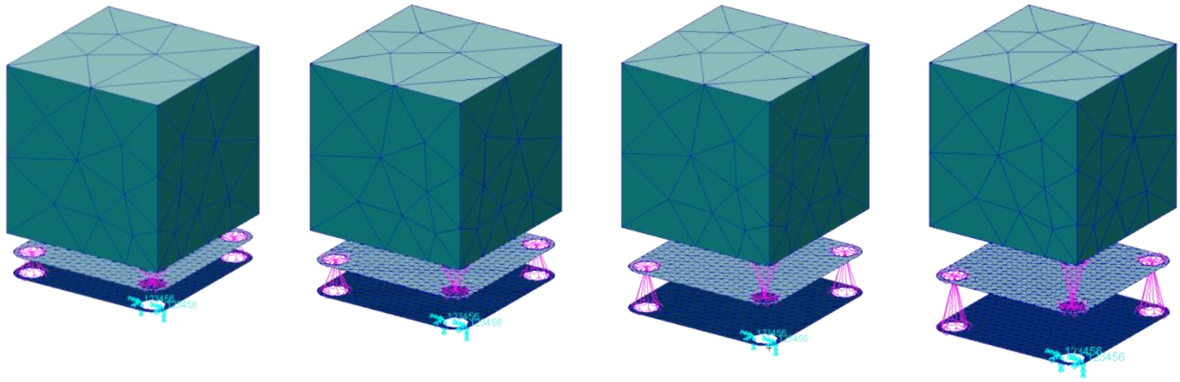

Fig. 4.62: Four FEM models for the study of the influence of different plate spacing

Modal (SOL 103)		**Static (SOL 101)**					
L [mm]	f_1 [Hz]	L' [mm]	F [N]	Δx [mm]	r [mm]	h [mm]	K_t [Nmm/rad]
10	1.192	20.00	0.002	0.021	27.97	2.03	31.07
15	1.077	25.00	0.002	0.031	32.32	2.68	31.72
20	0.978	30.00	0.002	0.044	36.75	3.25	32.27
25	0.894	35.00	0.002	0.060	41.24	3.76	32.74

Tab. 4.17: Rotation centre determination method results, for different L distances

Having found how r changes with L, we can write the relation between the frequency and the rotation radius which, according to the lumped parameter model, is calculated starting from the dynamics equation, this relation is the (4.1) equation on page 89:

$$I\ddot{\theta} + K_t\theta = 0$$

$$f_n = \frac{\sqrt{\dfrac{K_t}{I_0 + m \cdot r^2}}}{2\pi} \quad [Hz]$$

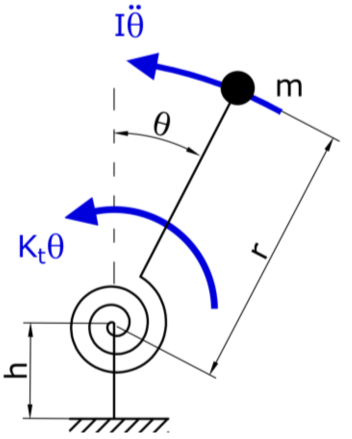

Fig. 4.63: Lumped parameters model

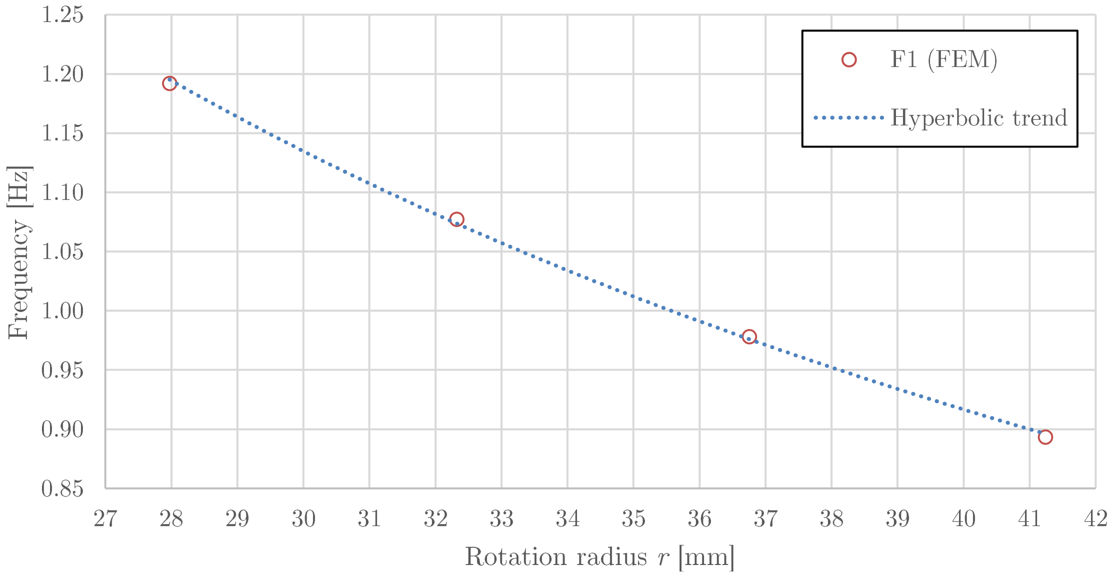

Fig. 4.64: Bending resonance mode frequency of the suspension as a function of the virtual rotation lever arm

It can be observed how the frequency f_n varies with the rotation arm r in accordance to the lumped parameter model, in fact from the previous formula it can be deduced that:

$$f_n \propto \frac{1}{r}$$

It can be observed from these results that the bending stiffness of the lumped parameter model obtained remains approximately constant, this is because the number of plates is kept at a number of two. The spacing distance of the sheets, however, is a parameter limited by space restrictions, in fact theoretically a longer arm is preferable but this implies a greater volume occupied by the suspension for a small advantage. It is required to stay within a total suspension height limit of 70 mm and a smaller total dimension with the same performances is always preferable for space applications.

4.4.7 Constraint Conditions

During the assembly phase, the possibility of having a single separator between the sheets can be taken into consideration to allow a support for the rivets. This solution would make the structure more constrained compared to the cases studied previously where the rivets, seen as a rigid connections, were independent. We therefore want to study the difference in modal behaviour between these two solutions. To simulate the constraint conditions due to a single rivet support separator between one sheet and another, it will be sufficient to build a single *RBE2* type *MPC* for both of the two diagonal rivets of the plate instead of making two separate ones.

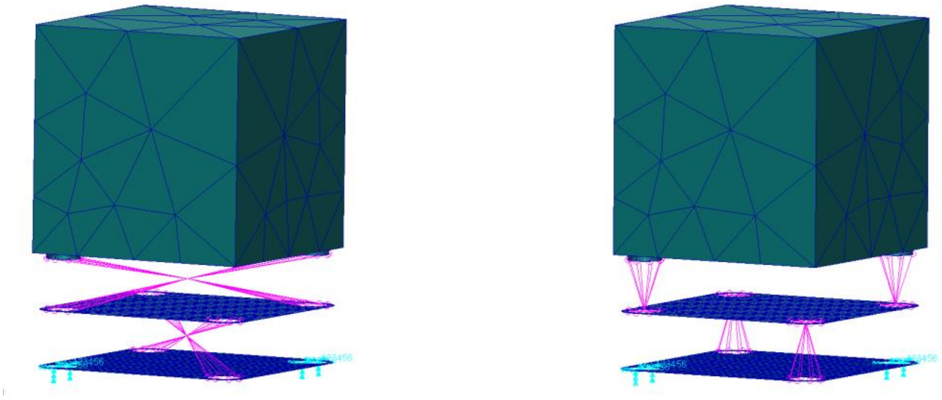
(a) (b)

Fig. 4.65: Models of mutually constrained rivets with a single separator (a) and independent rivets (b).

Nastran SOL 103

Constraint conditions	**F_1 [Hz]** flex_xz	**F_2 [Hz]** flex_xz	**F_3 [Hz]** long_y	**F_4 [Hz]** tors_xz	**F_5 [Hz]** tors_zx
(a)	0.988	0.988	3.329	17.85	18.01
(b)	0.978	0.988	3.329	11.65	18.01

Tab. 4.18: FEM modal analyses results for the two aforementioned constraint conditions

From these results it can be deduced that in case (a) there is a symmetry homogenization of both the two lateral bending and the two torsional resonance modes, leaving the frequencies practically unchanged. This is explained by the fact that in case (b), which is the one we used for the entire study of the influence of the parameters, the upper plate already had the rivets mutually constrained, because they were rigidly fixed to the mass, unlike the lower plate. This creates an asymmetry for a two-sheets suspension. Furthermore from the modal analysis it appears that in the case (a) of mutually constrained rivets, the directions of bending oscillations are not diagonal as in the case (b) but parallel to the sides of the cube, as shown in the following picture.

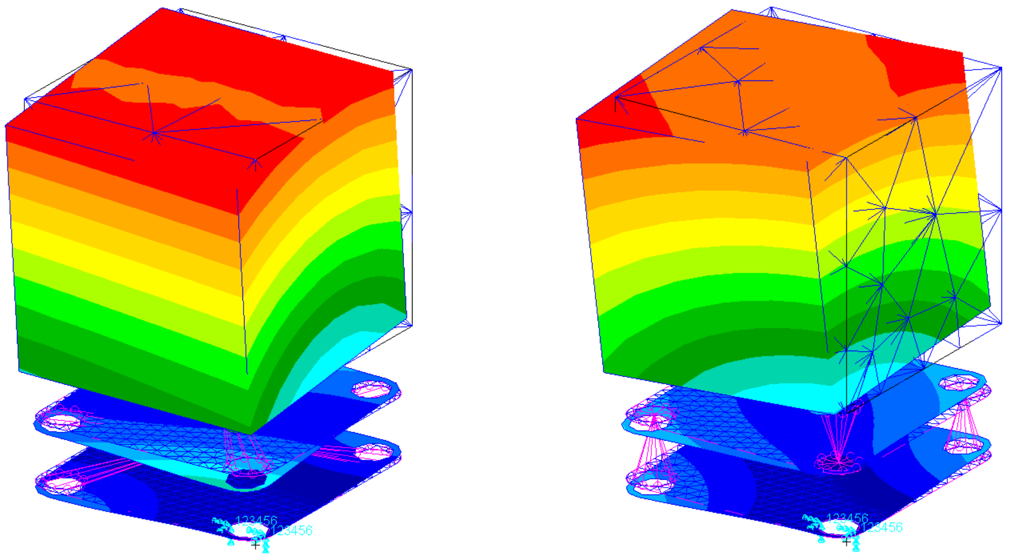

(a) (b)

Fig. 4.66: Displacements plot comparison of the first bending mode between the case with mutually restrained rivets with the same separator (a) and the independent rivets case (b)

For a three-sheets suspension the modal behaviour remains practically unaltered by changing the state of mutual constraint of the rivets, since the oscillation was already in the direction parallel to the faces of the cube and not diagonal and the two bending resonance frequencies were already equal.

4.5 Design Proposals

During the design phase, our purpose will be to achieve the bending resonance frequency requirement of less than 1 Hz. Theoretically, a frequency as low as possible is desirable, but we have to take into consideration the constraints of the limit volume box of 40 × 40 × 70 mm, the complexity of the assembly and stress resistance.

As seen in the previously conducted study in the past paragraphs, the design parameters ordered by decreasing relevance for the bending resonance frequency influence are:

	CAUTIONS:
1. Sheets thickness	It has a significant impact on the yield strength, weakening the structure;
2. Number of sheets	A greater number of sheets implies a more complex assembly which is better to be avoided for these high-precision applications;

3.	Edge carving shape of the plates	Excessive cutting from the edges weakens the torsional stiffness and if a hole in the middle of the plate is already present, a certain distance must be respected between the hole and the external cut;
4.	Spacing between the sheets	A larger swing arm is desirable to decrease frequency without affecting compliance, but it increases the overall dimensions of the suspension;
5.	Central hole diameter	It might be necessary to have a central hole for assembly accessibility, even if within a certain diameter there is no influence on the oscillation frequency;
6.	Constraint conditions	Greater oscillation symmetry for an even number of plates, with homogenization of the frequencies of the same type in the two directions but at the higher frequency of the two, using a single support for the two rivets between two plates. Little effect on uneven sheets number.

The final design will have to emerge from a trade-off between all these variables. In the studies on the influence of the design parameters, a simplified FEM model was used, which does not consider additional components necessary for assembly. These would influence the modal characteristics because moving masses and additional constraints are added.

For space applications it is preferable to use non-magnetic materials characterized by good thermal and electrical conductivity, such as the T6-7075 Aluminium alloy and the C17200 Beryllium-Copper alloy, which has superior mechanical properties compared to copper, which are the materials used for the proposed models.

Two design solutions are subsequently proposed, which share the same components but differs only in the number of metal sheets: one is a two-sheets suspension while the other has three sheets. I will call the first “Model-2S” and the second “Model-3S” where the “S” stands for “sheets”. The sheets are made of the Beryllium-Copper alloy, like the test mass, and are assembled together by riveting, through separating aluminium supports, of which the top and bottom ones connects respectively to the test mass and to the LIG-A frame, as shown in the following dimensioned CADs.

4.5.1 Model-2S

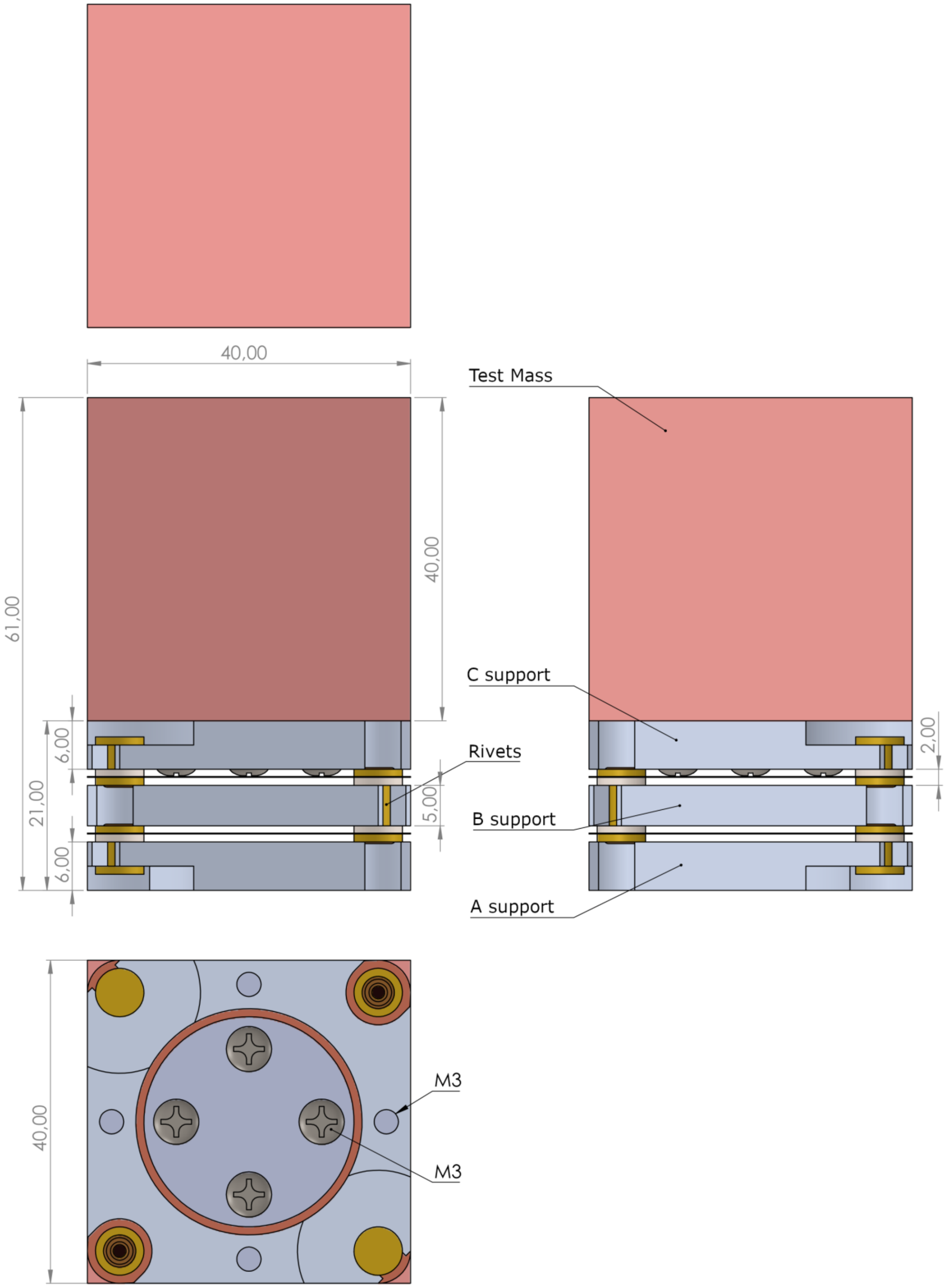

Fig. 4.67: Model-2S, upper, front, side and bottom view

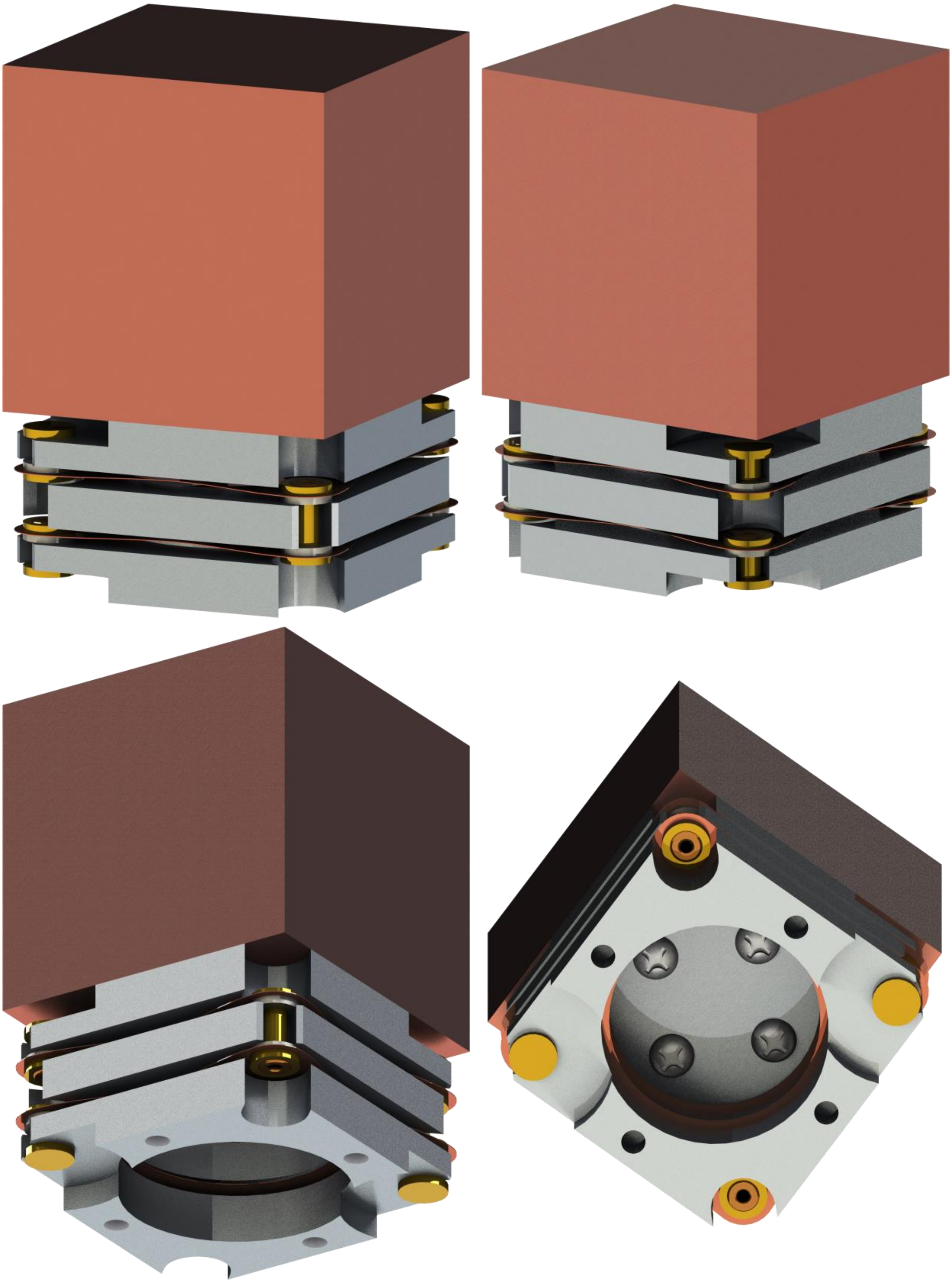

Fig. 4.68: Model-2S, renderings

4.5.2 Model-3S

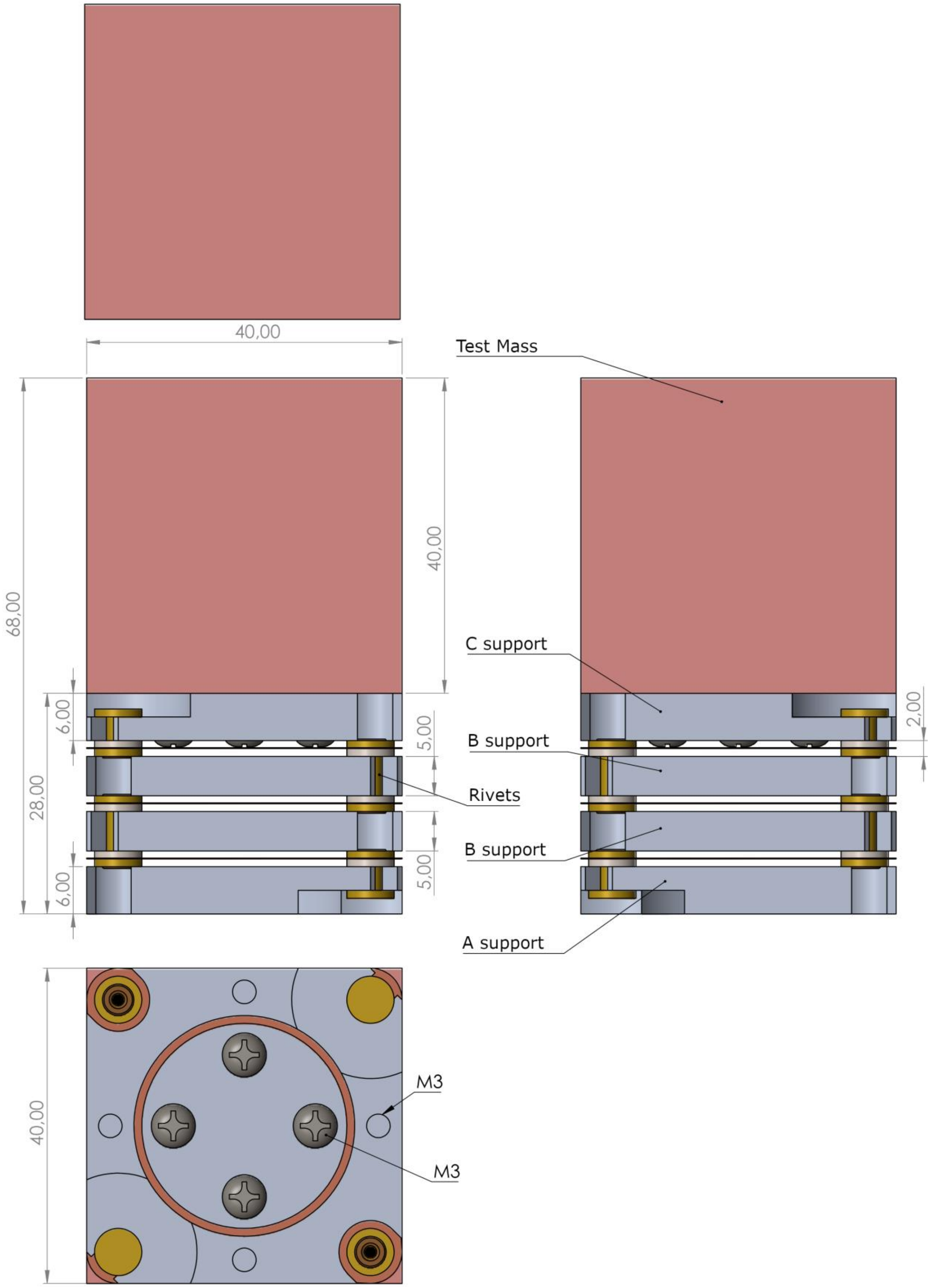

Fig. 4.69: Model-3S, upper, front, side and bottom views

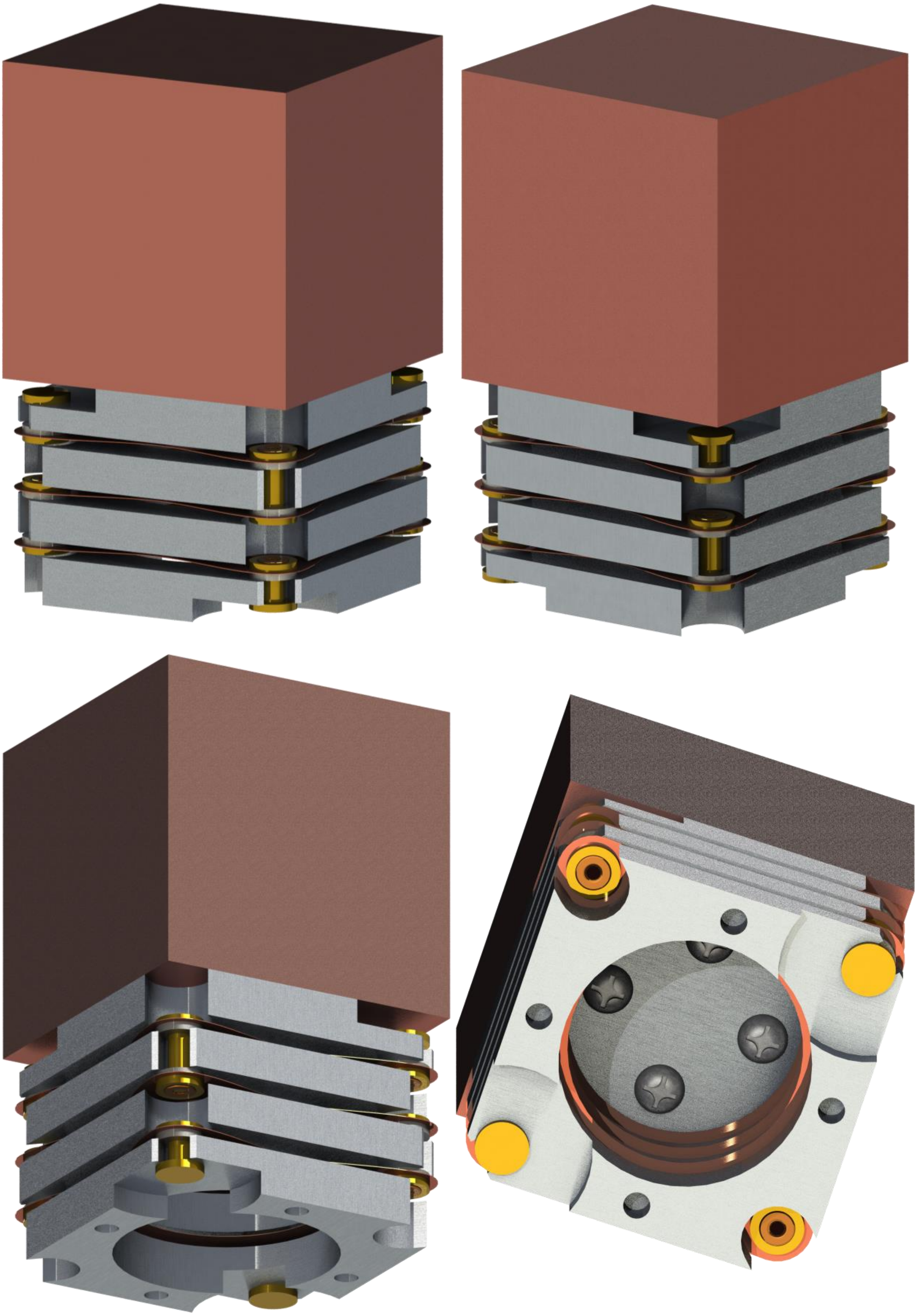

Fig. 4.70: Model-3S, renderings views

4.5.3 Components

Sheets

The shape of the plates is designed with a central hole that acts as an assembly access for joining the suspension to the test mass and with edge carvings made to decrease stiffness, the thickness will later be determined to be 0.05 mm. The size of the sides of the square from which the sheet is shaped is always 40 mm, as previous studied "Plate-A", in order to exploit all the available space according to the volume requirements. The rivets used have a footprint on the plates with a diameter of 6 mm as in the Plate-A model, in the same positions. I call this new sheet model "Plate-B" which differs from the one considered in the preliminary study of the previous chapters only by the central hole and the cut at the edges. The material chosen is the Beryllium-Copper alloy C17200, due to its good mechanical characteristics and thermal and electrical conductivity.

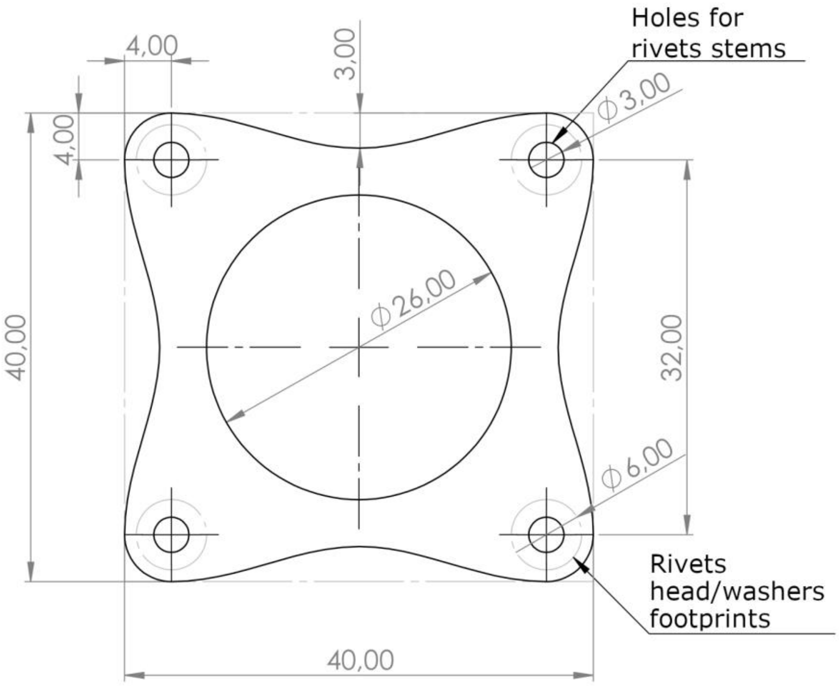

Fig. 4.71: Dimensioned drawing of the "Plate-B" model of the sheets used in the design proposals of the Model-2S and Model-3S suspensions. The footprint of the rivets are also shown at the vertices. Material: C17200 Beryllium-Copper alloy

Supports

The two suspension models have their sheets spaced by T6 7075 aluminium supports to house the rivets. These pieces are born as blocks with a square base and have a central hole for access to the assembly screws of the test mass and different housing cuts for the accommodation of two rivets in two diagonal vertices and clearance carvings to avoid interference with those of the other sheets in the other two vertices. Each support is separated from the other by 2 mm, in a neutral position. Aluminium was chosen for its thermal and electrical conductivity characteristics but above all for its low density, so as not to lead to significant unwanted resonance modes of the supports alone.

For both suspension models, three different types of aluminium supports are present:

- **A** support: suspension's bottom base, interface with the spacecraft frame via 4 screws, thickness of 6 mm;
- **B** support: sheets separators, there is one in the Model-2S model and there are two in the Model-3S, they are 5 mm thick;
- **C** support: interface with the test mass with 4 screws, thickness of 6 mm.

This solution provides a constraint condition of the type (a) discussed in Fig. 4.65 on page 102 in the study of the influence of the design parameters. Dimensioned drawings and CADs of the three types of support are reported in the following pages.

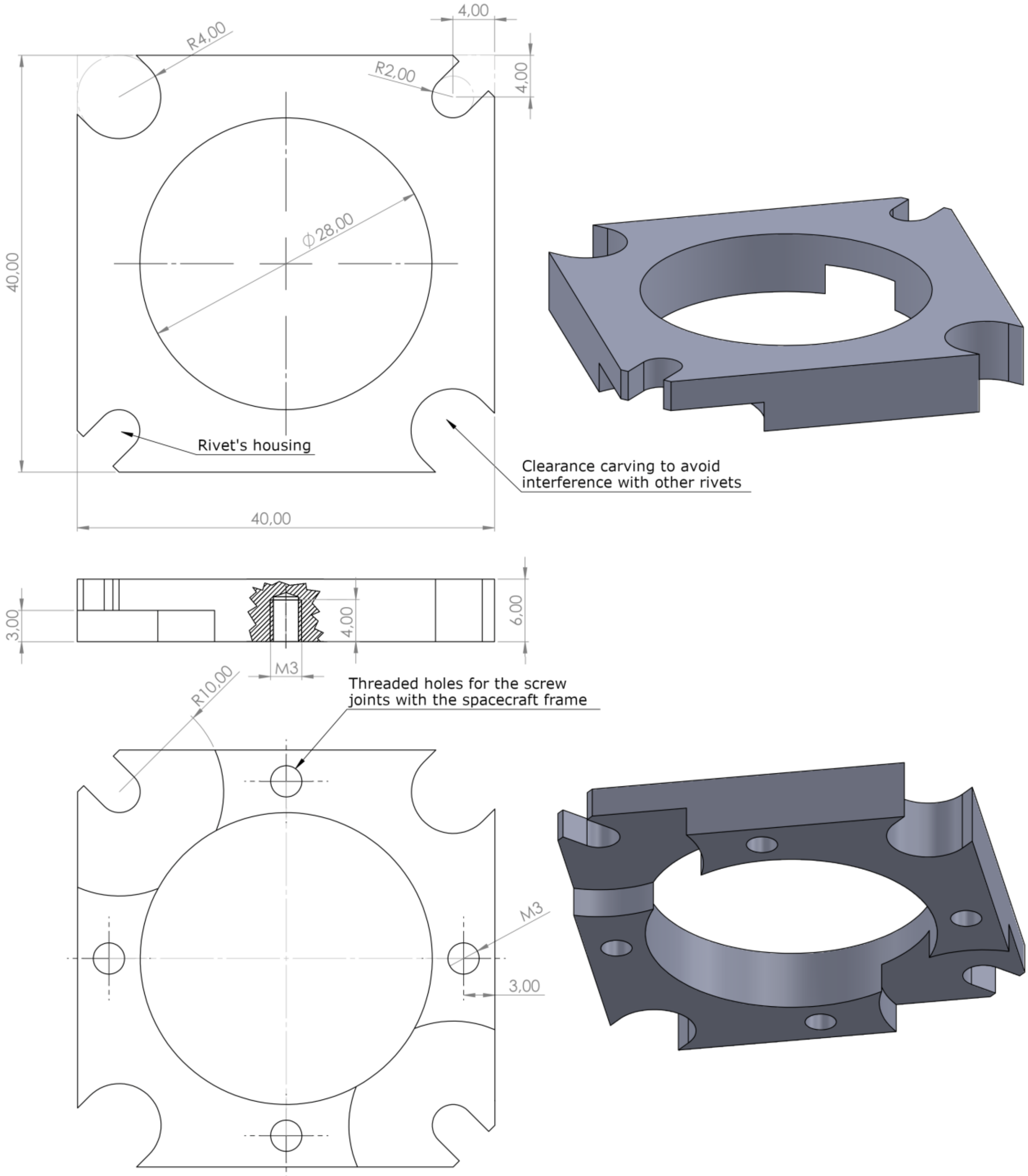

Fig. 4.72: A type support, T6 7075 aluminium alloy

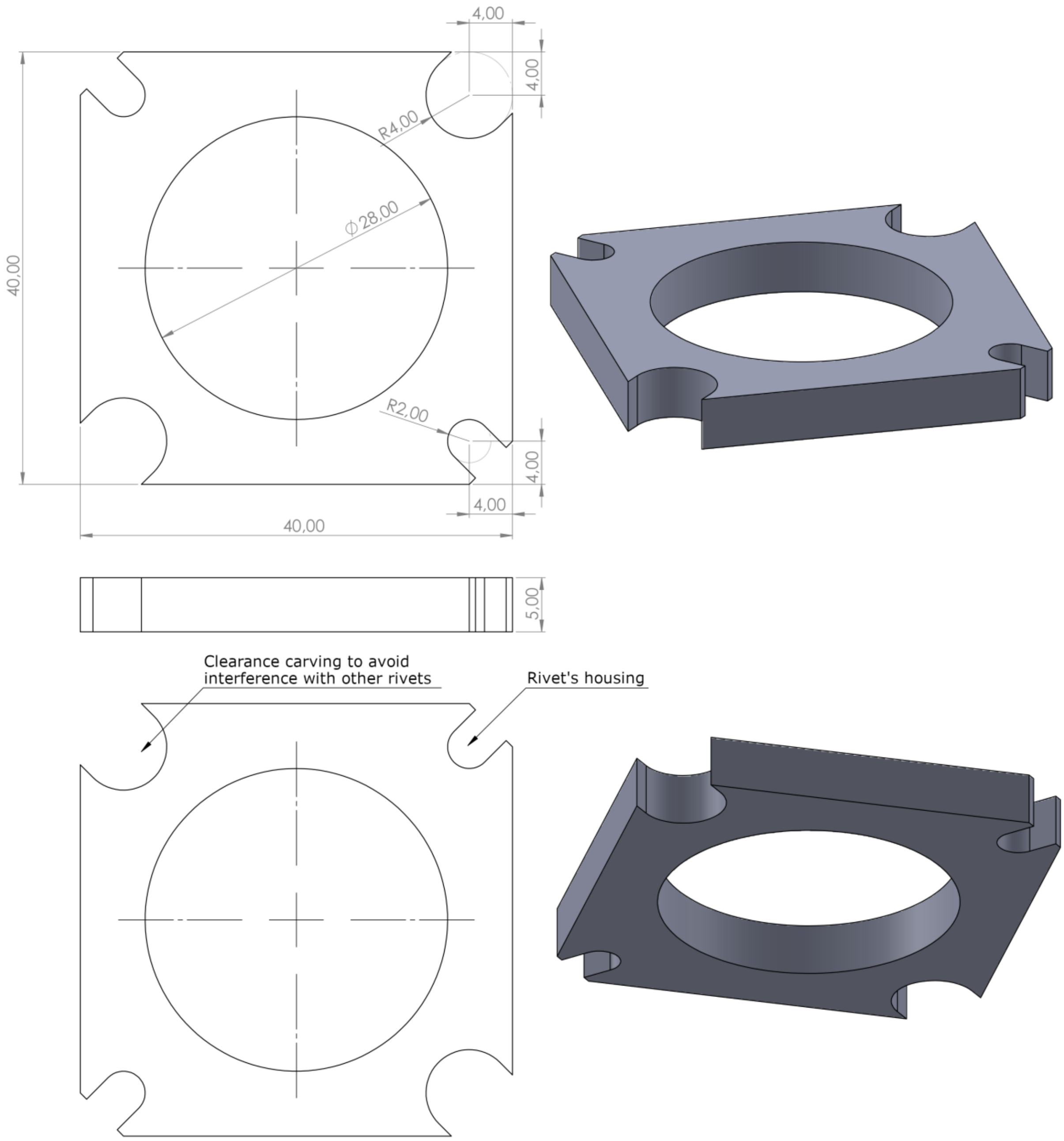

Fig. 4.73: B type support, T6 7075 aluminium alloy

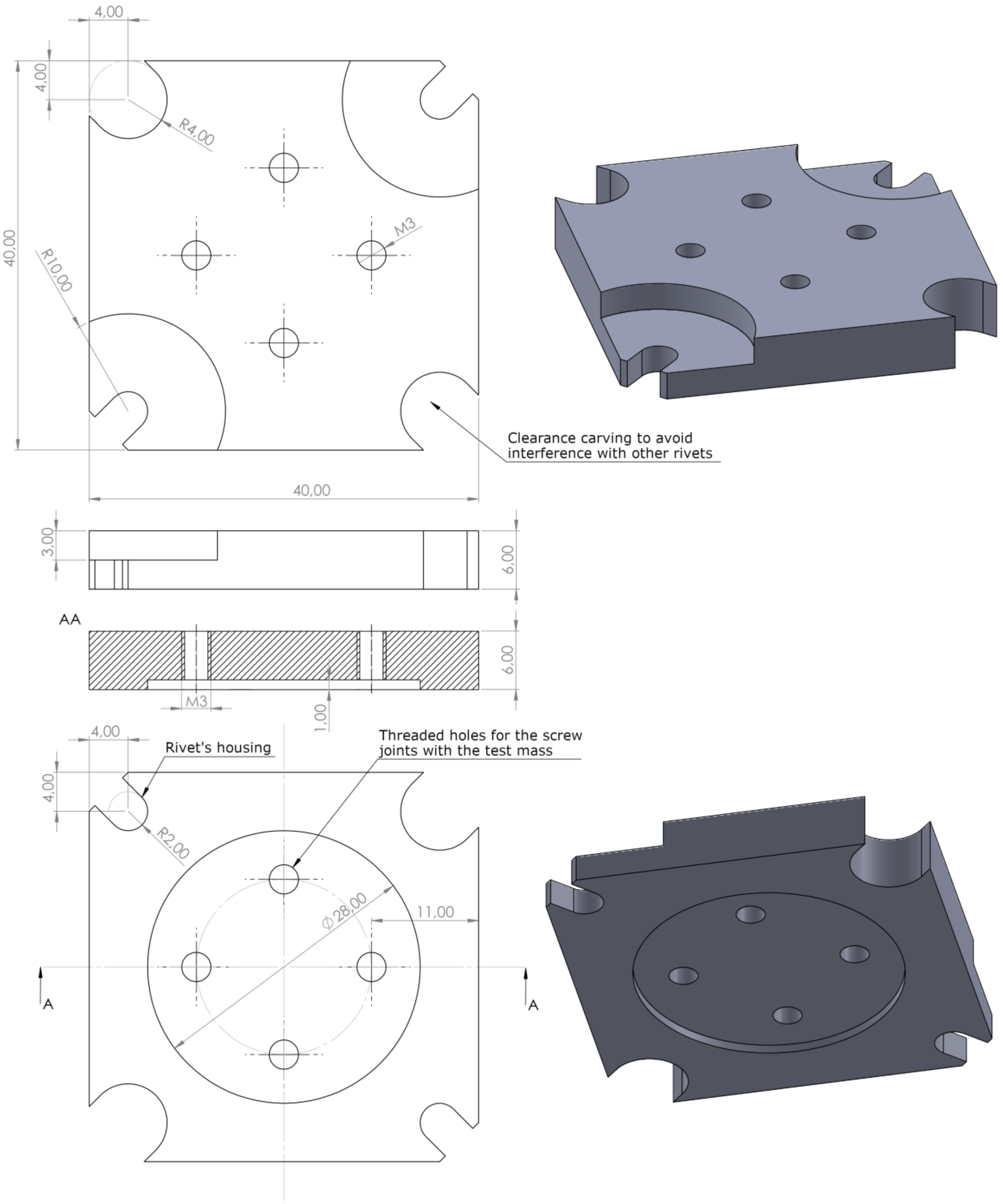

Clearance carving to avoid interference with other rivets

Rivet's housing

Threaded holes for the screw joints with the test mass

Fig. 4.74: C type support, T6 7075 aluminium alloy

Test mass

The test mass is, as in the case of the design proposal with an Helical spring, a cube of 40 mm of side length, it furthermore presents four threaded holes for housing of the screw joints with the aforementioned C type support (see Fig. 4.74 on page 113). The Beryllium-Copper C17200 alloy was the chosen material because of its good thermal and electrical conductivity characteristics and high density, as in the case of chapter 4.

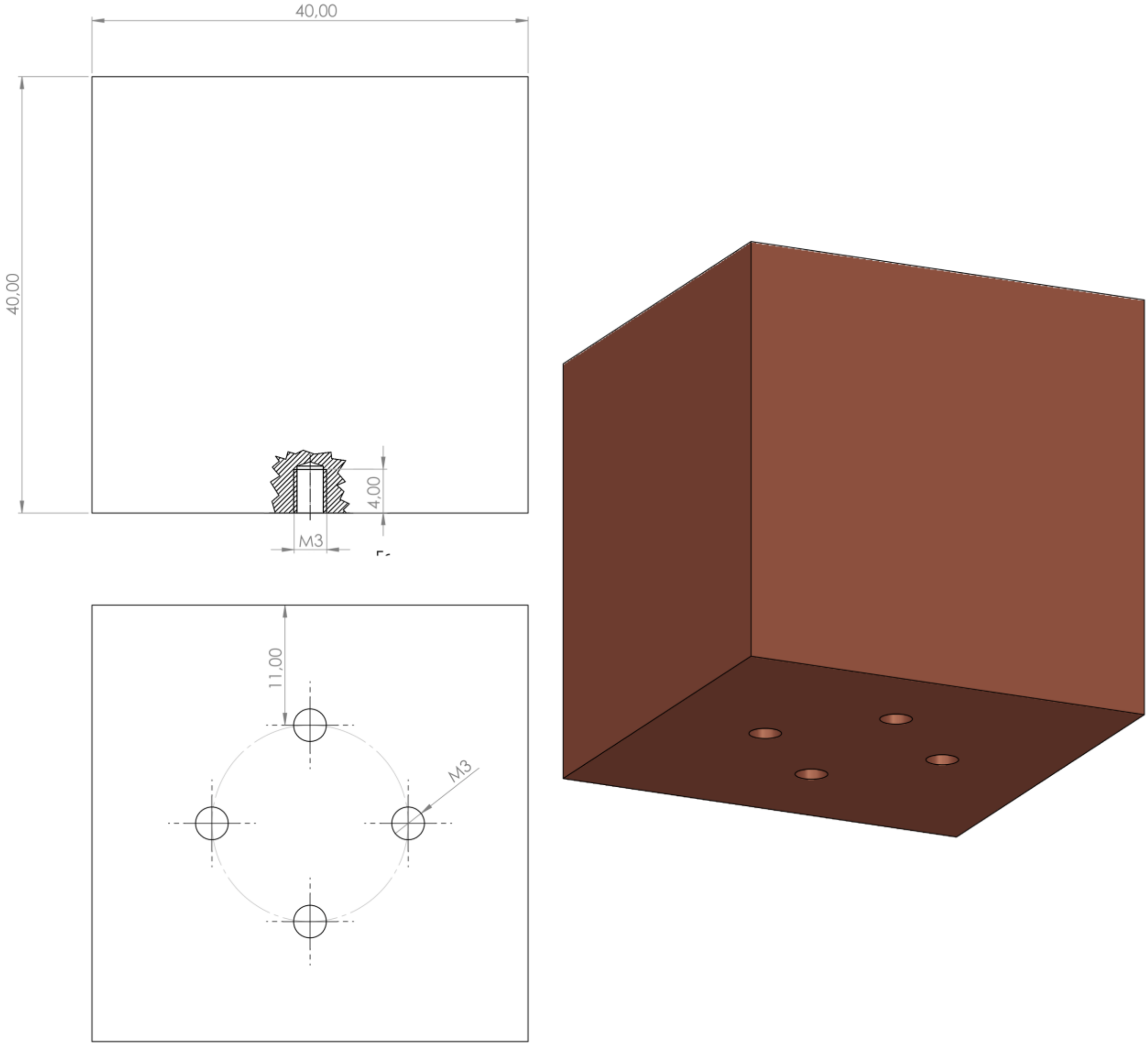

Fig. 4.75: Test mass, Beryllium-Copper C17200 alloy

Riveting

Taking as a reference case the construction of torque couplings of a similar concept to the elastic suspension in question (see Fig. 4.78 on page 116), riveting is selected for construction, joining the different sheets to each other and to the supports. The vertices of the plates are clamped between two washers of 6 mm of diameter and a of a thickness of 1 mm, one of which rests on the aluminium support and the other is fixed to the clinched end of the rivet. For the rivets attached to the base support (A) or to the interface support with the mass (C) the head is directly held on the aluminium supports. The stem of the rivets has a diameter of 3 mm and is 5 mm long for the separation supports (B) and instead is 3 mm for those at the A and C type supports. As in the real example reported in Fig. 4.78, they can be used materials such as brass or bronze for the rivets and aluminium for the support interface washers.

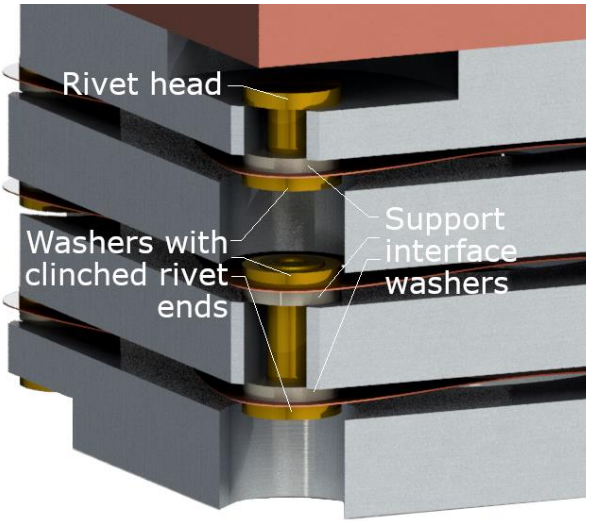

Fig. 4.76: Rendered detail of the riveting in the Model-3S case

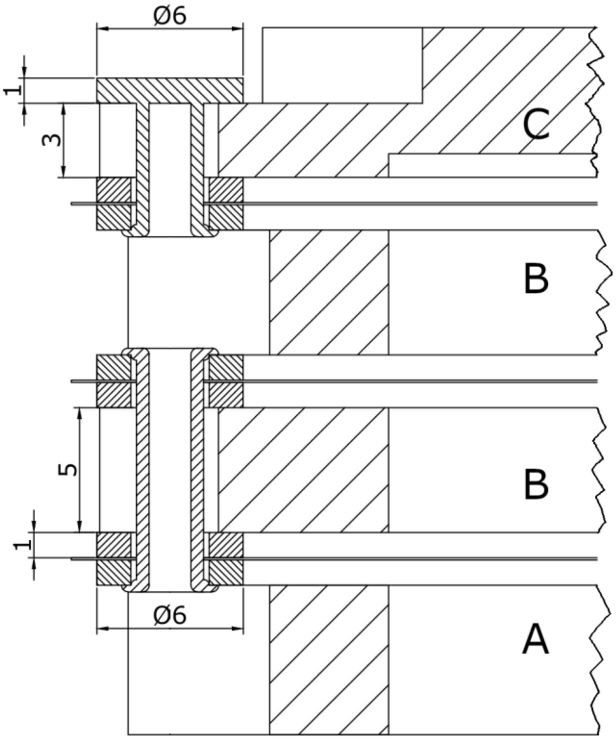

Fig. 4.77: Diagonal cross section of the Model-3S, detail on the different kinds of riveting involved

Fig. 4.78: Real assembly example for a sheets torque coupling

4.5.4 Modal Analysis – Sheets Thickness Variation

Once the two design proposals have been defined in their entirety, the corresponding finite element models can be built on the *MSC Patran* software, to conduct analyses with the *Nastran* solver. The models are not simplified as in the case of the previous conducted design parameters influence study, but instead they portray each element and their geometric, physical and mechanical characteristics, since an accurate modal analysis needs the knowledge of the mass distributions in space.

The C17200 Beryllium-Copper alloy cubic test mass is modelled with *Hex8* three-dimensional element type mesh, the T6 7075 aluminium supports and the brass rivets are modelled with *Tet4* three-dimensional elements instead, while the C17200 plates with *Tria3* two-dimensional elements. The different components are coupled together with *RBE2* type *MPCs*. The bottom base support is completely clamped, because fastened to the spacecraft frame structure. The properties of the isotropic materials set in the software are the following (see Tab. 3.7 on page 39 for references):

	Elastic Modulus [MPa]	**Poisson's Ratio**	**Density [t/mm^3]**
Al-7075	7170	0.33	2.81E-09
C17200	130000	0.30	8.25E-09
Brass	110000	0.30	8.50E-09

Tab. 4.19: Material properties of the FEM models for modal analysis of the proposed suspension designs Model-2S and Model-3S

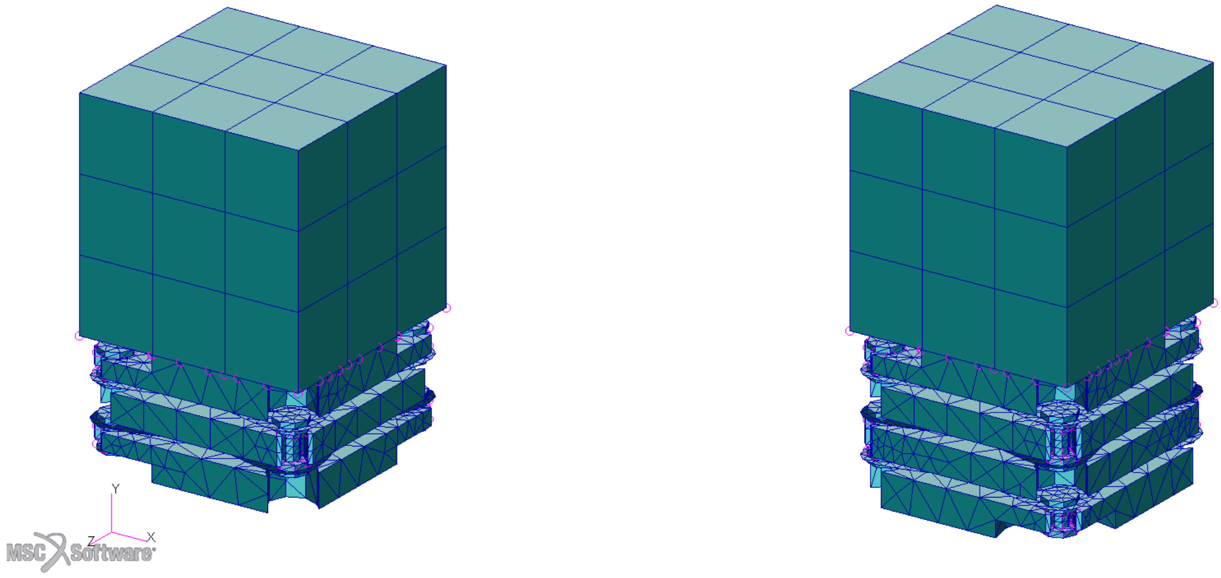

(a)

(b)

Fig. 4.79: FEM models of the two design proposals Model-2S (a) e Model-3S (b)

Since the FEM elements of the sheets are of the "shell" type, different analyses can be carried out as the thickness of the plates varies, by changing the mesh properties. The analyses consider a thickness spanning from 0.05 mm to 0.10 mm, which are in the range of commercially available C17200 alloy laminates. It will be concluded that the choice should fall on the smaller considered thickness, since even if it is the weakest, for the same strain it generate a lower stress relative to a thicker plate and therefore if the displacements from the neutral position are constrained within certain limits, it will not be able to reach the yield stress. In fact, it will be seen that yielding will not constitute a problem because the displacements are already limited by the interference between the mechanical parts and therefore, to avoid this phenomenon, the deviations of the test mass must already be restricted and within those limits the maximum tension reached in the sheets is negligible. Furthermore, as the thickness decreases, there is a notable decrease in the bending resonance frequency. Greater attention must be paid at these reduced thicknesses during construction and assembly to avoid unwanted distortions from the flat shape.

The results of the modal analyses for the two proposed elastic plate suspension models are reported on the following pages.

Model-2S

The results of the modal analyses show that for the two-plate model there are 6 main resonance modes, in fact from the seventh one onwards there is an increase in frequency of two orders of magnitude, so they are not of influence. In addition to the usual resonance modes seen in the previous analyses, this presents a mode of longitudinal oscillation of the aluminium support alone, marked below with an apostrophe, corresponding to the sixth resonance mode.

	Model-2S (Nastran SOL 103)					
Sheet thickness [mm]	**F_1 [Hz]** flex	**F_2 [Hz]** flex	**F_3 [Hz]** long	**F_4 [Hz]** tors_xz	**F_5 [Hz]** tors_zx	**F_6 [Hz]** long’
0.05	0.2582	0.2584	0.6692	4.128	4.414	8.335
0.07	0.4277	0.4280	1.108	6.827	7.309	13.76
0.08	0.5225	0.5229	1.354	8.334	8.928	16.78
0.10	0.7300	0.7306	1.892	11.63	12.47	23.38

Tab. 4.20: Modal analyses for different mass-spring systems of the Model-2S suspension type, as the thickness of the sheets changes

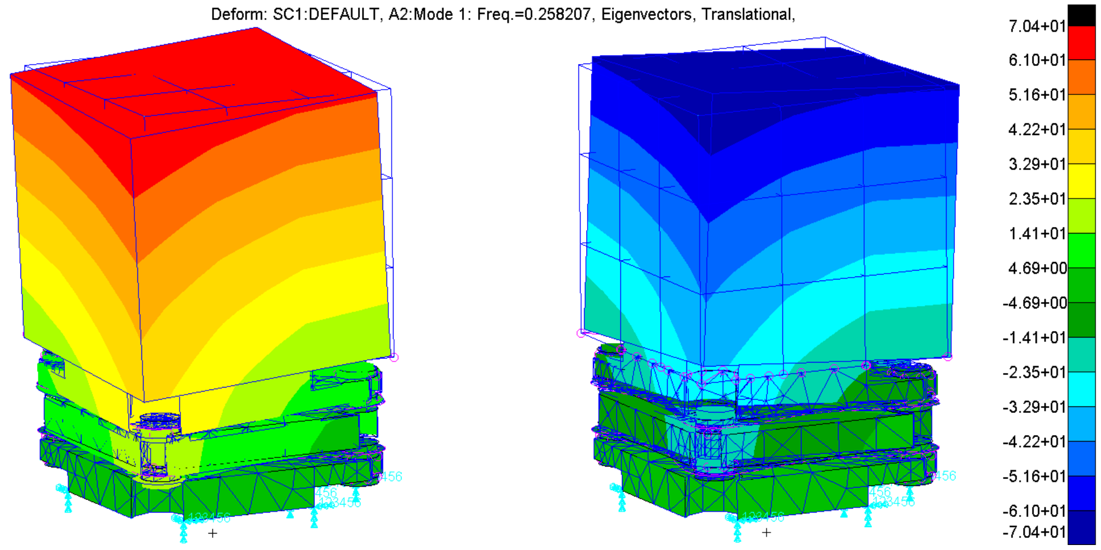

Fig. 4.80: F_1=0.258 Hz First bending resonance mode, Model-2S with 0.05 mm thick sheets

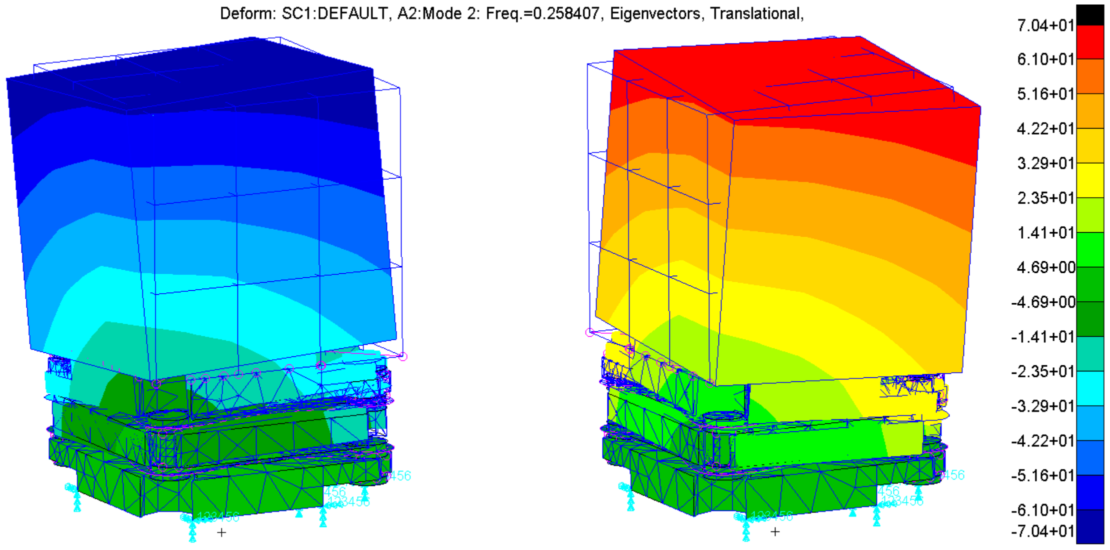

Fig. 4.81: F_2=0.258 Hz Second bending resonance mode, Model-2S with 0.05 mm thick sheets

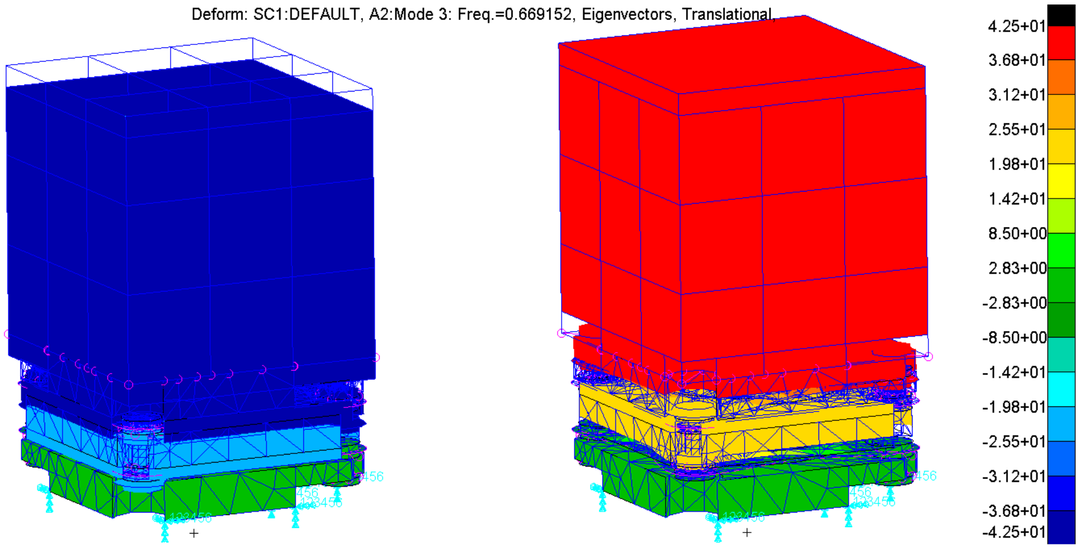

Fig. 4.82: F_3=0.669 Hz First longitudinal resonance mode, Model-2S with 0.05 mm thick sheets

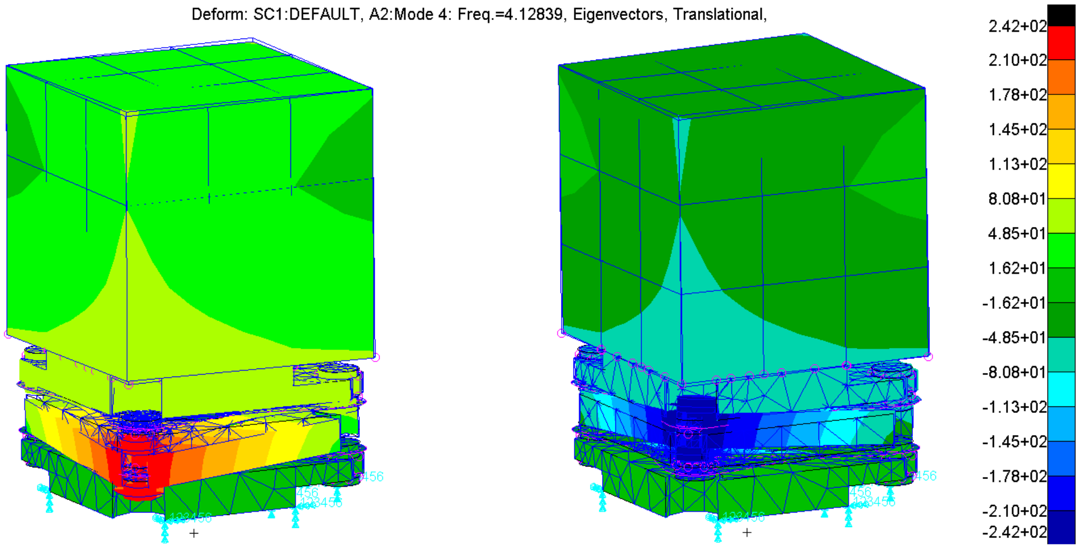

Fig. 4.83: F_4=4.13 Hz First side torsional mode, Model-2S with 0.05 mm thick sheets

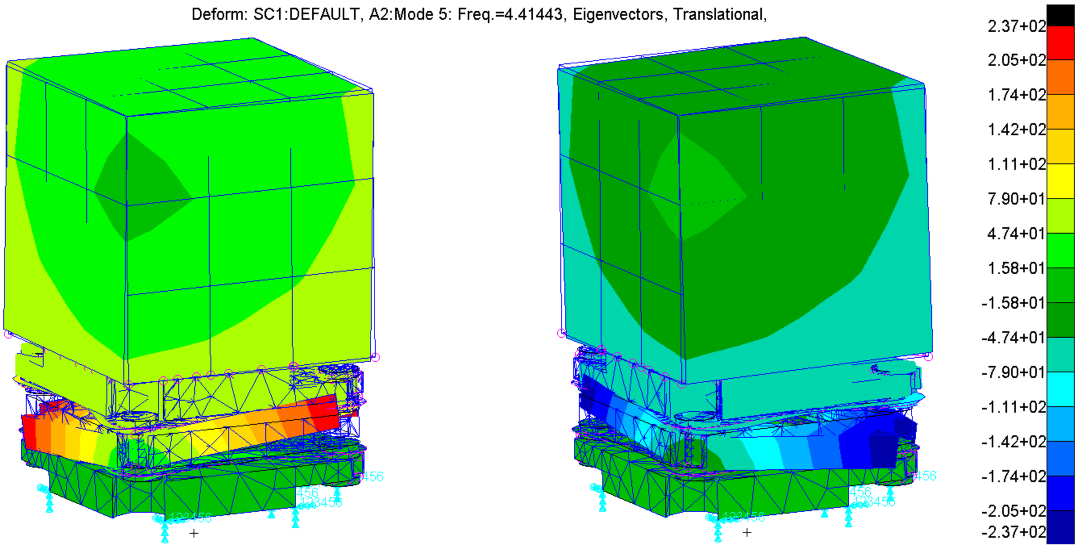

Fig. 4.84: F_5=4.41 Hz Second side torsional mode, Model-2S with 0.05 mm thick sheets

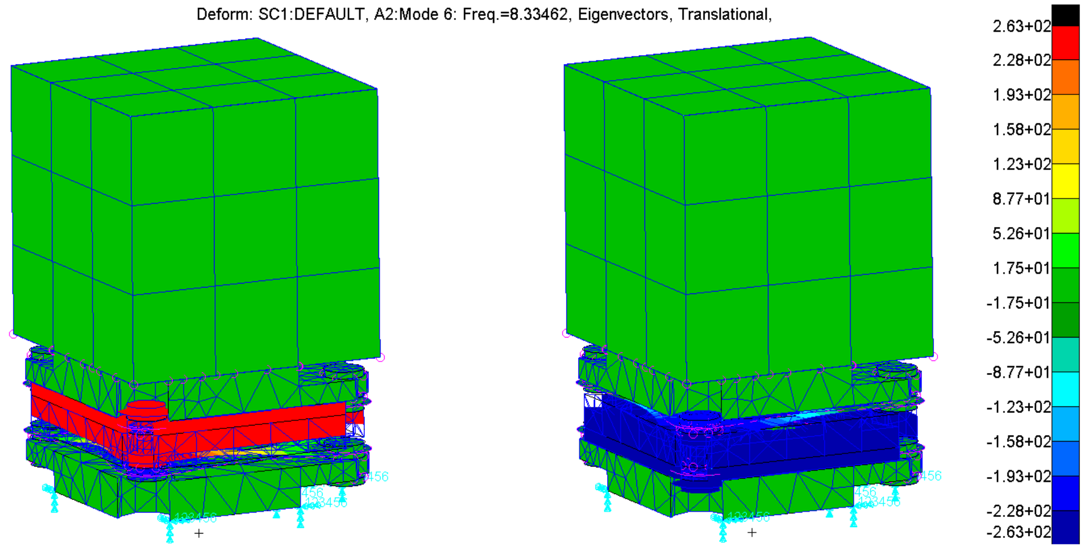

Fig. 4.85: F_6=8.33 Hz Second longitudinal resonance mode, Model-2S with 0.05 mm thick sheets

Model-3S

From the modal analyses it results that for the three-laminate model there are 9 main modes, subsequently there is a frequency increase of more than an order of magnitude, therefore the others are not influential. To the usual resonance modes seen in the previous analyses, four modes of oscillation of the aluminium supports are added, marked below with an apostrophe: two along the longitudinal y axis and the others of torsional oscillation in the normal directions.

Model-3S (Nastran SOL 103)

Sheet thick. [mm]	**F_1 [Hz]** flex	**F_2 [Hz]** flex	**F_3 [Hz]** long	**F_4 [Hz]** tors_xz	**F_5 [Hz]** tors_zx	**F_6 [Hz]** long’	**F_7 [Hz]** tors_xz’	**F_8 [Hz]** long_zx’	**F_9 [Hz]** long’’
0.05	0.1932	0.1932	0.5447	2.435	2.451	5.911	9.650	9.792	10.21
0.07	0.3200	0.3200	0.9023	4.033	4.063	9.782	16.04	16.30	16.91
0.08	0.3909	0.3909	1.102	4.925	4.962	11.93	19.56	19.88	20.63
0.10	0.5462	0.5462	1.540	6.876	6.928	16.61	27.24	27.70	28.74

Tab. 4.21: Modal analyses for different mass-spring systems of the Model-3S suspension type, as the thickness of the sheets changes

The following pages show the figures depicting the displacements plots of the first nine resonance modes are reported in the following pages, resulting from the FEM analyses for the Model-3S multiple sheets suspension.

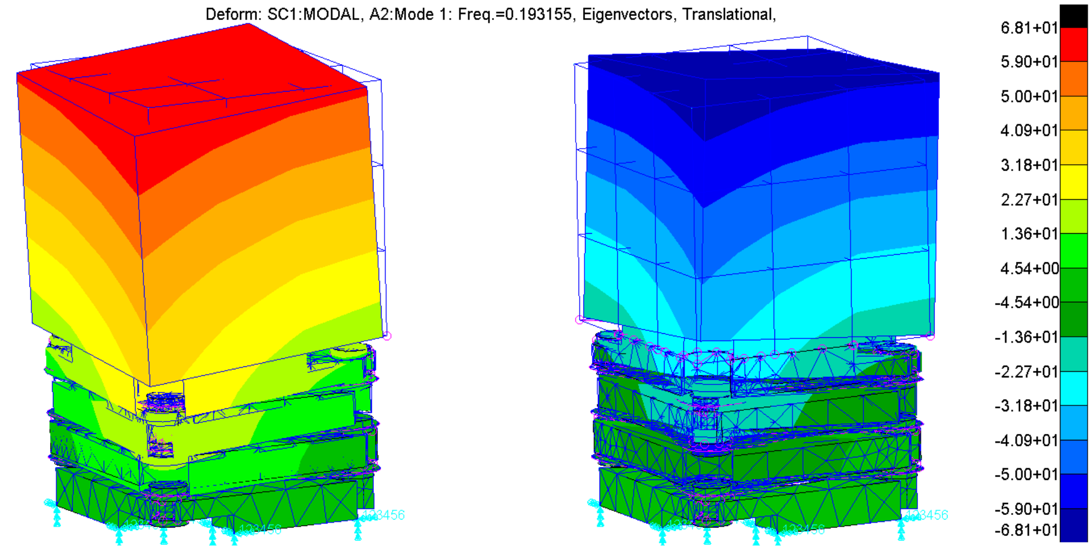

Fig. 4.86: F_1=0.193 Hz First bending resonance mode, Model-3S with 0.05 mm thick sheets

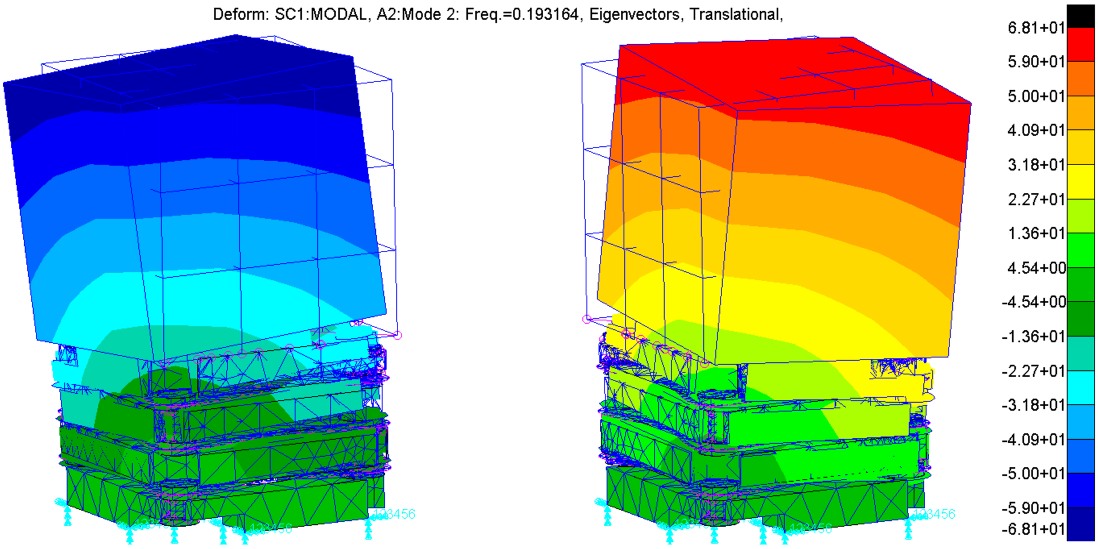

Fig. 4.87: F_2=0.193 Hz Second bending resonance mode, Model-3S with 0.05 mm thick sheets

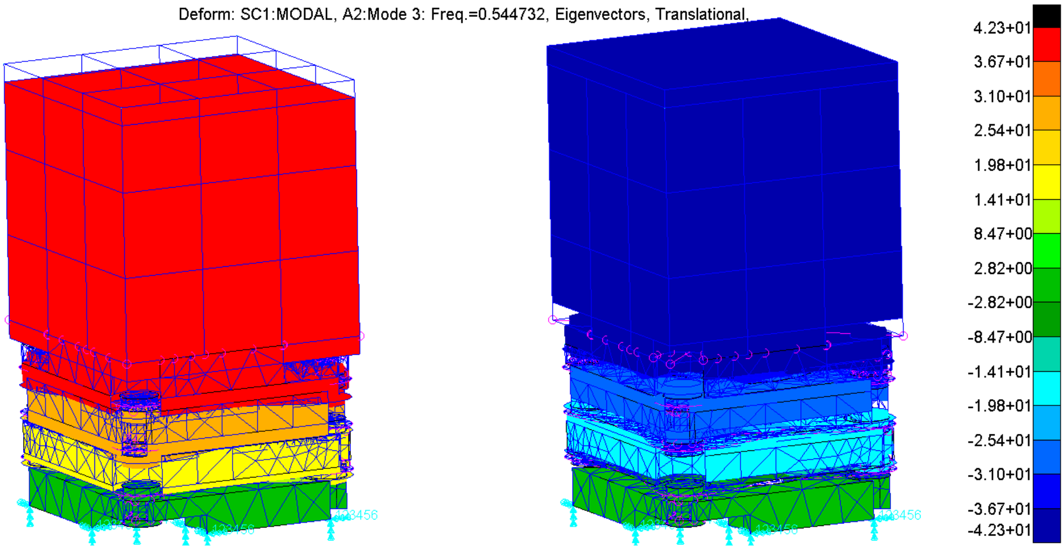

Fig. 4.88: F_3=0.545 Hz First longitudinal resonance mode, Model-3S with 0.05 mm thick sheets

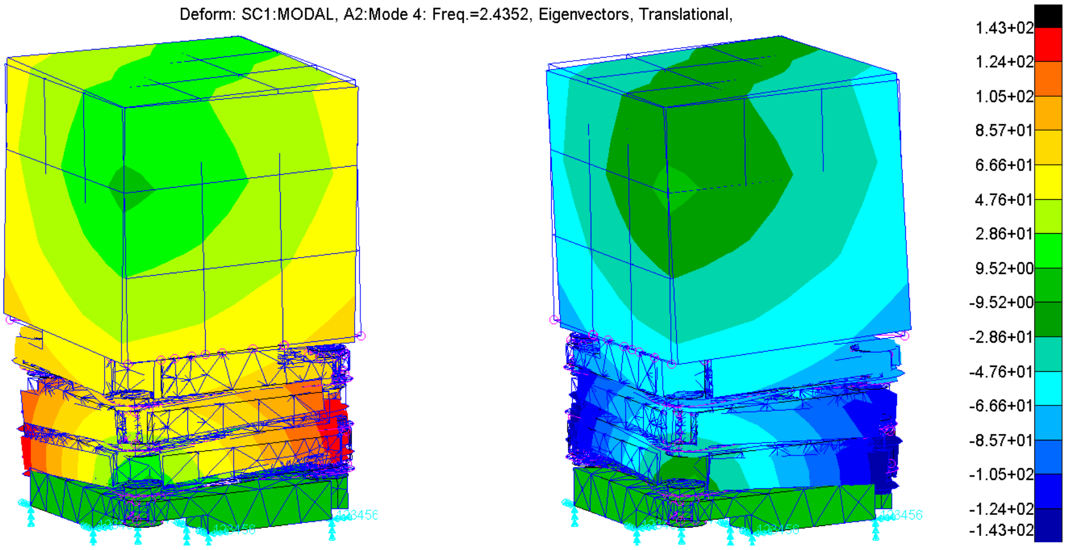

Fig. 4.89: F_4=2.44 Hz First side torsional resonance mode, Model-3S with 0.05 mm thick sheets

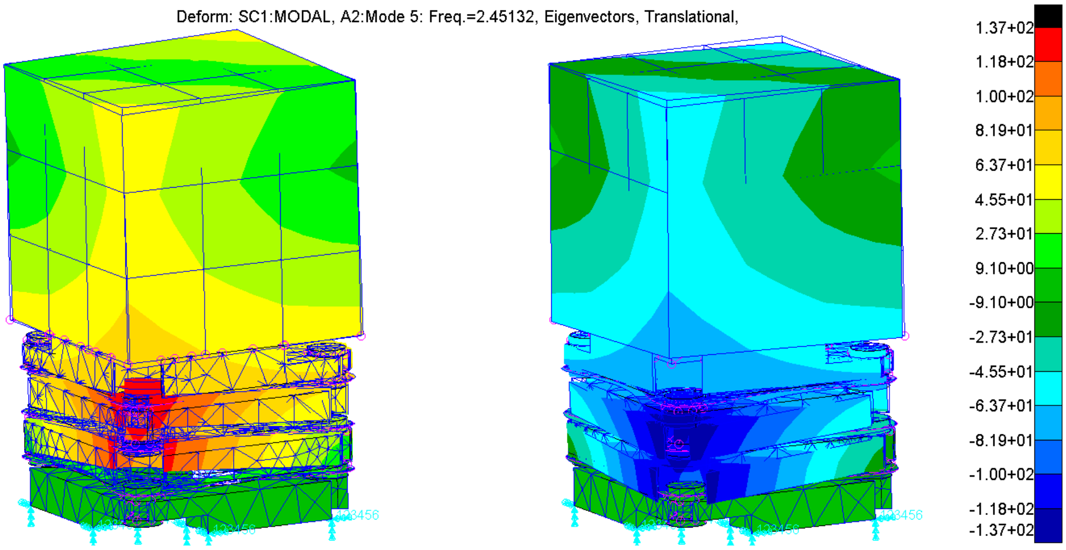

Fig. 4.90: F_5=2.45 Hz Second side torsional resonance mode, Model-3S with 0.05 mm thick sheets

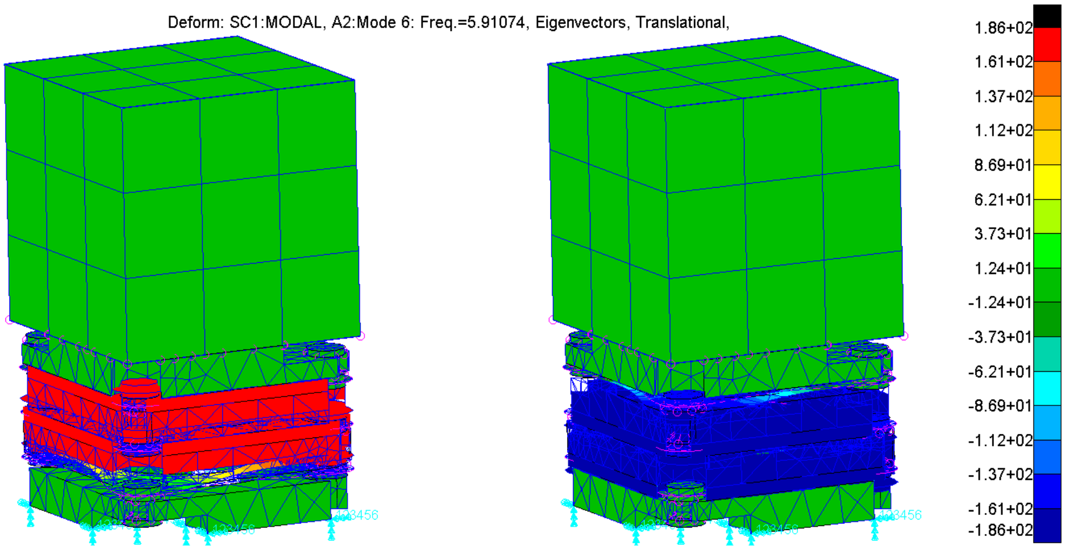

Fig. 4.91: F_6=5.91 Hz Second longitudinal resonance mode, Model-3S with 0.05 mm thick sheets

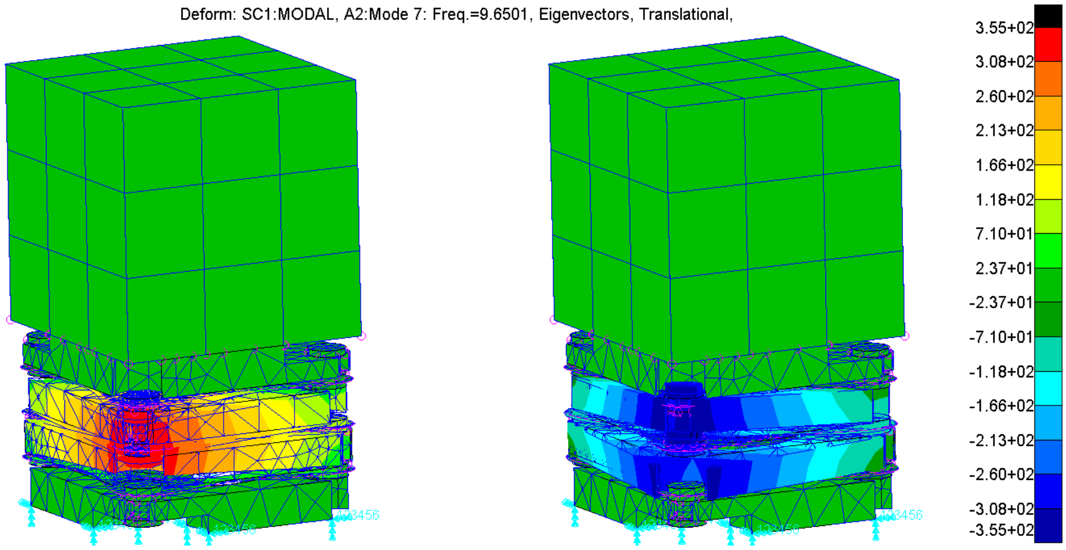

Fig. 4.92: F_7=9.65 Hz Third side torsional resonance mode, Model-3S with 0.05 mm thick sheets

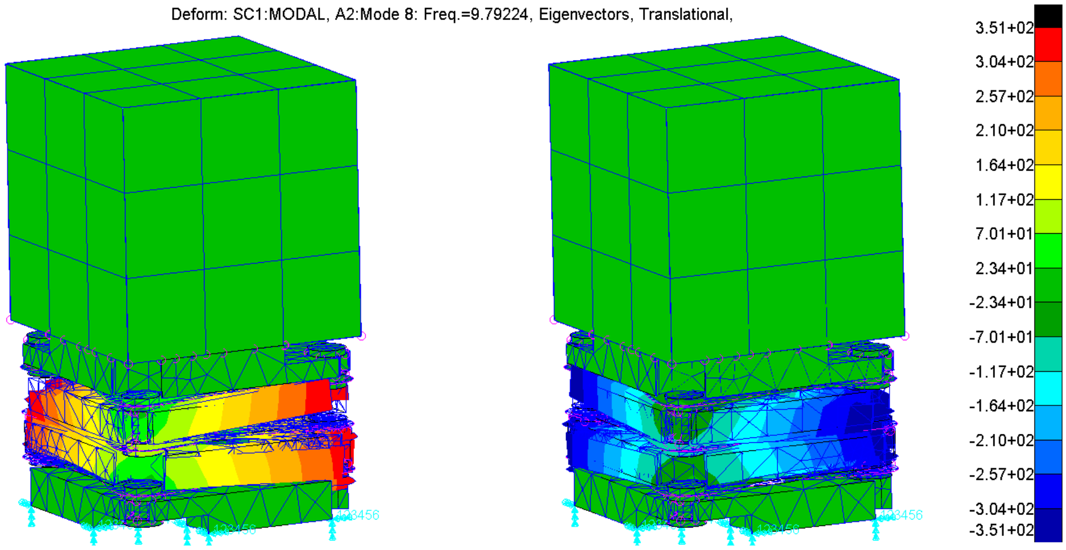

Fig. 4.93: F_8=9.79 Hz Fourth side torsional resonance mode, Model-3S with 0.05 mm thick sheets

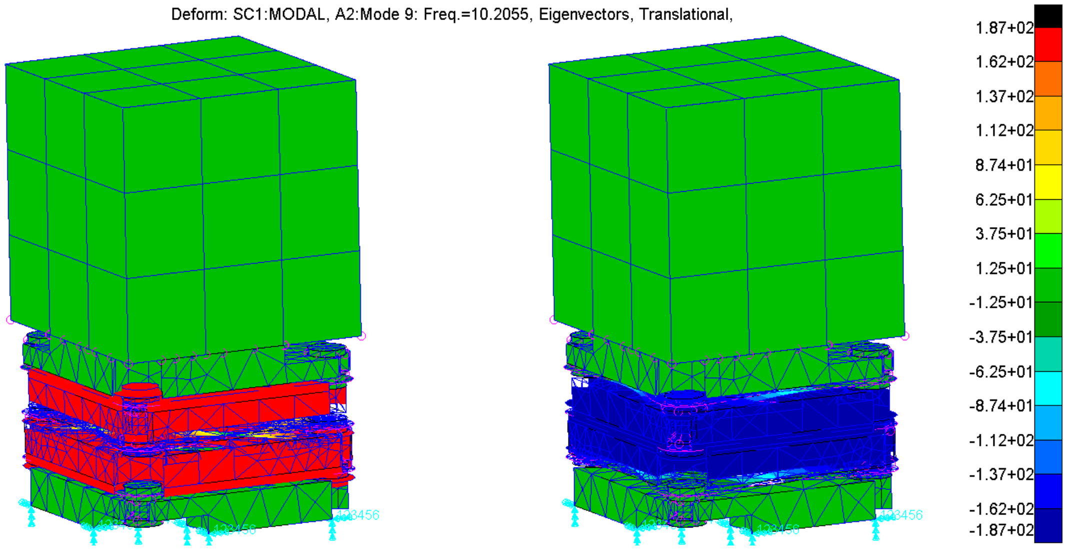

Fig. 4.94: F_9=10.21 Hz Third longitudinal resonance mode, Model-3S with 0.05 mm thick sheets

4.5.5 Static Analysis – Displacements Limits Determination

The allowable displacements of the elastic suspension components in response to an acceleration in a generic direction must be limited for two reasons:

- To avoid yield in the metal elastic sheets
- To avoid mechanical interference between components

To know what the extents of the displacement limits that will have to be set with mechanical stops to avoid these two phenomena, linear static analyses (Nastran SOL 101) will have to be carried out with the same FEM model used for the previous modal analyses, adding to the boundary conditions, in addition to the clamping at the bottom base, an inertial load to simulate the response of the elastic suspension to an acceleration.

The logical process I adopted to find a solution is the following. I first simulated the most critical cases of interference in the different directions with an acceleration in those same directions to find both the corresponding displacements of the pieces during the interference and to find the stress in the sheets for these conditions. For the same displacement and therefore deformation, a greater stress is obtained for a greater sheet thickness. Therefore, to get a conservative result, these static analyses at the interference will be performed for the most critical case between those considered, thus for a thickness of 0.1 mm. If the maximum tension reached in the plates in correspondence with the interference is less than the yield stress of the material then the problem of yielding can be excluded regardless, since a greater displacement and therefore a greater stress than that corresponding the interference is unacceptable. If this applies to the sheet with the larger thickness (0.1 mm) than those proposed, then it must also apply to all the smaller thicknesses.

From different simulations it was seen that the interference always begins when the edge of the sheet touches the edge of the upper or lower aluminium support. The simulated acceleration directions, also shown in the following figure, were:

- Side direction (x axis of the FEM model)
- Diagonal direction (diagonal between the x and z of the FEM model)
- Longitudinal direction (y axis of the FEM model)

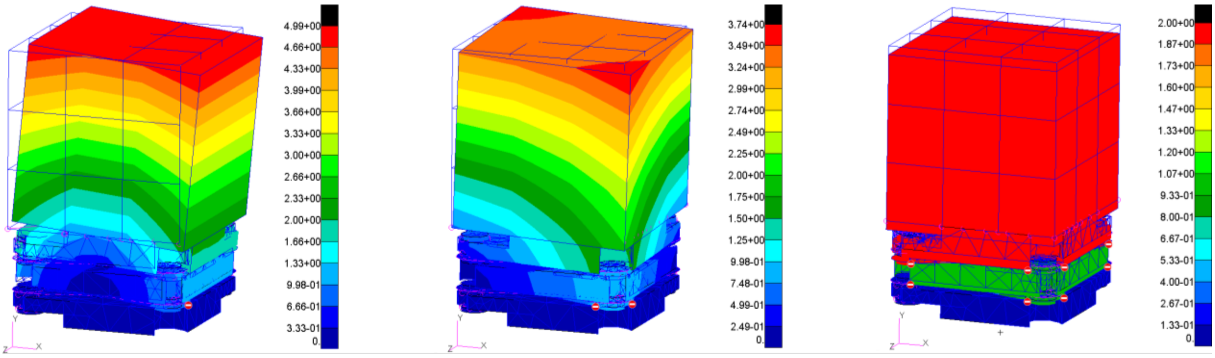

Fig. 4.95: Displacements plot [mm] for the Model-2S suspension in correspondence with starting interference phenomena conditions for the three lateral, diagonal and longitudinal directions. Interference principles are marked with red and white symbols

From the results we obtain that for both the Model-2S and Model-3S suspension models, the test mass displacement is limited first by the interference in the lateral diagonal direction in the x, z and $+y$ directions while the deviation in the $-y$ direction is limited first due of interference in the longitudinal direction, which also limits the displacement of the aluminium supports. The maximum allowed displacements in the different cases, corresponding to the interferences, are reported below.

	Δx [mm]	Δy [mm]	Δz [mm]
Model-2S	±2.31	+1.82	±2.31
Model-3S	±3.93	+2.86	±3.93

Tab. 4.22: Test mass maximum displacements corresponding the start of the interference phenomenon alongside the bending oscillation

	Δy [mm]
Model-2S	-2.00
Model-3S	-3.00

Tab. 4.23: Test mass maximum displacements corresponding the start of the interference phenomenon alongside the longitudinal oscillation

	Δy [mm]
Model-2S	±1.00
Model-3S	±1.00

Tab. 4.24: Aluminium supports maximum displacements corresponding the start of the interference phenomenon alongside the longitudinal oscillation.

	Sheets thickness [mm]	σ_{max} **[MPa]**
Model-2S	0.1	0.017
Model-3S	0.1	0.016

Tab. 4.25: Maximum stress achieved in the sheets in correspondence of displacements that induce the interference phenomena, Nastran SOL 101.

It turns out that even if we were to reach interferences and therefore the maximum permitted displacements, for a sheet thickness of 0.1 mm a maximum stress of the order of one hundredth of MPa would be reached in correspondence of the rivets' footprints, and therefore a negligible tensions compared to the 965-1205 MPa yield stress of the Beryllium-Copper alloy C17200 [12] of which the sheets are made. This means that the displacements will be limited only by the interference phenomenon and that the yield problem can be ignored if these deviations are respected.

A system for restricting the movements of the components consisting of a containment cage for the test mass and stops for the floating supports will have to allow for smaller deviations than the limits obtained before. The test mass (40 × 40 × 40 mm) containment box, for example, can have the following dimensions for the two design proposals:

	x **[mm]**	y **[mm]**	z **[mm]**
Model-2S	42	42	42
Model-3S	45	45	45

Tab. 4.26: Proposed dimensions for the test mass containment cage

These performed static analyses make use of a linear solution, Nastran SOL 101, which is only valid within a certain range of strains/torque applied, as seen in the preliminary FEM study (see Fig. 4.10 on page 61). In that context it was found that for a single sheet the linear and non-linear results coincided up to a torque of approximately 0.3 Nmm.

If we wanted to make a broad estimate to verify whether the results obtained with a linear solution are valid, it can be considered that during the bending flex, a torque is applied to the suspension, equal to the product of the test mass (0.53 kg), the acceleration and the rotation lever arm of the bending mode. The centre of rotation for a two and three sheets elastic suspension was previously calculated to be equal to be approximately at 8% and 14% of the distance between the bottom plate and the centre of the test mass (see Tab. 4.15 on page 96). Therefore for the Model-2S and Model-3S suspensions, a bending lever arm of about 31 mm and 35 mm respectively can be estimated. Assuming that, as in the lumped parameter model, the torque is equally divided between the sheets, the following equations can be written to find the limit lateral accelerations for which the linear solution is valid, for the two cases:

$$2 \cdot 0.5\ Nmm = 31\ mm \cdot 0.53\ kg \cdot a_{lim\_M2S}$$

$$3 \cdot 0.5\ Nmm = 35\ mm \cdot 0.53\ kg \cdot a_{lim\_M3S}$$

$$a_{lim\_M2S} = 0.061\ \frac{m}{s^2}$$

$$a_{lim\_M2S} = 0.081\ \frac{m}{s^2}$$

When the displacements corresponding to interference phenomenon start reported in Tab. 4.22 were evaluated, the FEM analysis was carried out with a lateral acceleration in the diagonal direction equal to 0.056 m/s^2 for the Model-2S and 0.052 m/s^2 for the Model-3S, therefore within the limit values of validity of the linear solution. The maximum value corresponding to the interference was considered to be conservative, but with the limits dictated by a containment cage we can safely say that the results fall within the range of validity of the linear solution.

It can be concluded that the FEM models for the Model-2S and Model-3S project proposals adopted in this paragraph and subsequently the linear static analyses carried out by setting an acceleration in a generic direction, could be used accurately to predict the behaviour of the suspension and then establish an acceleration-displacement relationship, useful for the accelerometer calibration, given that the LIG-A interferometric system measures the displacements of the test mass to compute the acceleration of the spacecraft.

CONCLUSION

The design of an elastic suspension for the test mass of the LIG-A high-precision accelerometer for space applications, that is the work presented in this thesis, was carried out with the purpose of meeting the project requirements regarding the instrument acceleration reading noise, degrees of freedom and dimensions. In particular, the suspension had to be free to move through all 6 degrees of freedom in space and this was achieved by proposing suspensions with a helical spring obtained from a single machined piece, the so called HELI-CAL® type, or with a solution that exploits the bending of a suspension with multiple parallel sheets mutually attached to the vertices in an alternating manner. The proposed design models are one of the first type, called Helical-C and two of the second, called Model-2S and Model-3S with 2 and 3 metal sheets respectively. For the mass-spring system of the accelerometer it was desired that the first resonance modes were to be bending and then longitudinal modes and that it should be provided with an adequate torsional stiffness. The sheets and Helical spring suspension solutions behave similarly at the modal level, respecting the aforementioned requirements, but the proposed multiple sheets suspension models guarantee a torsional stiffness almost two orders of magnitude greater than the Helical case and also a lower bending stiffness, resulting into more desirable performance. The main oscillation frequency should have been, according to the requirement, less than 1 Hz and preferably of the order of a tenth of an Hz. For all project proposals this requirement is satisfied, in particular the main resonance mode, which is the bending mode, frequencies obtained were of: 0.416 Hz for the Helical-C; 0.258 Hz for the Model-2S; 0.193 Hz for the Model-3S. The proposed solutions have similar dimensions, falling within the imposed box limit of 40 × 40 × 70 mm. In particular, both the Helical-C model and the Model-3S have dimensions of 40 × 40 × 68 mm, while the Model-2S has dimensions of 40 × 40 × 61 mm and is therefore the best in terms of size - performance ratio. From the FEM analyses of the models it emerged that, if displacements are appropriately constrained to avoid interference between mechanical components which would damage the flexible elements, stresses well below the yield threshold are obtained. The gaps proposed for the movements are of the order of millimetres, therefore much larger than those of the capacitive accelerometers currently used in the same applications, thus allowing less noise in the output readings.

The next proposed phase for the perpetuation of the work is to create prototypes of the proposed project models, with appropriate containment cages whose limits are known but whose construction details have not been explored in depth yet, in order to verify the validity of the numerical obtained results. A development of empirical research on prototypes could also evaluate the quality of the materials chosen for the construction of the suspensions. In all the proposed project models the same Beryllium-Copper alloy cubic test mass of 40 mm side length is used due to its good thermal and electrical conduction characteristics and mechanical resistance. In fact, the same material is also used for the metal sheets of the Model-2C and Model-3C, while the Helical-C suspension is proposed to be made in the Titanium Beta alloy. The multiple sheets suspensions also feature 7075 T6 aluminium spacers for rivet support. These characteristics can lead to critical issues that will have to be evaluated in the subsequent phases. In fact, for the Helical solution, which is obtained by machining from a single metal block, that should therefore provide better thermal noise characteristics, the criticality emerges however for the same reason: the geometry and the material, place the processing technology at its limits. As regards the proposed multiple sheets suspension solutions, the presence of interfaces between different materials and the assembly with rivets, which is therefore more complex due to the greater number of mechanical components, can lead to critical issues of thermal noise and thermal deformation.

A significant result concerns the applicability of the used methods, such as the lumped parameters analogy of the bending resonance mode with an original numerical-analytical method developed by me, or the results of the suspension design parameters influence study, especially in the case of the sheets suspension, which could find applications of general interest in the field of mechanics.

ACKNOWLEDGEMENTS

The most important acknowledgement I must devote to is to my parents, who allowed me to pursue my dreams and complete my university career, they have always supported me unconditionally in the best and worst moments and my ultimate goal is to make them proud.

For this master's degree thesis work I have to thank my institute supervisor, Doc. Marco Pisani of INRiM, who has always followed me, guided me and proposed brilliant ideas and solutions. Above all I am grateful for him having believed in me. I really appreciated his availability, his professionalism and his passion and I am indebted to him for everything I learned which allowed me to grow professionally and personally.

This thesis would not have been possible without the unrepeatable opportunity of being able to work on such an important project for INRiM and ESA which was allowed to me by the academic supervisor, Prof. Angelo Lerro, to whom I therefore owe special thanks and to whom I am grateful for the availability and guidance provided.

REFERENCES

[1] Rindler, W. (2013). *Essential relativity: Special General, and Cosmological.* Springer.

[2] Corke, P. (2017). *Robotics, vision and control: Fundamental Algorithms In MATLAB® Second, Completely Revised, Extended And Updated Edition.* Springer.

[3] Pisani, M. Z. (2021). *LIG-A: Laser Interferometry Gauge & Accelerometer. Final Review.* ESA AO/1-8876/17/NL/CRS ITI type B Proposal No. 1000019244-8000014585-1 ESA CN 4000125653.

[4] Josselin, et al. (1999). *Capacitive detection scheme for space accelerometers applications.* Sensors and Actuators A: Physical.

[5] Santoli, F. et al. (2020). ISA, a High Sensitivity Accelerometer. *Space Science Reviews*, 216:145.

[6] Università di Pisa, Dipartimento di Fisica "E. Fermi" & INRIM, Torino. (2020). *LIG-A: Laser Interferometry Gauge & Accelerometer, Proposal: Technical Part.* ESA AO/1-8876/17/NL/CRS.

[7] Nobili A. M., Pisani M., Zucco M., Pegna R. (2021). LIG-A Laser Interferometry Gauge & Accelerometer. *Space Engineering & Technology Final Presentation Days.* INRiM, Istituto Nazionale di Ricerca Metrologica, Torino. Dipartimento di Fisica "E. Fermi", Università di Pisa & INFN, Pisa.

[8] Pisani M. (2023) *LIG-A-CUBE Requirements Review.* INRiM, 14th August ESA Meeting.

[9] MONDIAL S.p.A. (2023). HELICAL. From https://www.mondial.it/euronet/contenuti/image/thumb/HELICAL.pdf

[10] NeoNickel. (s.d.). *Alloy 15-5 Datasheet.* From https://www.neonickel.com/generate-alloy-pdf/?id=12106

[11] Anchor Harvey. (s.d.). *Aluminum 7075 Datasheet.* From https://www.anchorharvey.com/media/fiahg3e0/anchorharvey-aluminum7075-datasheet.pdf

[12] AZO materials. (2012). *Beryllium Copper UNS C17200.* From https://www.azom.com/article.aspx?ArticleID=6326

[13] AZO materials. (2013). *Grade Ti 15V 3Cr 3Al 3Sn Alloy (UNS R58153).* From https://www.azom.com/article.aspx?ArticleID=9396

[14] Gutekunst Formfedern. (2023). *1.1248 steel properties.* From https://info.formfedern.com/en/properties-of-spring-steel-sheets/

[15] Virgamet. (2023). *1.1248 steel properties.* From https://virgamet.com/c75s-1-1248-ck75-c75-xc75-xc70-75cr1-aisi-1075-spring-steel

[16] Precitec Optronik GmbH. (2019, OCT). *CHRocodile Overview: Chromatic Confocal sensors and probes Datasheet.*